Coherent Control and Reconstruction of Free-Electron Quantum States in Ultrafast Electron Microscopy

DISSERTATION

zur Erlangung des mathematisch-naturwissenschaftlichen Doktorgrades

"Doctor rerum naturalium"

der Georg-August-Universität Göttingen

–

im Promotionsprogramm ProPhys

der Georg-August University School of Science (GAUSS)

von

Frau Katharina Elisabeth Priebe,
geb. Echternkamp

aus Köln

Göttingen, 2017

Betreuungsausschuss

Prof. Dr. Claus Ropers, IV. Physikalisches Institut

Prof. Dr. Dirk Schwarzer, Institut für Physikalische Chemie

Mitglieder der Prüfungskommission

Referent:	Prof. Dr. Claus Ropers, IV. Physikalisches Institut
Korreferent:	Prof. Dr. Stefan Mathias, I. Physikalisches Institut
2. Korreferent:	Prof. Dr. Thomas Baumert, Institut für Physik, Universität Kassel

Weitere Mitglieder der Prüfungskommission

Prof. Dr. Tim Salditt, Institut für Röntgenphysik

Prof. Dr. Steffen Schumann, II. Physikalisches Institut

Prof. Dr. Dirk Schwarzer, Institut für Physikalische Chemie

Prof. Dr. Annette Zippelius, Institut für Theoretische Physik

Tag der mündlichen Prüfung: 19. Dezember 2017

Come on Rory! It isn't rocket science, it's just quantum physics! - The Doctor

Steven Moffat

Abstract

The present (cumulative) thesis examines the quantum coherent interaction of ultrashort free-electron pulses with tailored optical near-fields. Multiple fields are utilised to prepare, coherently manipulate and characterise the longitudinal component of free-electron momentum superposition states.

After traversal of an intense optical near-field, the free-electron kinetic energy spectrum exhibits sidebands that are separated by the photon energy, which can be attributed to a phase modulation of the longitudinal electron wavefunction. To characterise these electron quantum states, an algorithm termed "SQUIRRELS" (Spectral QUantum Interference for the Regularised Reconstruction of free-ELectron States) is developed that is capable of reconstructing free-electron density matrices from experimental spectrograms.

As a first application, quantum state reconstruction by SQUIRRELS is used to experimentally demonstrate sub-cycle temporal structuring of the electron density. Free-space propagation of the phase-modulated electron wavefunction dispersively reshapes the electron density, leading to the formation of a train of attosecond electron density spikes at few-millimetre distance behind the interaction plane. Inelastic electron-light scattering may thus find application as a programmable, temporal phase plate for free electrons enabling time-resolved electron microscopy with attosecond precision.

Besides spatio-temporal shaping of electrons, phase-locked interactions with multiple near-fields constitute an essential building block for future quantum optics experiments with free electrons.

Zusammenfassung

Die vorliegenden (kumulative) Arbeit untersucht die quantenkohärente Wechselwirkung ultrakurzer Freie-Elektronenpulse mit maßgeschneiderten optischen Nahfeldern. Mehrere Felder werden zur Erzeugung, kohärenten Manipulation und Charakterisierung der longitudinalen Komponente der Superposition von Impulszuständen freier Elektronen genutzt.

Die Energieverteilung freier Elektronen weist nach dem Durchqueren eines intensiven optischen Nahfeldes Seitenbänder im Abstand der Photonenenergie zueinander auf. Dies kann auf eine Phasenmodulation der longitudinalen Elektronenwellenfunktion zurückgeführt werden. Um diese Elektronenquantenzustände zu charakterisieren, wird ein Algorithmus namens "SQUIRRELS" (Englisch für "Spektrale Quanteninterferenz für die

regularisierte Rekonstruktion freier Elektronenzustände") entwickelt, der es erlaubt, die Dichtematrix freier Elektronen aus experimentellen Spektrogrammen zu rekonstruieren.

Eine erste Anwendung der Quantenzustandsrekontruktion mittels SQUIRRELS zeigt experimentell die zeitliche Strukturierung der Elektronendichte innerhalb eines Lichtzyklus. Propagation im freien Raum führt zu einer zeitlichen Umverteilung der Elektronendichte, sodass einige Millimeter hinter der Wechselwirkungsebene ein Zug von Attosekunden-Elektronenpulsen entsteht. Inelastische Streuung von Elektronen an Licht könnte somit Anwendung als programmierbare zeitliche Phasenplatte für freie Elektronen finden, die zeitaufgelöste Elektronenmikroskopie mit Attosekunden-Präzision ermöglicht.

Neben der räumlichen und zeitlichen Formung von Elektronen stellen phasengekoppelte Wechselwirkungen mit mehreren Nahfeldern einen wichtigen Baustein für zukünftige quantenoptische Experimente mit freien Elektronen dar.

Contents

List of Figures

Symbols and Abbreviations

Symbol	Meaning	Unit
a, $a^\dagger$	lowering and raising operators	
$\vec{a}$	Bloch vector	1
$\vec{A}$	vector potential	$\mathrm{V\,s\,m^{-1}}$
c	vacuum speed of light	$\mathrm{m\,s^{-1}}$
C_c	chromatic aberration coefficient	m
d	dimension of Hilbert space	1
d	propagation distance	m
e	elementary charge	C
E	energy	eV
E_0	initial energy	eV
ΔE	energy bandwidth (FWHM)	eV
F	electric field	$\mathrm{V\,nm^{-1}}$
g	coupling constant	1
$\hbar$	reduced Planck constant	J s
I	intensity	$\mathrm{TW\,cm^{-2}}$
k	angular wavenumber	$\mathrm{m^{-1}}$
m	electron mass	kg
N	sideband number	1
p, $\vec{p}$	momentum	$\mathrm{kg\,m\,s^{-1}}$
p_0	initial momentum	$\mathrm{kg\,m\,s^{-1}}$
P	purity	1
Δt	time delay	s
T	optical period	fs
U	acceleration voltage	V
U_P	ponderomotive potential	eV
v	relativistic electron velocity	$\mathrm{m\,s^{-1}}$

x, z	spatial coordinates	nm
β	collection angle	mrad
ε	reconstruction error	1
γ	Lorentz factor	1
λ	wavelength	nm
φ	relative phase	rad
ρ	density operator	1
$\sigma_{x,y,z}$	Pauli matrices	1
σ_ϕ	phase jitter (standard deviation)	rad
τ	pulse duration	fs
ω	optical (angular) frequency	Hz
Ω	detuning of optical (angular) frequency	Hz

Abbreviation	**Meaning**
CDI	coherent diffractive imaging
cw	continuous wave
DTEM	dynamic transmission electron microscope
EEHG	echo-enabled harmonic generation (FEL)
EELS	electron energy loss spectroscopy
FEL	free-electron laser
FROG	frequency-resolved optical gating
FWHM	full-width at half-maximum
HGHG	high-gain harmonic generation (FEL)
HHG	high harmonic generation
IELS	inelastic electron-light scattering
LIED	laser-induced electron diffraction
PCGPA	principal component generalised projections algorithm
PINEM	photon-induced near-field electron microscopy
RABBITT	reconstruction of attosecond beating by interference of two-photon transitions
RF	radiofrequency
SASE	self-amplified spontaneous emission
SHG	second harmonic generation

SPIDER	spectral phase interferometry for direct electric-field reconstruction
STED	stimulated emission depletion
SQUIRRELS	spectral quantum interference for the regularised reconstruction of free-electron states
THz	terahertz
UEM	ultrafast electron microscopy
UTEM	ultrafast transmission electron microscopy
XUV	extreme ultraviolet

Chapter 1

Introduction

Light-matter interaction is governed by the microscopic motion of electrons in atoms, molecules and solids exposed to electromagnetic radiation. A wealth of phenomena, including light emission, plasmons and nonlinear optical effects, and optical properties like the refractive index, is fundamentally caused by electron displacements in matter. The ability to control these electronic motions with light plays a central role in attosecond science [1], with high-harmonic generation [2, 3] as a prominent example. A profound understanding of charge dynamics in atoms, molecules and solids is a prerequisite for the engineering of complex materials that promise technological leaps, for instance, in future information and energy storage, signal transmission and light harvesting. Such understanding calls for techniques that are able to investigate nanoscopic charge dynamics on their natural time and length scales.

Pump-probe techniques [4] achieve very high temporal resolution, provided that ultrashort pulses are available. In photon optics, the quest for ever shorter pulse durations resulted not only in the ability to generate attosecond pulses, but also in advanced pulse shaping techniques that are capable of producing virtually any desired optical waveform. Programmable temporal pulse shaping promoted coherent control, multidimensional spectroscopy and optical communication to name just a few of the many applications [5]. The versatility of optical methods is complemented by spatial beam shaping, for example, the generation of orbital angular momentum beams [6] and structured illumination microscopy [7]. Despite the fact that super-resolution techniques such as stimulated emission depletion (STED) [8] and scanning near-field optical microscopy (SNOM) [9] are able to break the diffraction limit, atomically resolved images still necessitates the use of probe beams with sub-nanometer wavelengths. Electrons are perfectly suited for

high-resolution imaging due to their small de-Broglie wavelength, besides offering much larger scattering cross-sections compared to x-rays. Spatio-temporal shaping techniques in electron optics, however, are significantly less advanced, and considerable effort is still required to reach similar levels as for their optical counterparts.

Temporal shaping of electrons is at the heart of ultrafast electron microscopy [10], as pulse compression capabilities dictate the ultimately achievable temporal resolution. Time-dependent electric fields in the radiofrequency [11–14] and THz range [15] have successfully been applied to compress electron pulses, and sub-100 fs pulse durations have been demonstrated. Atomic motion occurs on the femtosecond scale and can be resolved with state-of-the-art ultrafast electron microscopy. Electron movements are yet much faster, since atomic energy level separations are on the order of electronvolts, which translates to attosecond time scales. With the capability to generate attosecond XUV pulses, optical methods offer the necessary time resolution, though at a spatial resolution that is diffraction-limited to few tens of nanometres. Electron imaging and diffraction, in contrast, allow for atomic spatial resolution, and the generation of attosecond electron pulses is highly desirable to also push down the temporal resolution. Currently, simultaneous attosecond temporal and sub-Ångström spatial resolution is only achieved by laser-induced electron diffraction (LIED) [16, 17]. The versatility of LIED yet suffers from the large intertwining of the probing electron and the process under study, given that the sample is imaged by a re-colliding electron that was previously emitted from it. Attosecond electron pulses should preferably be prepared independently from the sample.

In this thesis, the inelastic scattering of swift free-electron beams with optical near-fields is studied in a coherent manner. Multiple tailored fields are used to phase-modulate the longitudinal component of the free-electron wavefunction. The motivation for this work is twofold: Firstly, this interaction offers huge potential for temporal shaping of electron beams with sub-cycle precision, and is therefore a promising candidate for realising the afore-mentioned imaging of electronic motion; secondly, the quantum coherent nature of this interaction suggests a transfer of quantum-optical concepts from photons to electrons. Quantum optics is an important research field with significant impact on many areas of physics. Besides fundamental tests of quantum theory that demonstrated counter-intuitive quantum mechanical effects like entanglement, teleportation [18] and the violation of Bell's inequality [19, 20], quantum optics fostered a large number of practical applications in optical communication and quantum information [21]. Originally focused on quantum states of light, quantum optics now more generally refers to quantum prop-

erties of light-matter interactions and has been successfully transferred to other physical systems, giving rise to new research fields such as neutron [22] and electron quantum optics [23].

In the present work, we achieve coherent control of *free electrons in vacuum*, which features a quasi decoherence-free evolution of the electron quantum state and therefore allows to study quantum coherent phenomena in a very clean form. We contribute to the toolbox of free-electron quantum optics [24] methods to prepare, coherently manipulate and characterise free-electron momentum superposition states. Such methods constitute essential building blocks for any quantum technology. Quantum state characterisation is applied to experimentally verify the achievement of sub-cycle temporal shaping of pulsed free-electron beams. These advanced temporal shaping capabilities and the ability to manipulate and characterise free-electron quantum states will enable novel, unimagined types of electron microscopy and may prove beneficial for quantum information science.

Outline

This thesis is organised as follows. The remainder of Chap. 1 draws a link to previous work and gives the theoretical background required for further discussion. In particular, inelastic electron-light scattering is introduced in Sec. 1.1, followed by a brief explanation of quantum state tomography in Sec. 1.2. The experimental setup, i.e., the Göttingen ultrafast transmission electron microscope, is described in Sec. 1.3, and the basics of electron pulse compression are presented in Sec. 1.4.

Chapter 2 presents the experimental realisation of *multi-field* interactions to coherently manipulate free-electron beams. A polarisation-sensitive nanostructure allows for individual control of the amplitude and phase of two spatially separated optical near-fields with which the electron beam sequentially interacts. In some analogy to the Ramsey method of oscillatory fields, the final electron state at the exit of this electron-light interferometer is governed by the relative phase between the two near-fields.

Chapter 3 comprises the results of two further multi-field experiments that employ (i) two-colour fields at frequencies ω and 2ω to coherently control the individual sideband populations and (ii) near-fields with millimetre scale spatial separation to study the influence of dispersion on the electron state. A method termed SQUIRRELS is developed to retrieve the free-electron quantum state from electron energy spectra, which are recorded for various relative phases between two optical near-fields that act upon the electrons.

Electron quantum state reconstruction by SQUIRRELS is applied to reveal the formation of an electron pulse train with sub-femtosecond pulse duration after few millimetres of free-space propagation.

Chapter 4 concludes the findings of Chapters 2 and 3 with a general discussion. SQUIRRELS will be compared to related techniques from ultrafast optics in Sec. 4.2, followed by an outlook on further investigations in Sec. 4.3. In particular, the feasibility of attosecond electron microscopy, potential advancements of the reconstruction method and imaginable future applications of inelastic electron-light scattering in quantum technologies and other research fields will be contemplated.

1.1 Coherent Electron-Light Scattering

Acceleration of bound electrons by time-dependent electric fields is ubiquitous in light-matter interaction. Facilitated by resonant excitations, the absorption of photons by atoms requires only weak intensities. In free space, no such resonances exist, and the strong electromagnetic fields required to observe free-electron light coupling were not yet available when Kapitza and Dirac proposed the diffraction of free electrons from a standing electromagnetic wave in 1933 [25]. Experimental demonstrations of free-electron motion control with electromagnetic radiation became possible with the invention of the laser. In the Kapitza-Dirac effect, observed for the first time in 2001 [26], the electrons simultaneously absorb and emit a photon, experiencing a net momentum change of $\Delta p = 2\hbar k$. While energy-momentum conservation is automatically fulfilled in this configuration, the emission or absorption of single photons by free electrons is prohibited in free space, as can be inferred from the mismatch in the free-electron and photon dispersion relations shown in Fig. 1.1**a**.

In other words, phase-matching is required for net energy exchange between a free-electron and an electromagnetic wave. This can be achieved in multiple ways: In 1975, for instance, Piestrup *et al.* employed the inverse Cerenkov effect [29] for the first experimental demonstration of momentum modulation of free electrons, where the phase velocity of light is retarded by a dielectric gas. In the inverse Smith-Purcell effect, phase-matching occurs due to the periodicity of the near-field at a grating [30]. In this thesis, free-electron light coupling is mediated in yet another way, making use of the momentum spread associated with field localisation at nanostructures.

Figure 1.1**b** illustrates the experimental scenario: A short electron pulse traverses the optical near-field of a nanostructure excited by a picosecond light pulse. The initially narrow electron energy distribution evolves into a spectrum consisting of a number of symmetrically populated sidebands that are separated by the photon energy. The observed free-electron light coupling can be regarded as a stimulated variant of the spontaneous electron-energy loss that electrons transmitted through matter experience due to collective excitations of charges. In contrast to common electron energy loss spectroscopy (EELS), the electrons both lose *and* gain energy in presence of a light field and a large fraction is scattered (up to 100 %), such that the zero-loss peak is strongly depleted. In 2009, inelastic electron-light scattering (IELS) based on field localisation was demonstrated for the first time by Barwick *et al.* [27] by observing the energy spectrum shown in Fig. 1.1**c**.

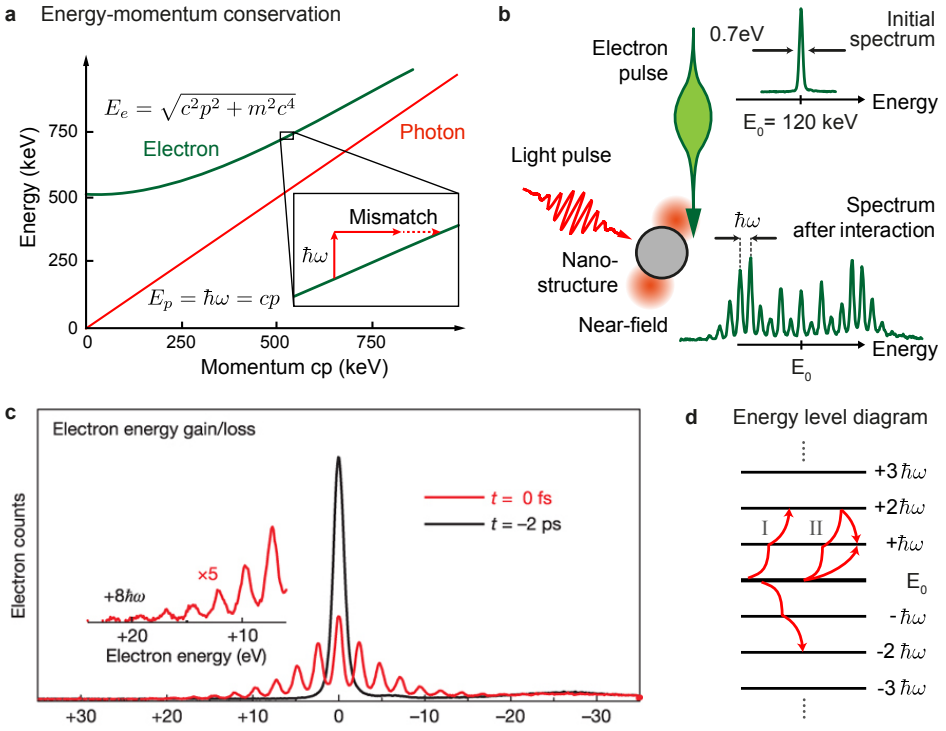

Figure 1.1: a Dispersion relations of free electrons and photons. In vacuum, absorption of photons by electrons is prohibited due to energy-momentum conservation. **b** After interaction with the near-field, the initially narrow electron energy spectrum exhibits several peaks separated by the photon energy. **c** First experimental demonstration of photon-induced electron energy gain ($E_0 = 200\,\mathrm{keV}$, reprinted with permission from Ref. [27]). **d** Energy ladder illustrating sequential single-photon transitions (I) and multipath interferences (II), reprinted with permission from Ref. [28].

The symmetric energy spectra result from absorption and emission of multiple photons with equal probabilities. In previous studies [27, 31, 32], incoherent spatial and temporal averages over near-field amplitudes due to laser pulse durations shorter than the electron pulse and electron focal spot sizes larger than the transverse near-field decay length gave rise to spectra with sideband amplitudes decaying towards larger orders, such as the one observed by Barwick *et al.*. The underlying process is however coherent in nature, such that multiple quantum paths on an infinite energy ladder leading to the same final energy interfere (type II interaction in Fig. 1.1**d**) and produce spectra with strongly modulated sideband amplitudes as in Fig. 1.1**b**. To reveal and, most importantly, to harness the coherence of this electron-light interaction, spatially and temporally homogeneous near-field amplitudes are required.

1.1.1 Theoretical description

A comprehensive derivation of the electron wavefunction after interaction for the general case of pulsed optical excitation can be found in Ref. [31], and a succinct description using ladder operators for the limiting case of continuous-wave excitation was derived in our group [28]. Here, the main findings will be briefly summarised.

Theoretically, the interaction can be described by solving the Schrödinger equation for the Hamiltonian $H = \frac{1}{2m}(\vec{p} + e\vec{A})^2$ of an electron with charge $-e$, mass m and momentum p in an electromagnetic field F, where the vector potential $\vec{A}$ is defined by $\vec{F} = -\partial\vec{A}/\partial t$. It was shown in Ref. [33] that this non-relativistic treatment is exactly equivalent to a relativistic description, when the relativistically correct value for the electron velocity and the corresponding non-relativistic values for momentum and kinetic energy are used, since the dispersion relation $\partial E/\partial p = v$ is identical in both cases, and equal momentum changes lead to the same energy change. Assuming a Gaussian light pulse with duration τ (intensity standard deviation) and a relative time delay δt between electron and light pulse, the final electron wavefunction in the co-moving frame is given by [31]

$$\psi_{\text{out}}(z) = \exp\left(-i\exp\left(-\frac{(z+v\delta t)^2}{4v^2\tau^2}\right)\operatorname{Im}\left[\exp\left(i\frac{\omega}{v}z\right)2g\right]\right)\psi_{\text{in}}(z). \tag{1.1}$$

Here, z is the spatial coordinate along the electron trajectory, v the relativistic electron velocity, ω the optical frequency and $\psi_{\text{in}}(z)$ the incident electron wavefunction. $g \in \mathbb{C}$ is a dimensionless coupling constant that is proportional to the spatial Fourier transform of the electric field along the electron trajectory $\tilde{F}_z$, evaluated at the spatial frequency component $\Delta k = \omega/v$ that corresponds to the momentum change of an electron gaining or losing an energy quantum $\hbar\omega$, so that energy-momentum conservation is fulfilled [28, 31]:

$$g = \frac{e}{2\hbar\omega}\tilde{F}_z\left(\frac{\omega}{v}\right) = \frac{e}{2\hbar\omega}\int_{-\infty}^{\infty}\mathrm{d}z\, F_z(z,0)\exp\left(-i\left(\frac{\omega}{v}z\right)\right). \tag{1.2}$$

In the derivation, the ponderomotive term $\vec{A}^2$ in the Hamiltonian was neglected due to the large electron momentum $\vec{p} \gg \vec{A}$, as well as the wavefunction dispersion during the interaction time. In the limit of continuous-wave excitation, i.e. $\tau \to \infty$, Eq. 1.1 reduces to [28]

$$\psi_{\text{out}}(z) = \exp\left(-2i|g|\sin\left(\frac{\omega}{v}z + \arg(g)\right)\right)\psi_{\text{in}}(z). \tag{1.3}$$

According to Eq. 1.3, IELS imprints a sinusoidal phase modulation onto the electron wavefunction, which gives rise to the observed symmetric sidebands in the energy spectrum. Equivalently, Eq. 1.3 can be written as a coherent superposition of momentum states $|N\rangle$, where $|N\rangle$ denotes a plane wave with shifted momentum $p = p_0 + N\frac{\hbar\omega}{v}$ with respect to the initial electron momentum p_0:

$$|\psi_{\text{out}}\rangle = \sum_N \left(\frac{g}{|g|}\right)^N J_N(2|g|)\,|N\rangle \quad \text{with} \quad \langle z|N\rangle = e^{i(p_0+N\frac{\hbar\omega}{v})z}. \tag{1.4}$$

Consequently, the N$^{\text{th}}$-order sideband population is given by the N$^{\text{th}}$-order Bessel function J_N and the spectral width is $\Delta E = 4|g|\hbar\omega$, such that the number of populated sidebands rises linearly with the optical field strength.

Simultaneous multi-field interactions can be described by multiplying Eq. 1.3 with further phase functions. For phase-locked two-colour interactions at frequencies ω and 2ω and a relative phase φ, the wavefunction is, for example, given by

$$\psi_{\text{out}}(z) = \exp\left(2i|g_\omega|\sin\left(\frac{\omega}{v}z\right)\right)\cdot\exp\left(2i|g_{2\omega}|\sin\left(\frac{2\omega}{v}z+\varphi\right)\right)\cdot\psi_{\text{in}}(z). \tag{1.5}$$

Using generalised Bessel functions $J_N(x,y;z)$ [34], we obtain for the momentum state

$$|\psi_{\text{out}}\rangle = \sum_N J_N(2|g_\omega|,2|g_{2\omega}|;e^{i\varphi})\,|N\rangle = \sum_N |N\rangle \sum_{l=-\infty}^{\infty} e^{il\varphi}J_{n-2l}(2|g_\omega|)J_l(2|g_{2\omega}|). \tag{1.6}$$

Experimentally, the magnitude of the coupling constants $|g|$ can be controlled via the optical field strength or by tailored nanostructures with optimised spatial Fourier components $\tilde{F}_z(\omega/v)$ (see also Appendix 5.2), e.g., by using resonant gratings [35]. Fluence-dependent measurements of electron energy spectra confirmed the theoretically predicted coherent nature of the inelastic electron scattering with remarkable agreement between experiment and calculation [28]. Figure 1.2 displays Rabi-oscillations [36], a hallmark of quantum coherence, in the population of the different photon sidebands due to multi-level interferences. Rabi-oscillations are typically discussed in the context of two-level systems, in which the population of the ground and excited level are found to sinusoidally oscillate with time or field strength if an oscillatory driving field is applied. Here, an infinite number of sidebands is coherently coupled, giving rise to multi-level Rabi-oscillations in the fluence-dependent sideband populations. Since the Rabi frequencies of each tran-

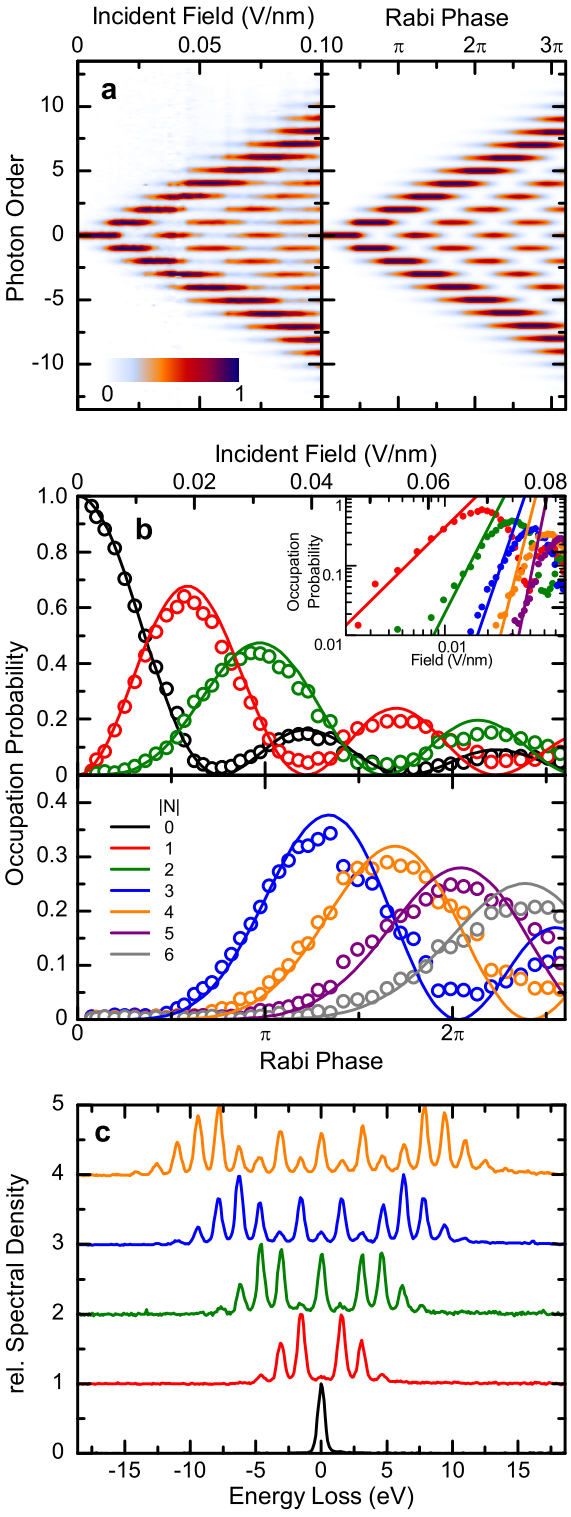

Figure 1.2: Experimental demonstration of multilevel Rabi-oscillations in the population of free-electron momentum states. **a** Measured fluence-dependent electron energy spectra (left) in near-perfect agreement with model calculations using N^{th}-order Bessel functions. The number of populated sidebands rises linearly with the optical field strength. Notably, the field-strength dependent sideband populations are strongly modulated: The initial energy level is, for instance, depleted around $F = 0.023\,\mathrm{V\,nm^{-1}}$ and repopulated at $F = 0.04\,\mathrm{V\,nm^{-1}}$. **b** The observed occupation probabilities of the N^{th}-order spectral sidebands extracted from **a** (open circles) are well described by the theoretically expected N^{th}-order Bessel functions (solid lines). Inset: A double-logarithmic plot of the sideband populations confirms the expected slope of $2N$ (solid lines) near the onset. **c** Measured electron energy spectra for optical field strengths $F = 0, 0.023, 0.040, 0.053$ and $0.068\,\mathrm{V\,nm^{-1}}$ (bottom to top). Spectra in **a** and **c** are normalised to their maxima for clarity. Reprinted with permission from Ref. [28].

sition are all equal in this case, free electrons in optical near-fields are ideally suited to experimentally investigate the so-called "equal-Rabi case" of multi-level quantum systems, which was studied theoretically by Eberly and co-workers in the seventies [37–39]. Analytically, the oscillations of the sideband populations are described by Bessel functions (cf. Eq. 1.4), which nicely follow the experimental data (solid lines in Fig. 1.2**b**).

1.1.2 Applications

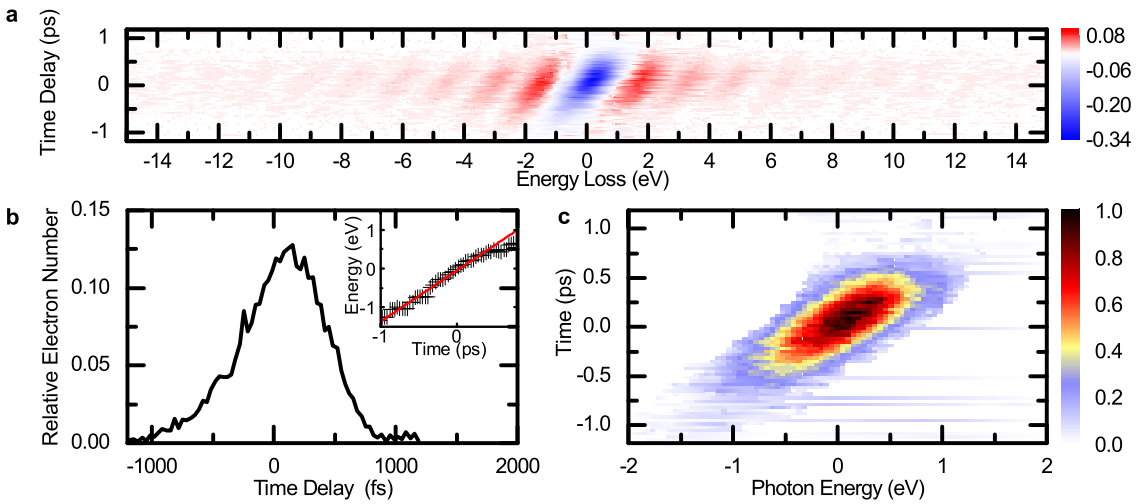

Figure 1.3: Application of IELS for electron pulse characterisation. **a** Electron energy spectra for varying time delay between electron and laser pulse (50 fs FWHM pulse duration, $\lambda = 800\,\text{nm}$). The initial energy distribution without laser excitation was subtracted from all spectra. **b** The fraction of electrons scattered to higher and lower energies indicates the temporal structure of the electron pulse (convoluted with the much shorter laser pulse). Inset: Photon sideband shift relative to the zero-loss peak. **c** The normalised electron density in time-energy-space reveals the electron chirp. Reprinted with permission from Ref. [28].

Inelastic scattering of electrons found applications as a contrast mechanism in transmission electron microscopy, termed photon-induced near-field electron microscopy (PINEM), to image optical near-fields [40]. Here, by using energy-gain scattered electrons for image formation, one obtains a map of the near-field Fourier component $\tilde{F}_z(\omega/v)$ with high spatial resolution. In other EELS-based methods such as STEM SI (scanning transmission electron microscopy spectrum imaging) [41] or EFTEM SI (energy filtered transmission electron microscopy) of plasmons [42, 43], multiple electro-magnetic modes of a nanostructure are excited by the electron beam itself. In PINEM, in contrast, only

specific modes are excited optically, and can be detected background-free in the energy-gain region of the spectrum.

Moreover, PINEM has been used to characterise ultrashort electron pulses by scanning the relative delay between the near-field excitation and the electron arrival time and recording the resulting energy spectrum [44–46]. Figure 1.3**a** shows an exemplary electron-photon cross-correlation. Because the interaction only takes place when both electron and light pulse are present, the time dependent number of scattered electrons shown in Fig. 1.3**b** traces the convolution of the electron and light pulse envelopes. In this case, 50 fs laser pulses much shorter than the electron pulse were used, so that the temporal width of the cross-correlation very closely corresponds to the electron pulse duration.

In this thesis, the quantum coherent nature of IELS will be harnessed for free-electron quantum state preparation, coherent control, interferometry and state characterisation.

1.2 Quantum State Tomography

Knowing the quantum state of a physical system is equivalent to having complete information about the system, such that one knows the probability distribution for the outcome of any possible measurement on the system [47]. Complete quantum state characterisation is crucial for practically all quantum optics applications such as quantum computation, communication and cryptography, e.g., to verify the correct functioning of sources, transmission lines and gates.

In classical mechanics, the state of a particle is completely described by its position and momentum, which can be measured, in principle, simultaneously with arbitrary precision. In quantum mechanics, however, Heisenberg's uncertainty principle [48] and the no-cloning theorem [49] fundamentally prohibit a complete state characterisation of a single particle, that would require multiple measurements on the same object. Each individual measurement modifies the particle's state, which can be nicely illustrated by considering the state of a free electron after interaction with an optical near-field as discussed in Section 1.1. Initially, the electron is in a superposition state of plane waves with energies $E_0 \pm N\hbar\omega, N \in \mathbb{N}_0,\ N \leq 2|g|$. After the energy measurement, the state "collapses" to an eigenstate of the measurement operator according to von Neumann's definition of projective measurements [50], e.g., to the state with energy $E_0 + 3\hbar\omega$, which is clearly different from the initial state. Measurements on many identically prepared electrons will

generally yield different measurement results due to the probabilistic nature of quantum mechanics, and one obtains the energy probability distribution or spectrum.

The spectrum only contains the magnitude or population of the individual momentum sidebands, while any phase information is lost in the measurement process. Furthermore, it is impossible to distinguish between a coherent superposition of momentum states and a statistical ensemble of electrons with different classical energies on the basis of an energy spectrum alone.

This Section briefly introduces the concept of *quantum state tomography*, which aims at obtaining the maximum information possible about an ensemble of quantum states. A comprehensive collection of theoretical and experimental developments in this field can be found in Ref. [47]. To begin with, the density operator, a mathematical object describing a quantum state, will be introduced.

1.2.1 Pure and Mixed Quantum States: The Density Operator

Quantum states which can be written as a vector $|\psi\rangle$ in a Hilbert space are called *pure states*. This is, however, not the most general description of a quantum state: An ensemble of quantum systems might be in a statistical mixture of multiple pure states, a so-called *mixed state*, and requires a different mathematical description. Mixed states arise, for example, from experimental uncertainties in the state preparation, but also if only a subsystem of a larger system in a pure, entangled state is observable. Mathematically, mixed states are described by a density operator

$$\rho = \sum_k p_k \left|\psi_k\right\rangle \left\langle\psi_k\right|, \quad \sum_k p_k = 1, \tag{1.7}$$

where p_k denotes the probability to find the system in the pure state $|\psi_k\rangle$. Note that the $|\psi_k\rangle$ do not necessarily form a basis of the Hilbert space, and the same density operator may describe several different ensembles of mixtures. Density operators have the following general properties [51]:

- they are hermitean $\rho = \rho^\dagger$,
- positive semidefinite, i.e. all eigenvalues $\lambda \geq 0$
- and have trace one: $\mathrm{tr}(\rho) = 1$.

In the density operator formalism, pure states are simply described by $\rho = |\psi\rangle\langle\psi|$. Obviously, pure states are idempotent, i.e. $\rho^2 = \rho$. Therefore, it is convenient to define the purity of a state as $P = \mathrm{tr}(\rho^2)$, which is $P = \mathrm{tr}(\rho^2) = \mathrm{tr}(\rho) = 1$ for pure states and ≤ 1 otherwise. The purity is bounded by $\frac{1}{d} \leq P \leq 1$, where d is the dimension of the Hilbert space. Maximally mixed states, described by the scaled identity matrix $\frac{1}{d} I_d$, have the lowest purity $P = \frac{1}{d}$.

Density operators are represented by square matrices in a basis $\{|i\rangle\}$ of the Hilbert space. With $|\psi_k\rangle = \sum_i c_i^k |i\rangle$, the diagonal matrix elements are given by $\rho_{ii} = \langle i|\rho|i\rangle = \sum_k p_k |c_i^k|^2$. They correspond to the probability distribution or *populations* of the basis states $|i\rangle$ and can readily be quantified by projective measurements on the basis states. The off-diagonal elements ρ_{ij} or *coherences* contain information about the interference between the amplitudes of states $|i\rangle$ and $|j\rangle$ and are not directly accessible. Therefore, quantum state tomography techniques to recover the missing information from suitable measurements have been developed. The following Section illustrates the principle of quantum state estimation for the rather trivial, but particularly demonstrative case of two-level systems, also known as qubits.

1.2.2 Qubits and Bloch Sphere Representation

A qubit is a quantum system that has only two possible measurement outcomes, usually denoted as 0 or 1, such as spin for electrons or polarisation for photons. In contrast to classical bits, the system can be in a superposition state $|\psi\rangle = \alpha|0\rangle + \beta|1\rangle, \alpha, \beta \in \mathbb{C}$, where the probability to measure 0 or 1 is given by $|\alpha|^2$ or $|\beta|^2$, respectively, such that $|\alpha|^2 + |\beta|^2 = 1$. Using the parametrisation $\alpha = \cos(\theta/2)$ and $\beta = e^{i\varphi}\sin(\theta/2)$ with $0 \leq \theta \leq \pi$ and $0 \leq \varphi \leq 2\pi$, the state can be visualised as a point on the Bloch sphere (cf. Fig. 1.4). Note that since global phase factors do not play a physical role, α can be chosen as a real value. The state $|0\rangle$ corresponds to the north pole and $|1\rangle$ to the south pole of the sphere, and all other points on the surface are coherent superpositions of these two basis states.

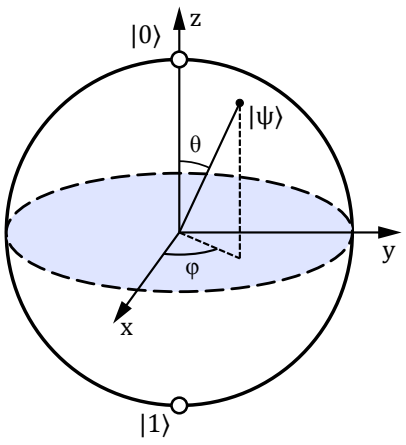

Figure 1.4: Visualization of the pure qubit state $|\psi\rangle = \cos\left(\frac{\theta}{2}\right)|0\rangle + e^{i\varphi}\sin\left(\frac{\theta}{2}\right)|1\rangle$ on the Bloch sphere. Pure states are represented by points on the surface and mixed states by points within the unit sphere.

For qubits, the density operator is represented by a 2x2 matrix, which can be expanded in the basis $\{I_2, \sigma_x, \sigma_y, \sigma_z\}$, where $\sigma_{x,y,z}$ denote the traceless Pauli matrices [52]:

$$\rho = \frac{1}{2}\left(I_2 + \vec{a}\cdot\vec{\sigma}\right), \quad \vec{a} \in \mathbb{R}^3. \tag{1.8}$$

$\vec{a}$ is called the Bloch vector. It follows from the positive-semidefiniteness of ρ that $|\vec{a}|^2 \leq 1$, meaning that there is a one-to-one correspondence between the single-qubit density matrix and points in the Bloch sphere, as mentioned above. For pure states, the eigenvalues $\lambda_{1,2}$ must be 0 and 1, such that the determinant $\det\rho = \lambda_1 \cdot \lambda_2 = (1 - |\vec{a}|^2)/4 = 0$ vanishes and $|\vec{a}|^2 = 1$. Thus, pure states are points on the surface of the Bloch sphere, whereas mixed states ($|\vec{a}| \leq 1$) are located within the sphere. The maximally mixed state with $\vec{a} = \vec{0}$ corresponds to the sphere's origin.

The goal of quantum state tomography is to determine all elements of the density matrix ρ. For a qubit, this corresponds to quantifying four values, of which only three are independent (due to the trace constraint), namely the three components of the Bloch vector $\vec{a}$. These can be obtained by three measurements in different directions $\hat{n}$ on many identically prepared copies of the quantum system that will yield the expectation values $\langle\hat{n}\cdot\vec{\sigma}\rangle_\rho = \mathrm{tr}\left(\rho\hat{n}\cdot\vec{\sigma}\right) = \hat{n}\cdot\vec{a}$. Such measurements can be performed either by rotating the detector or by keeping the detector fixed and rotating the state, for example by waveplates when looking at the polarisation state of a photon.

It is possible to generalise the Bloch vector description to higher-dimensional Hilbert spaces. In particular, the density matrix can be expanded analogously to Eq. 1.8 using the generators σ_j of the special unitary group $SU(d)$ [52] (which are the Pauli matrices for $d = 2$):

$$\rho = \frac{I_d}{d} + \frac{1}{2}\sum_{j=1}^{d^2-1} a_j \sigma_j. \tag{1.9}$$

Consequently, for a d-dimensional Hilbert space, $d^2 - 1$ measurements (assuming perfect detection) are required to completely reconstruct the state. In this context, it should be pointed out that the free-electron quantum state given by Eq. 1.4 is strictly speaking infinite-dimensional. In practice, however, the density matrix can be truncated after $N \gtrapprox 2|g|$ sidebands given that only a finite number of energy levels is significantly populated.

1.2.3 Wigner Function

In Section 1.2.1, the density operator was introduced as the most general, but rather abstract quantum state description. An equivalent, in the context of phase-modulated electrons perhaps more intuitive description is given by a phase-space representation based on the *Wigner function* $W(x,p)$, which was introduced by Eugene P. Wigner in 1932 [53]:

$$W(x,p) = \frac{1}{\pi\hbar}\int_{-\infty}^{\infty} \mathrm{d}y\, \langle x+y|\rho|x-y\rangle\, e^{-2ipy/\hbar} \tag{1.10}$$

Here, x and p denote position and momentum, respectively. The Wigner function can analogously be defined in time-frequency space. In contrast to classical phase space distributions, the Wigner function can assume negative values for quantum states without a classical correspondence [54], such that it cannot be interpreted as a true probability distribution. Integration of $W(x,p)$ over position x or momentum p, however, yields the corresponding marginal or probability distributions, that are strictly positive:

$$P(x) = \int_{-\infty}^{\infty} W(x,p)\,\mathrm{d}p, \tag{1.11}$$

$$P(p) = \int_{-\infty}^{\infty} W(x,p)\,\mathrm{d}x. \tag{1.12}$$

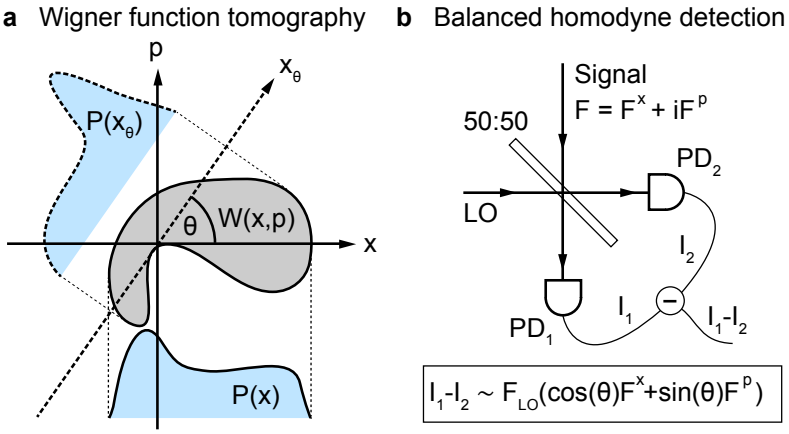

Figure 1.5: Optical homodyne tomography. **a** Schematic marginal distributions $P(x_\theta)$ of a Wigner function $W(x,p)$ at angles 0 and θ. **b** In balanced homodyne detection, the signal field F is superposed with a strong local oscillator (LO) using a 50:50 beam splitter. Depending on the relative phase θ between signal and LO, the photocurrent difference $I_1 - I_2$ measured by photodiodes (PD) is proportional to different field quadratures $F^\theta = \cos(\theta)F^x + \sin(\theta)F^p$.

Knowledge of the two marginal distributions $P(x)$ and $P(p)$ is insufficient to retrieve the Wigner function. Figure 1.5**a** illustrates marginal distributions that correspond to tomographic cuts through the Wigner function taken at arbitrary angles θ. Similar to tomography techniques used in medicine, it is possible to retrieve the Wigner function by recording such cuts at all angles [55] and applying an inverse Radon transformation on the dataset. In practice, the continuous ensemble of angles is well approximated by measuring a finite number.

Figure 1.5**b** illustrates the first experimental realisation of this principle, which was succesfully implemented by the Raymer group in 1993 [56, 57] to reconstruct the Wigner function and density matrix of an electric-field mode by optical homodyne tomography (OHT). In OHT, the signal field is superposed at a beam splitter with a *local oscillator*, a strong coherent-state field with the same frequency as the signal, and the photocurrent at the two output ports of the beam splitter is detected by two balanced photodiodes, as illustrated in Fig. 1.5**b**. The difference signal is proportional to the signal quadrature that is in phase with the local oscillator. By varying the relative phase, tomographic cuts through the Wigner function can be measured at all angles.

1.2.4 State Tomography for Other Physical Systems

Since the pioneering work by the Raymer group, quantum state tomography was successfully extended to other physical systems and improved or novel reconstruction algorithms were developed. Some methods retrieve the density matrix ρ, others the Wigner function $W(x,p)$. Due to the one-to-one correspondence between $W(x,p)$ and ρ given by Eq. 1.10, the respective quantity can be obtained by a Weyl transform [58, 59]. Apart from photons, the quantum states of atomic beams [60, 61], vibrations of molecules [62], ions in a Paul trap [63] and, more recently, single electron excitations in quantum Hall edge channels [64, 65] have successfully been reconstructed. Maximum likelihood algorithms significantly reduce statistical errors compared to linear inversion methods (see Chap. 3 in Ref. [47]). Going beyond the estimation of a system's state, so-called *quantum-process tomography* techniques to characterise unknown quantum operations of a quantum device have been developed [66].

In Section 3 of this thesis, a novel variant of quantum state tomography for free-electrons, termed SQUIRRELS, will be introduced, which enables the characterisation of longitudinal electron momentum states prepared by coherent electron-light scattering.

The density matrix and Wigner function of such a phase-modulated free-electron state are exemplarily depicted in Figs. 1.6**d** and **e**. Notably, the temporal shape of the electron density is obtained as a marginal of the Wigner function (cf. Fig. 1.6**g**). SQUIRRELS will thus play an important role for the metrology of sub optical-cycle shaped electron pulses, which represent promising, tailored probes for advanced versions of time-resolved electron microscopy or diffraction.

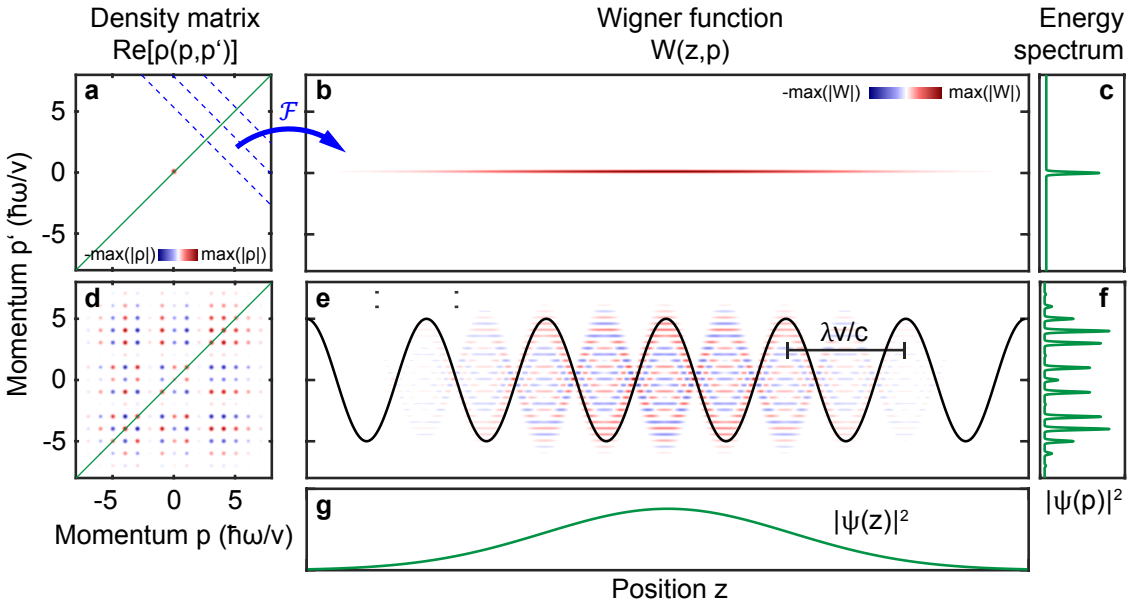

Figure 1.6: Density matrix $\rho(p,p')$ and Wigner function $W(z,p)$ of a free electron before (**a**,**b**) and after optical phase modulation (**d**,**e**). The density matrix is calculated with Eq. 5.8 and the Wigner function is obtained from the density matrix according to Eq. 1.10 by taking the Fourier transform along the anti-diagonals of ρ (exemplarily indicated by dashed blue lines in (**a**)). The solid black line in (**e**) emphasises the sinusoidal shape of the phase modulation with periodicity $\lambda v/c$. **c**,**f** The diagonal elements $\rho(p,p)$ of the density matrix (green lines in (**a**),(**d**)) or, equivalently, the momentum marginals of the Wigner functions yield the electron energy spectrum. **g** The position marginal of the Wigner function yields the temporal envelope, which, directly after the interaction, is identical for (**b**) and (**e**). Calculations for a pure quantum state (coherent electron energy bandwidth $\Delta E = 0.4\,\mathrm{eV}$), $\lambda = 800\,\mathrm{nm}$ and coupling constant $g = 2.5$.

1.3 Ultrafast Electron Microscopy

Electron microscopy is one of the most powerful and versatile techniques for the study of material properties on atomic length scales. Conventional electron microscopes, however, provide rather poor temporal resolution compared to ultrafast optical and x-ray techniques [67, 68] that use pump-probe methods to decouple the time resolution from the detector speed. Recent developments of time resolved electron microscopy, diffraction and spectroscopy techniques, such as ultrafast electron microscopy [10] and ultrafast electron diffraction [69, 70], have improved the temporal resolution by several orders of magnitude and enable the study of rapid atomic processes on ultrashort time scales.

Since the pioneering work by Bostanjoglo *et al.* in the 1980s [71] and major advancements by the Zewail group in 2005 [10, 72], time-resolved electron microscopy has significantly gained in interest, which is reflected in a growing number of research groups worldwide working on this topic [73–78]. Two complementary approaches, namely dynamic (DTEM) and ultrafast (UTEM) transmission electron microscopy, have emerged:

- In DTEM, each electron pulse contains enough electrons to record a wide-field image of the sample under study, typically many millions. While only one image is recorded in the original "single shot" approach [79], the advanced, "movie-mode" version of DTEM captures a small series of images (up to 16) within a short time span (up to 100 µs) [80]. DTEM is ideally suited to study irreversible processes, including irreversible phase transitions and melting.

- UTEM, in contrast, utilises electron pulses with typically one electron per pulse or less in order to prohibit beam quality degradation by space-charge effects. The image, diffraction pattern or electron energy spectrum is then integrated over thousands to millions of shots in a stroboscopic fashion. Consequently, UTEM is limited to the study of reversible processes, e.g. plasmonics [32, 81] and reversible phase transitions such as charge density waves [82]. At present, however, UTEM offers better temporal and spatial resolution than DTEM, owing to the superior coherence properties and lower energy spread of the single-electron pulses.

The Göttingen UTEM [83], used in this work, follows the stroboscopic approach, which will be briefly introduced in the following. Ultrafast transmission electron microscopy is based on pump-probe measurements, an established technique well-known from time-resolved optical spectroscopy. A laser pump beam excites the sample, which is probed

by a pulsed electron beam at varying time delays (cf. Fig. 1.7**a**). The temporal resolution is ultimately limited by the laser and electron pulse durations – currently in the range of 200 fs [83] – rather than by the detector speed. High-brightness, pulsed electron sources are thus a key ingredient for UTEM.

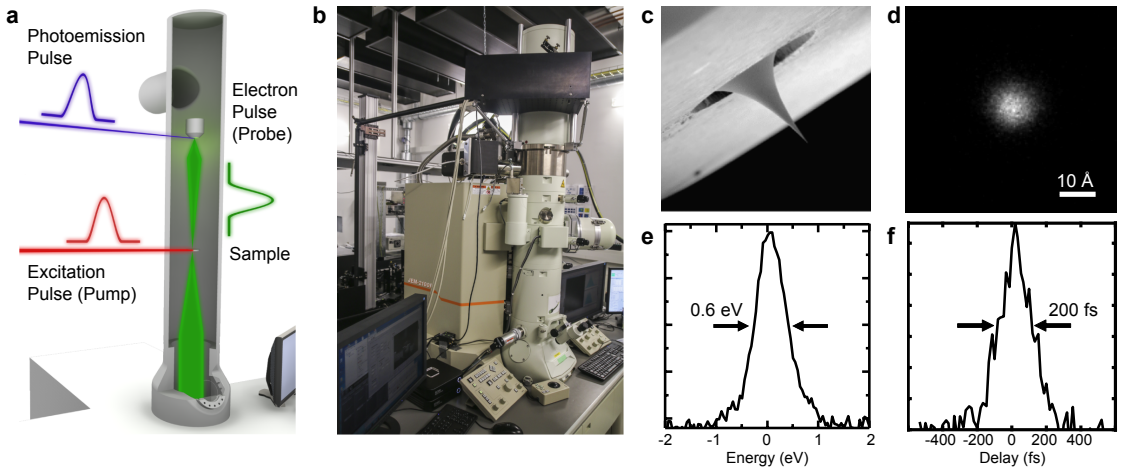

Figure 1.7: The Göttingen UTEM instrument and its electron pulse properties. **a** Schematic setup illustrating the laser-pump electron-probe principle. **b** Photograph of the modified JEOL JEM-2100F electron microscope. **c** Scanning electron micrograph of the nanoscopic ZrO/W(100) tip emitter. Illumination with ultrashort laser pulses (50 fs FWHM pulse duration, $\lambda = 400$ nm) yields electron bunches focusable down to 0.89 nm (**d**), at an energy width of 0.6 eV (**e**) and a pulse duration of 200 fs (**f**). Reprinted with permission from Ref. [83].

The Göttingen UTEM is special in this respect, in the sense that it is the first instrument featuring a nanoscopic tip emitter as an electron source instead of a flat photocathode. Specifically, the pulsed electron beam is generated by single-photon photoemission from a heated zirconium-oxide-covered tungsten tip using ultrashort laser pulses (400 nm wavelength, 50 fs pulse duration, 250 kHz repetition rate). The electrons are emitted from the front facet of the tip, i.e., an emission area that is much smaller than in the case of flat photocathodes, and thus exhibit a high spatial coherence, which is manifest in focus spot sizes as small as 0.89 nm. The advanced electron beam properties, which are summarised in Fig. 1.7**d**-**f**, render the Göttingen UTEM ideally suited for the study of quantum-coherent electron-light scattering. More details on the instrumentation can be found in Ref. [83].

1.4 Temporal Shaping of Electron Pulses

The ability to control the spatial propagation of light and electrons renders photonics and electron optics among the most advanced technologies. Super-resolution optical microscopy techniques such as STED (stimulated emission depletion) [8, 84] and structured illumination microscopy [7] make use of spatially shaped light beams. Frequency combs [85] and attosecond pulses [86] exemplify the excellent controllability of electromagnetic fields in the temporal domain. Analogous capabilities in electron optics, to date by far surpassed by light optics, are highly desirable, not only due to the short de Broglie wavelength of electrons which allows for sub-atomic spatial resolution. Motivated by a wealth of novel applications in electron imaging, diffraction and spectroscopy, shaping of free-electron beams in space and time has therefore recently attracted much attention. Electron vortex beams, for instance, promise atomic scale measurements of magnetic moments [87, 88]. Laser-driven electron accelerators [89] are expected to bring high-energy physics into the realm of table-top experiments in the long term. Ultrafast electron diffraction and imaging utilising high brightness, pulsed electron sources [10, 28, 70, 83, 90, 91] yield access to nanoscale dynamics in spatially inhomogeneous media. An ultimate goal would be the development of a programmable pulse shaper for the synthetisation of arbitrary electron pulses and beam profiles, similar to spatial light modulators for photons [5]. This Section will introduce means to temporally shape free electrons. Spatial degrees of freedom will not be considered.

In contrast to photons, electrons experience dispersion in vacuum due to their mass. Consequently, ultrashort electron pulses, having a finite energy bandwidth, will quickly spread in time during free-space propagation – even in the single-electron regime, where space-charge effects due to Coulomb repulsion are absent. In order to achieve the desired high temporal resolution in electron imaging, diffraction and spectroscopy, one can post-select a short temporal slice of a longer electron pulse by energetic or spatial filtering (at the cost of total electron current) [44, 92–95], minimise the dispersion by keeping the source-sample distance as short as possible [70, 96, 97] or actively compensate for the dispersion by re-compressing the electron pulses with time-dependent electric fields [11, 12, 15, 98, 99].

In ultrafast optics, light pulses can be compressed to pulse durations below their initial Fourier limit: First, nonlinear spectral broadening is employed, which induces a time-dependent instantaneous frequency or chirp. In the second step, the spectral phase is re-

flattened by a suitable, dispersive optical element, such as a prism, fiber or chirped mirror. By chirp overcompensation, the shortest laser pulse duration can be obtained at a distant position in the beam path, e.g. at the position of the sample under study. Analogously, radio frequency (RF) cavities are routinely used in accelerators and free-electron lasers (FEL) for electron pulse compression by *velocity bunching* [100]. To this end, a chirp is induced in the electron pulse, resulting in kinetic energies in the leading edge of the pulse smaller than in the trailing edge, so that the pulse will self-compress after a certain amount of free-space propagation. The achievable time resolution, however, crucially depends on the synchronisation of the microwave field and electron pulse arrival time [101], which becomes technologically increasingly difficult towards the sub-10 fs regime. Therefore, this concept has been transferred to the terahertz (THz) and optical domain [15] to enable all-optical electron pulse control, which suffers less from synchronicity issues. THz control of electron pulse propagation has been successfully demonstrated by Wimmer *et al.* [102]. Notably, when combining several compression stages at increasing driving frequency going from the microwave to the optical domain, the overall timing jitter would be exclusively limited by the last interaction [103], which can be easily stabilised with sub-fs precision based on optical interferences.

In the remainder of this Section, it will be shown that coherent electron-light scattering introduced in Sec. 1.1 can be harnessed to bring the temporal resolution of ultrafast transmission electron microscopy, currently in the range of few hundred fs [83], to the attosecond regime. This is achieved by shaping the ultrashort electron pulses with sculpted light fields on a sub-cycle time scale [28]. Figure 1.8**a** displays the evolution of the electron density during free-space propagation. With increasing propagation distance, the sinusoidal phase modulation imprinted onto the electron wavefunction transforms into a density modulation. This occurs due to the fact that the phase modulation corresponds to periodically alternating positive and negative chirp, such that the electron wavepacket compresses during free-space propagation, and a spike in the electron density of attosecond duration is produced once per optical period T. In the phase space picture shown in Fig. 1.8**b**, dispersion corresponds to a shearing of the electron's Wigner function along the time axis. For a certain amount of shearing, that is, at the temporal focus position, the projection of the Wigner function onto the time axis exhibits a sharp peak (Fig. 1.8**c**). Note that in contrast to electron microbunching in a free-electron laser (FEL), where a larger number of electrons is contained in each pulse, here, the bunching of the wavefunction of a single electron is discussed.

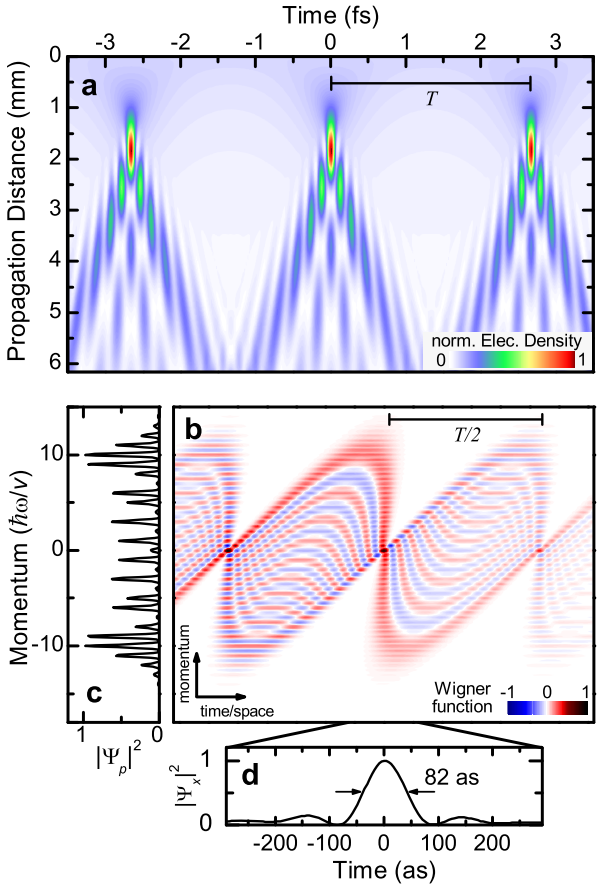

Figure 1.8: Prediction of attosecond electron pulse trains generated by sinusoidal phase modulation. **a** Evolution of electron density for free-space propagation (numerical simulation for $g = 5.7$). At a certain distance downstream the interaction, a train of density spikes separated by the optical period $T = 2.66\,\mathrm{fs}$ is formed. **b** The corresponding Wigner function, clearly picturing the sinusoidal phase modulation, exhibits substantial shearing at the temporal focus (1.8 mm propagation distance). **c,d** Marginal distributions showing the energy spectrum and temporal envelope, respectively. For $g = 5.7$ and $\lambda = 800\,\mathrm{nm}$, density spikes shorter than 100 as (FWHM) are produced. Reprinted with permission from Ref. [28].

In analogy to Fresnel diffraction from a spatial grating, the temporal reshaping can be regarded as the result of near-field diffraction in time from a temporal phase-grating. In fact, the same pattern as depicted in Fig. 1.8**a** would be observed as a near-field diffraction pattern for a planar light wave diffracted from e.g. a glass plate with sinusoidally varying thickness. The temporal focus position for typical coupling strengths g achievable in our experiments lies about one to two millimetres downstream the interaction region, i.e., well within reach of a TEM sample holder. According to the Talbot effect [104, 105], the pattern is periodic in propagation direction, and multiple recurrences of the caustics are expected at larger distances.

For electron pulse durations larger than the optical period, a train of attosecond pulses is produced. Using pre-compression stages in the microwave and THz domain as mentioned above, the generation of single attosecond electron pulses should be feasible. The experimental realisation of sub-cycle temporal shaping of free-electrons and characterisation of the resulting pulse trains using quantum state tomography for free-electrons will be presented in Chap. 3.

Chapter 2

Ramsey-type Phase Control of Free-Electron Beams

K. E. Echternkamp, A. Feist, S. Schäfer and C. Ropers
Nature Physics **12**, pp.1000-1004, August 2016
DOI: 10.1038/nphys3844

Quantum coherent evolution, interference between multiple distinct paths [106–109] and phase-controlled sequential interactions are the basis for powerful multidimensional optical [110] and nuclear magnetic resonance [108] spectroscopies, including Ramsey's method of separated fields [111]. Recent developments in the quantum state preparation of free electrons [28] suggest a transfer of such concepts to ultrafast electron imaging and spectroscopy.

Here, we demonstrate the sequential coherent manipulation of free-electron superposition states in an ultrashort electron pulse, using nanostructures featuring two spatially separated near-fields with polarization anisotropy. The incident light polarization controls the relative phase of these near-fields, yielding constructive and destructive quantum interference of the subsequent interactions. Future implementations of such electron-light interferometers may provide access to optically phase-resolved electronic dynamics and dephasing mechanisms with attosecond precision.

A central objective of attosecond science is the optical control over electron motion in and near atoms, molecules and solids, leading to the generation of attosecond light pulses or the study of static and dynamic properties of bound electronic wavefunctions [1, 112–114]. One of the most elementary forms of optical control is the dressing of free-electron states in a periodic field [115, 116], which is observed, for example, in two-colour

ionization [117, 118], free-free transitions near atoms [115, 119], and in photoemission from surfaces [120–123]. Similarly, beams of free electrons can be manipulated by the interaction with optical near-fields [27, 28, 31, 46, 124]. In this process, field localization at nanostructures facilitates the exchange of energy and momentum between free electrons and light. In the past few years, inelastic electron-light scattering [31, 124, 125] found application in so-called photon-induced near-field electron microscopy [27, 28, 32, 126], the characterization of ultrashort electron pulses [31, 46], or in work towards optically-driven electron accelerators [89, 127]. Very recently, the quantum coherence of such interactions was demonstrated by observing multilevel Rabi-oscillations in the electron populations of the comb of photon sidebands [28, 124]. Access to these quantum features, gained by nanoscopic electron sources of high spatial coherence [70, 91], opens up a wide range of possibilities in coherent manipulations, control schemes and interferometry with free-electron states.

Here, we present a first implementation of quantum coherent sequential interactions with free-electron pulses. In particular, we employ a nanostructure that facilitates phase-controlled double interactions, leading to a selectable enhancement or cancellation of the quantum phase modulation in the final electron wavefunction. Figure 2.1**a** illustrates the basic principle of our approach: Traversal of the first near-field induces photon sidebands (labelled 2 in Fig. 2.1**a**) to the initially narrow electron kinetic energy spectrum (labelled 1), which correspond to a sinusoidal phase modulation of the free-electron wavefunction. Following free propagation, the electrons coherently interact with a second near-field and, in analogy to Ramsey's method [111], the final electronic state sensitively depends on the relative phase between the two acting fields. In particular, a further broadening (labelled 4) or a recompression (labelled 3) of the momentum distribution can be achieved.

For a single interaction of a free, quasi-monoenergetic electron state with an optical near-field, the resulting final state is composed of a superposition of momentum sidebands associated with energy changes by $\pm N$ photon energies [31, 124], populated with amplitudes A_N according to

$$A_N = \left(\frac{g}{|g|}\right)^N J_N(2|g|), \tag{2.1}$$

where J_N are the N^{th}-order Bessel functions. The dimensionless coupling parameter g describes the efficiency of momentum exchange with the electron and scales linearly with

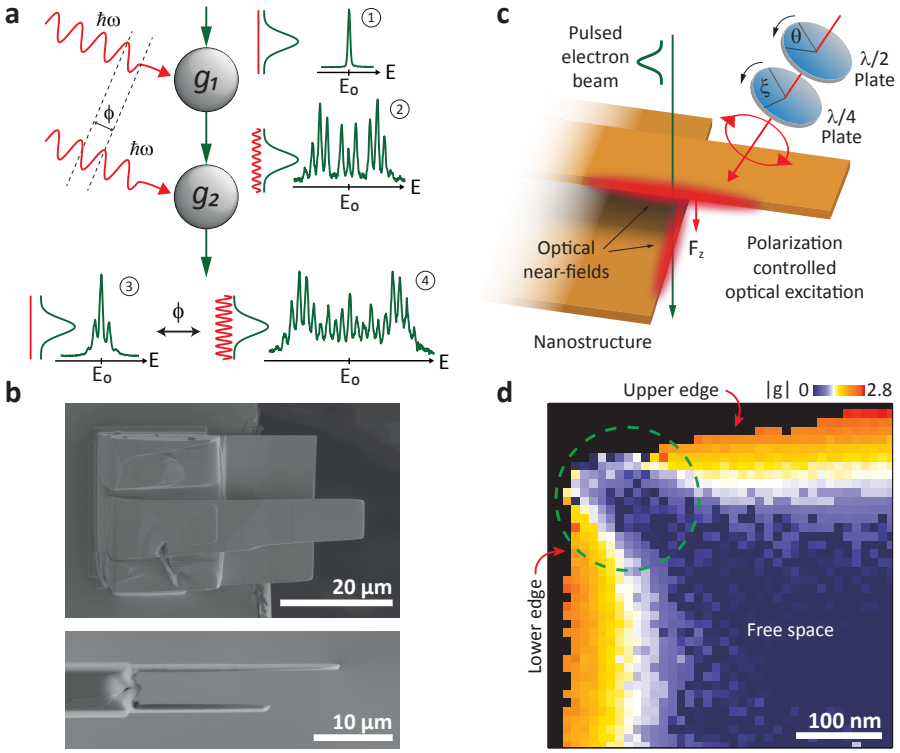

Figure 2.1: **a**, Working principle of the Ramsey-type free-electron interferometer: an electron pulse (green) is acted on at two spatially separated nodes g_1 and g_2. A sinusoidal phase modulation is imprinted onto the electron wavefunction during the first interaction, leading to the generation of spectral sidebands. The relative phase of the interactions governs the phase modulation of the final state. 1 to 4: Experimental electron energy spectra. 1, Incident spectrum. 2, Spectrum for a single interaction. 3, 4, Spectra recorded for destructive and constructive double interactions, respectively. **b**, Scanning electron micrographs of the nanostructure featuring two interaction zones (top and side view). Distance between gold paddles: 5 µm. **c**, Sketch of the experimental scenario displaying polarization-controlled excitation of the nanostructure. **d**, Raster-scanned image of the local coupling strength $|g_{\mathrm{tot}}|$ (see text) for excitation conditions near complete recompression in the corner region (green dashed circle, wave plate angles $\theta = -38°$, $\xi = 26°$, see Fig. 2.3**b**).

the longitudinal vector component of the optical near-field amplitude, i.e., the electric field component parallel to the electron trajectory (denoted F_z in Fig. 2.1**c**; see also Methods 'Sinusoidal phase modulation'). In the spatial representation of the free-electron state, this Bessel-type distribution of sideband amplitudes is manifest in a sinusoidal modulation of the phase of the wavefunction in the form[31]

$$\psi_{\mathrm{fin}} = \exp\left(2i|g|\sin\left(\frac{\omega z}{v} + \arg(g)\right)\right)\psi_{\mathrm{in}}, \tag{2.2}$$

where ψ_{in} and ψ_{fin} are the initial and final state wavefunctions, respectively, and z the spatial coordinate along the electron trajectory.

In the present experiment, schematically depicted in Figs. 2.1**a**,**c**, we demonstrate that two spatially separated optical near-fields may cause an overall interaction of strength g_{tot}, which is describable as the coherent sum of the individual, generally complex-valued interactions g_1 and g_2,

$$g_{\mathrm{tot}} = g_1 + e^{i\varphi_0} g_2, \tag{2.3}$$

where φ_0 is a constant phase offset that depends on the spatial separation of the interaction regions (see Methods 'Sinusoidal phase modulation', 'Coordinate system and geometric phase offset'). In terms of the spatial wavefunction, this then corresponds to an overall enhancement or cancellation of the subsequent interaction-induced phase modulations (eq. 2.2).

The desired control over g_{tot} requires the ability to separately address the two near-fields in a phase-locked manner. We achieve this by tailoring the nanostructure geometry, employing the strong polarization anisotropy of a pair of perpendicular plates (Fig. 2.1**b**). This approach allows us to control the near-field strengths and their relative phase by selecting the polarization state of the overall excitation. In the following, we describe the experimental implementation of this principle.

A narrow beam of ultrashort electron pulses passes the optically excited nanostructure in close vicinity (Fig. 2.1**c**). The final electronic state resulting from inelastic electron-light scattering is analysed by electron spectroscopy upon a systematic variation of the incident light polarization. The polarization state is described by the Jones vector $\vec{J}$, which we set in the standard fashion[128] by the combination of a half- and quarter wave plate at rotation angles θ and ξ, respectively. The Jones vector for sample excitation is then given by the product of the initial (in our case diagonal) polarization state and wave plate Jones matrices M, scaled by the field strength F=0.08 V/nm: $\vec{J} = F \cdot M_{\lambda/4}(\xi) \cdot M_{\lambda/2}(\theta) \cdot \frac{1}{\sqrt{2}} \begin{pmatrix} 1 & 1 \end{pmatrix}$.

In a first set of measurements, the near-field responses of the two nanoscopic plates to the incident polarization state are independently characterized. To this end, the electron beam is placed close to each of the edges, and distant from the corner (red, blue circles in Fig. 2.2**f**), such that the electrons only traverse one of the two near-field regions in each case. Figures 2.2**a**,**b** display electron spectra for a continuous variation of

polarization states (achieved by wave plate rotation), including polarizations parallel and perpendicular to the plates. The widths of these spectra directly reflect the respective coupling constants $g_{1,2}$, as the highest populated sideband is given by $2|g|$ [28]. It is evident that both edges exhibit strong near-fields only for excitation conditions with polarization perpendicular to the respective edge orientation. This behaviour can be regarded as a linear analyser response, in which each edge projects the incident polarization state onto a quasi-polarizability $\vec{\alpha}_{1,2}$, yielding scalar coupling constants $g_{1,2} = \vec{\alpha}_{1,2} \cdot \vec{J}$. By the design of the structure, the vectors $\vec{\alpha}_{1,2}$ are linearly independent, in fact nearly orthogonal, which allows for separate amplitude and phase control.

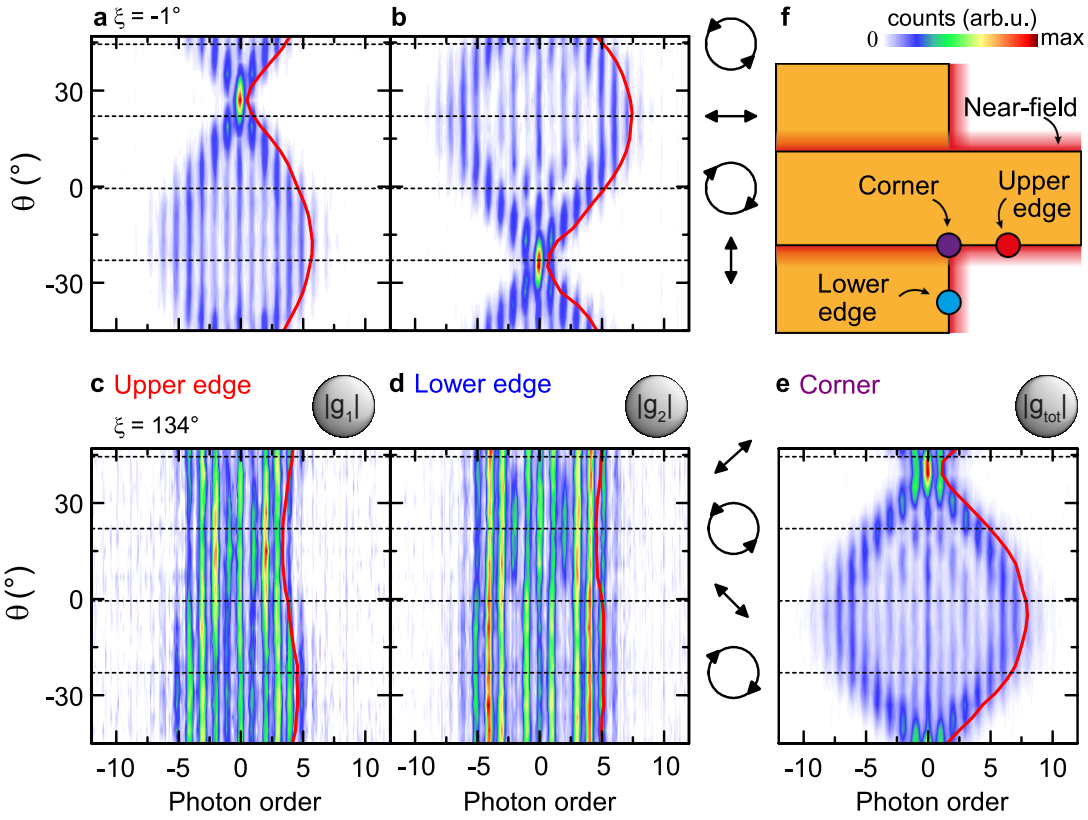

Figure 2.2: a-e, Electron spectra recorded at different positions on the sample for varying incident polarization states (arrow icons). Red lines: coupling constant $2|g_{1,2}|$ extracted from the spectra (see text). The upper (lower) edge yields maximum interaction strength for vertical (horizontal) incident polarization. For polarization states varying from diagonal to circular, nearly constant interaction strengths at the individual edges are observed. At the corner, the associated change of relative phase of the interactions $|g_1|$ and $|g_2|$ leads to a strong modulation in $|g_{\mathrm{tot}}|$, demonstrating the coherent actions of g_1 and g_2. **f**, Illustration of the three different measurement positions leading to single (red, blue circles) and double interaction (purple).

To demonstrate a modulation of the total coupling constant g_{tot} by mere manipulation of the relative phase of the interactions g_1 and g_2, we vary the incident polarization state in such a way as to keep the projections onto the vertical ($\sim |g_1|$) and horizontal ($\sim |g_2|$) axes fixed. This is the case for all elliptical polarization states with main axes rotated by 45° with respect to the edges, including ±45° linear as well as left- and right-hand circular polarizations. Figures 2.2**c** and **d** display the nearly constant coupling strengths at the individual edges resulting from this pure phase variation. Placing the beam at the corner, however, such that it sequentially interacts with both near-fields, we find a strong change in the spectral width of the final electronic state upon a variation through the same set of polarization states (Fig. 2.2**e**). This conclusively demonstrates the quantum coherence and thus reversibility of the two subsequent interactions. Specifically, a strong recompression of the spectrum is achieved near $\theta = 39°$. In the spatial wavefunction picture, this corresponds to a cancellation of the initially imprinted phase modulation by the second interaction. The effect of sequential coherent interactions can also be illustrated by spatial maps, in which the total coupling constant is displayed as a function of beam position near the nanostructure (Fig. 2.1**d**). The individual edges exhibit largely homogeneous coupling constants decaying over a distance of about 100 nm away from the edge (orange regions). In addition, for a destructive relative phase of the individual interactions, a substantially reduced total coupling constant is evident near the corner, at which the electrons traverse both near-fields (green dashed circle).

In order to identify the individual near-field responses, we map the interaction strength for arbitrary incident polarization states by a systematic variation of both wave plate angles. Figure 2.3**a** displays the measured coupling constants g_1, g_2, and g_{tot}, with higher-resolved lineouts in Figs. 2.3**c**,**d** (symbols). For the individual edges (left and middle in Fig. 2.3**a**, red and blue symbols in Figs. 2.3**c**,**d**), we obtain quasi-polarizabilities $\vec{\alpha}_{1,2} = \alpha_{1,2}\vec{n}_{1,2}$ with the normalized projection vectors $\vec{n}_1 = \begin{pmatrix} 0.09+0.14i & 0.99 \end{pmatrix}$ and $\vec{n}_2 = \begin{pmatrix} 0.99 & -0.05-0.07i \end{pmatrix}$, close to the design aim of $\begin{pmatrix} 0 & 1 \end{pmatrix}$ and $\begin{pmatrix} 1 & 0 \end{pmatrix}$, and amplitude prefactors of $\alpha_1 = 35\,(\mathrm{V/nm})^{-1}$ and $\alpha_2 = 44\,(\mathrm{V/nm})^{-1}$. The arbitrary overall phase of both vectors was chosen to yield real values for the respective dominant element. While the vectors $\vec{n}_{1,2}$ are universal and spatially independent for each of the edges, the specific prefactor sensitively depends on the particular distance from the respective surface. Employing amplitudes $\alpha_1 = 52\,(\mathrm{V/nm})^{-1}$, $\alpha_2 = 29\,(\mathrm{V/nm})^{-1}$ and a constant phase offset $\varphi_0 = 1.30$, the entire set of measurements near the corner of the structure is successfully

described by a summation $g_{\mathrm{tot}} = (\vec{\alpha}_1 + e^{i\varphi_0} \cdot \vec{\alpha}_2) \cdot \vec{J}$, again clearly demonstrating the phase-controlled quantum coherent interaction with both near-fields. Minor deviations, for example in the incomplete spectral recompression near the minima of g_{tot}, are attributed to a spatial average over near-field strengths across the electron beam (see Methods 'Determination of coupling constant and spatial averaging'). This leads to small residual sideband populations and highlights the importance of carrying out such experiments with low emittance electron beams, as performed here, using nanotip sources. Dispersive reshaping of the wavefunction, on the other hand, can be excluded for the given spatial separation of the interaction planes (see Methods 'Influence of dispersion').

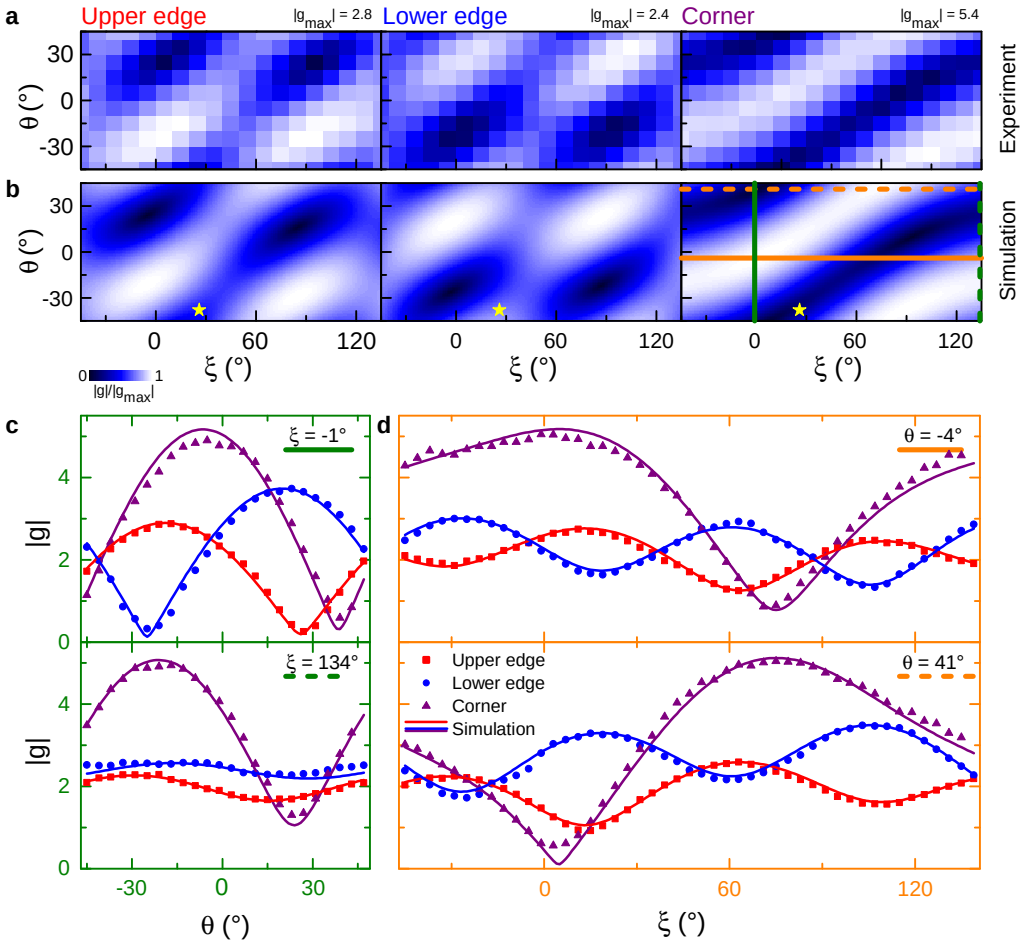

Figure 2.3: **a**, Coupling constant from experimental electron energy spectra measured for individual (left, middle) and combined (right) near-field actions. **b**, Corresponding simulations employing experimentally determined near-field responses $\alpha_{1,2}$ (left, middle) and their coherent sum (right). Yellow star: settings for raster scan in Fig. 2.1**d**. **c**,**d**, Higher-resolved lineouts of experimental coupling constant $|g|$ (symbols) and model prediction (solid lines). The position of the lineouts are indicated by dashed and solid lines in **b**.

A comment should be made about the invoked phase offset φ_0. The precise polarization state at which maximum recompression occurs is governed by the phase relation between the optical far-field and the respective near-fields, and the phase lag arising from the electron and light propagation between the two interaction planes. Although these phases are physically distinct, in practice, they can be combined in the single phase offset φ_0, which is sufficient to account for all experiments. For the present measurements, we identify this phase with a precision that corresponds to a timing uncertainty of a few attoseconds. This implies a sensitivity of the scheme to phase or timing changes to the free-electron wavefunction of this very same magnitude, rendering the presented interferometer an ideal tool to study excitation-induced phase shifts in new forms of electron holography employing the longitudinal degree of freedom. Utilizing this approach to imprint phase information onto the electron wavefunction could be translated to attosecond temporal resolution by, for example, energy-resolved electron diffraction.

Whereas the present work considers the longitudinal momentum, the transverse momentum component can also be accessed in coherent control experiments, for example, by multiple Kapitza-Dirac interactions [129] or diffraction from surface plasmon waves [130]. Similarly, coupling to both transverse momentum components will allow for the optical preparation of free-electron angular momentum states in chiral near-fields [131]. More generally, the absence of efficient decoherence mechanisms in vacuum renders free-electron wave packets an ideal system for coherent control schemes, which can be extended to multi-colour approaches and additional interaction stages. Future experiments may utilize this type of 'electron-light interferometer' by inserting optically excited materials in the gap for precision measurements of electronic dephasing with sub-cycle resolution. Various further applications include phase-resolved near-field imaging, possible quantum computation schemes using free electrons, or the tailored structuring of electron densities in accelerator beamlines with attosecond accuracy.

2.1 Methods

The experiments were performed in a recently developed ultrafast transmission electron microscope, featuring a nanoscale photoemitter as a pulsed electron source for electron pulses with high spatial coherence. Specifically, ultrashort electron pulses are generated by localized photoemission from a ZrO/W tip emitter, accelerated to a kinetic energy of 120 keV and focused tightly (with a beam divergence of 5.3 mrad) in close vicinity to a nanostructure. Electron spot diameters down to 3 nm and pulse durations as short as 300 fs were achieved. A scanning electron micrograph of the nanostructure design is shown in Fig. 2.1**b**. The two plates with a distance of 5 µm were milled by a focused ion beam from a single, annealed gold wire (30 µm diameter). The experimental scenario is sketched in Fig. 2.1**c**: a pump laser beam (800 nm wavelength, dispersively stretched to a pulse duration of 3.4 ps, 250 kHz repetition rate, 23 mW average power) passes a half- and a quarter-wave plate for polarization control and is focused onto the sample to a spot diameter of about 50 µm (full-width at half-maximum). The electron kinetic energy spectra are recorded with an electron energy loss spectrometer.

2.1.1 Sinusoidal phase modulation

To obtain the electron wavefunction $\psi(z,t)$ after interaction with the optical near-fields, we apply the scattering (S-matrix) approach in the interaction picture (see also ref. [28]). The final wavefunction is given by $|\psi(z,\infty)\rangle = S\,|\psi(z,-\infty)\rangle$ with the time-ordered unitary operator

$$S = T\exp\left(-\frac{1}{\hbar}\int_{-\infty}^{\infty} H_{\mathrm{int}}\mathrm{d}t\right) \tag{2.4}$$

and the interaction Hamiltonian

$$H_{\mathrm{int}} = -veA(z,t) \tag{2.5}$$

where v is the electron velocity and e is the electron charge. The vector potential $A(z,t)$ for the two near-fields separated by the distance L is given by

$$A(z,t) = \frac{F_1(z)}{\omega}\sin(\omega t) + \frac{F_2(z-L)}{\omega}\sin\left(\omega\left(t-\frac{L}{v}\right)-\varphi\right) \tag{2.6}$$

φ denotes the phase lag of the second near-field induced by the optical path length dif-

ference of the driving laser field (corresponding to d_l in Supplementary Fig. 2.5). For the wavefunction after interaction we obtain

$$\begin{aligned}
\psi(z,t) &= \exp\left(\frac{iev}{\hbar}\int_{-\infty}^{t} A(z+v\tau,\tau)\mathrm{d}\tau\right)\psi(z,-\infty) \\
\Rightarrow \psi(z,+\infty) &= \exp\Big(2i|g_1|\sin\left(\frac{\omega z}{v}+\arg(g_1)\right) \\
&\qquad +2i|g_2|\sin\left(\frac{\omega z}{v}+\arg(g_2)+\varphi\right)\Big)\psi(z,-\infty) \\
\Leftrightarrow \psi(z,+\infty) &= \exp\left(2i\mathrm{Im}\left(e^{i\frac{\omega}{v}z}\left(g_1+e^{i\varphi}g_2\right)\right)\right)
\end{aligned} \tag{2.7}$$

In the second step, we introduced the coupling constant $g = e/2\hbar\omega\int_{-\infty}^{\infty}F(z)\exp(-i\Delta kz)\mathrm{d}z$, as in ref. [31]. It is proportional to the spatial Fourier component of the longitudinal vector component of the near-field F(z) along the electron trajectory at the spatial frequency $\Delta k = \omega/v$, which corresponds to the momentum change of an electron at velocity v gaining or losing an energy $\hbar\omega$. Equation 2.7 evidences that the interaction of the free electrons with the two optical near-fields is describable as a single sinusoidal phase modulation of the electron wavefunction and that the two consecutive interactions coherently add up in the way stated in equation 2.3 in the main text.

2.1.2 Influence of dispersion

Between the two interaction regions, the electron wavefunction propagates in free space. The momentum-dependent propagation operator is given by

$$T(p) = \exp\left(-\frac{i}{\hbar}\left(\frac{m_e c^2}{\gamma}+\frac{\Delta p^2}{2\gamma^3 m_e}\right)t\right) \tag{2.8}$$

where γ is the Lorentz factor and Δp is the momentum change due to the interaction with the optical near-field, with Δp given by $N\hbar\omega/v$ for the N^{th}-order sideband. During free propagation, the sideband orders acquire different phases, which leads to a dispersive reshaping of the electron wavefunction and, at a certain propagation distance, to a temporal focusing into a train of attosecond pulses [28]. In the present study, the propagation distance is much shorter than the distance to the temporal focus (typically millimetre scale). Specifically, the experimental parameters employed here (coupling constants $g \approx 5$, propagation distance $L = 6\,\mu\mathrm{m}$, $v = 0.6c$, $\gamma = 1.24$) yield very small sideband-dependent phase shifts on the order of $N^2 \cdot 0.17\,\mathrm{mrad}$, such that dispersive effects are negligible.

2.1.3 Coordinate system and geometric phase offset

The angles θ and ξ define the orientation of the fast axes of the wave plates relative to the horizontal x axis of the coordinate system, which is indicated by black arrows in Supplementary Fig. 2.4**a**. The wave plate setting $\theta = \xi = -45°$, for example, yields linear laser polarization at $-45°$ to the x axis.

In the following, we discuss the influence of the sample and beam geometry on the constant phase offset φ_0. The difference in electron group and laser phase velocity leads to a phase lag, which can be calculated as follows: for a given plate distance d, the electron and laser path lengths are $d_e = d/\cos\alpha$ and $d_l = d\cos\beta/\cos\alpha$, respectively, where $\alpha = 37°$ is the sample tilt angle and $\beta = 55°$ is the angle between laser and electron beam. The path length difference corresponds to a timing difference of

$$\Delta t = \frac{d_e}{v_e} - \frac{d_l}{c} = \frac{d}{\cos\alpha c} \tag{2.9}$$

with $v = 0.6c$. A small variation of α by about 2.4° shifts Δt by a quarter laser period, that is, φ_0 by 90°. Sample tilting thus presents a convenient way to externally control φ_0. Note that the data displayed in Figs 2.2**e** and 2.3**c** in the main text were recorded at two slightly different sample tilts, resulting in a relative phase shift of $\Delta\varphi = 81.5°$.

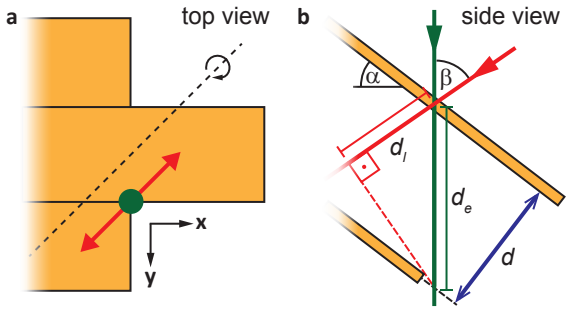

Figure 2.4: Sample and beam geometry. **a** Top view. Black arrows: coordinate system. Red arrow: incident polarization for wave plate angles $\theta = \xi = -45°$. **b** Side view. The laser bam (red) is focused onto the sample at an angle of $\beta = 55°$ with respect to the electron beam (green). The sample is tilted by $\alpha = 37°$ (around the dashed black line in **a**). The plate distance $d = 5\,\mu\text{m}$ determines electron and laser path lengths, d_e and d_l, respectively.

2.1.4 Determination of coupling constant and spatial averaging

In principle, the coupling constants can be inferred from the cutoff energy of the electron energy spectra, which is given by $2|g|\hbar\omega$ (ref. [28]). For a more precise determination, we extracted coupling constants from a fit of Bessel amplitudes to the data, according to equation 2.1. Due to the finite electron beam size, a small spatial average over different coupling constants needs to be taken into account, for which we adopt a Gaussian distribution of the electron intensity in the beam. At the gold edges, the near-field strength can be regarded as homogeneous in directions parallel to an edge, and exponentially decaying along the perpendicular direction (see Supplementary Fig. 2.5**g**). In this case, the probability distribution of coupling constants is given as

$$P(g) \propto \frac{1}{g} \cdot \exp\left(-\frac{1}{2}\left(\frac{l}{\Sigma}\ln\left(\frac{g_0}{g}\right)\right)^2\right) \tag{2.10}$$

where g_0 is the expectation value of the coupling constant, l is the decay length of the near-field strength and Σ is the electron beam width (standard deviation). For the analysis, we consider a constant ratio l/Σ for each near-field.

When averaging is taken into account, the experimental data are well reproduced. A comparison of Supplementary Figs 2.5**c**, **e** illustrates that spatial averaging only weakly affects the visibility of quantum coherent features in the electron energy spectra (see ref. [28]). The spectra recorded at the upper edge show stronger averaging compared with the lower edge, since the electron focus is not perfectly centred between the two edges (small displacement Δz). For the data set shown here, we obtain $l/\Sigma_U \approx 5$ and $l/\Sigma_L \approx 10$. Together with the near-field decay length of $l \approx 90\,\mathrm{nm}$ (determined from the raster scan in Fig. 2.1**d**), we find $\Sigma_U = 18\,\mathrm{nm}$ and $\Sigma_L = 9\,\mathrm{nm}$, in accordance with the electron focal spot diameter of 8 nm used in the experiment.

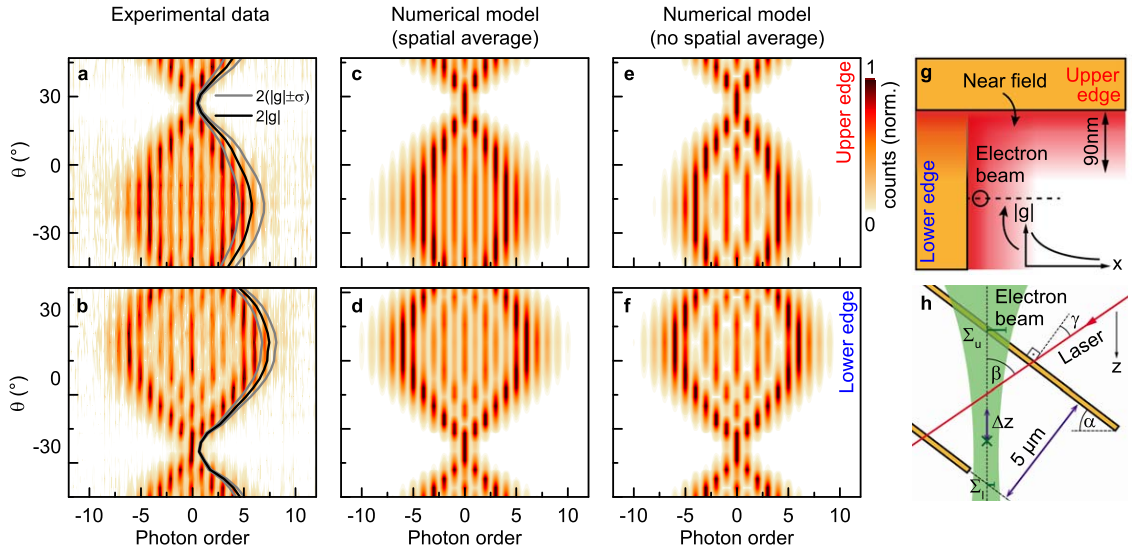

Figure 2.5: Determination of coupling constant and spatial averaging. **a,b** Experimental electron spectra (normalized to the maximum count rate for clarity) recorded at the upper and lower edge for varying half wave plate angles θ (quarter wave plate at $\xi = -1°$). **c-f** Bessel amplitudes adapted to the experimental data (with and without spatially averaged coupling constants, respectively). Black and gray curves in **a,b**: Expectation value of coupling constant and its standard deviation (linearly depending on $|g|$, $\sigma_U = 0.21|g|$ and $\sigma_L = 0.09|g|$). **g** Sketch of the experimental geometry (top view). The coupling constant decays exponentially along the black dashed line (decay length $l \approx 90\,\mathrm{nm}$). All coupling constants within the electron beam (black circle) contribute to the spectra. **h** Sketch of the experimental situation (side view). For experimental angles α and β see Fig. 2.4.

Acknowledgements

We gratefully acknowledge funding by the Deutsche Forschungsgemeinschaft (DFG-SPP-1840 'Quantum Dynamics in Tailored Intense Fields', and DFG-SFB-1073 'Atomic Scale Control of Energy Conversion', project A05). We thank S. V. Yalunin for useful discussions, and M. Sivis for help in sample preparation.

Author Contributions

K.E.E. prepared the nanostructure, conducted the experiments with contributions from A.F., and analysed the data. The manuscript was written by K.E.E. and C.R., with contributions from S.S. C.R. and S.S. conceived and directed the study. All authors discussed the results and the interpretation.

Chapter 3

Attosecond Electron Pulse Trains and Quantum State Reconstruction in Ultrafast Transmission Electron Microscopy

K. E. Priebe, C. Rathje, S. V. Yalunin, T. Hohage, A. Feist, S. Schäfer and C. Ropers
Nature Photonics **11**, pp.793-797, November 2017
DOI: 10.1038/s41566-017-0045-8

Ultrafast electron and X-ray imaging and spectroscopy are the basis for an ongoing revolution in the understanding of dynamical atomic scale processes in matter. The underlying technology heavily rests on laser science for the generation and characterization of ever-shorter pulses. Recent findings suggest that ultrafast electron microscopy with attosecond-structured wave functions may be feasible. However, such future technologies call for means to both prepare and fully analyse the corresponding free-electron quantum states.

Here, we introduce a framework for the preparation, coherent manipulation and characterization of free-electron quantum states, experimentally demonstrating attosecond electron pulse trains. Phase-locked optical fields coherently control the electron wave function along the beam direction. We establish a new variant of quantum state tomography – "SQUIRRELS" – for free-electron ensembles. The ability to tailor and quantitatively map electron quantum states will promote the nanoscale study of electron-matter entanglement and new forms of ultrafast electron microscopy down to the attosecond regime.

Optical, electron and X-ray microscopy and spectroscopy reveal specimen properties via spatial and spectral signatures imprinted onto a beam of radiation or electrons. Leaving behind the traditional paradigm of idealized, simple probe beams, advanced optical techniques increasingly harness tailored probes, or even their quantum properties and probe-sample entanglement. The rise of structured illumination microscopy [7], pulse shaping [5], and multidimensional [67] and quantum-optical spectroscopy [132] exemplify this development. Similarly, electron microscopy explores the use of shaped electron beams exhibiting particular spatial symmetries [133] or angular momentum [87, 134] and novel measurement schemes involving quantum aspects of electron probes have been proposed [135, 136]. Temporal beam shaping may considerably enhance the capabilities of ultrafast electron and X-ray imaging and spectroscopy [68, 69, 137, 138], provided that adequate means to generate [15] and characterize [1, 86, 139] ultrashort probe pulses [13, 69, 140–142] are available. For electron beams, temporal structuring is facilitated by time-dependent fields in the radio-frequency [12, 143, 144], terahertz [15, 102] or optical domains. Notably, light-field control [28, 135, 145] may translate the temporal resolution of ultrafast transmission electron microscopy (UTEM) [10, 146] and electron diffraction (UED) [69, 147], currently at about 200 fs [83] and 20 fs [12, 13], respectively, to the range of attoseconds [28, 148–150]. In this regime, quantum features may be exploited both for the creation and the measurement scheme of the respective attosecond-structured electron probe.

Here, we demonstrate the coherent control and attosecond density modulation of free-electron quantum states using multiple phase-locked optical interactions. Moreover, we introduce quantum state tomography for free electrons, providing crucial elements for ultrafast free-electron quantum optics.

3.1 Multi-Colour Interactions with Free-Electron Beams

In the first set of experiments, (sketched in Fig. 3.1**a**), two laser beams at frequencies ω and 2ω are focused onto a single-crystalline graphite flake that is transparent for 120-keV electrons. A pulsed electron beam, generated by an ultrafast field-emission cathode [83], traverses the dual-colour optical near-field, and its kinetic energy spectrum is subsequently recorded. The relative phase between the two laser pulses is precisely controlled by a pair of dispersive wedges. Single-colour excitation (upper two panels in Fig. 3.1**c**) induces spectra with symmetric sideband peaks separated by the respective photon energy,

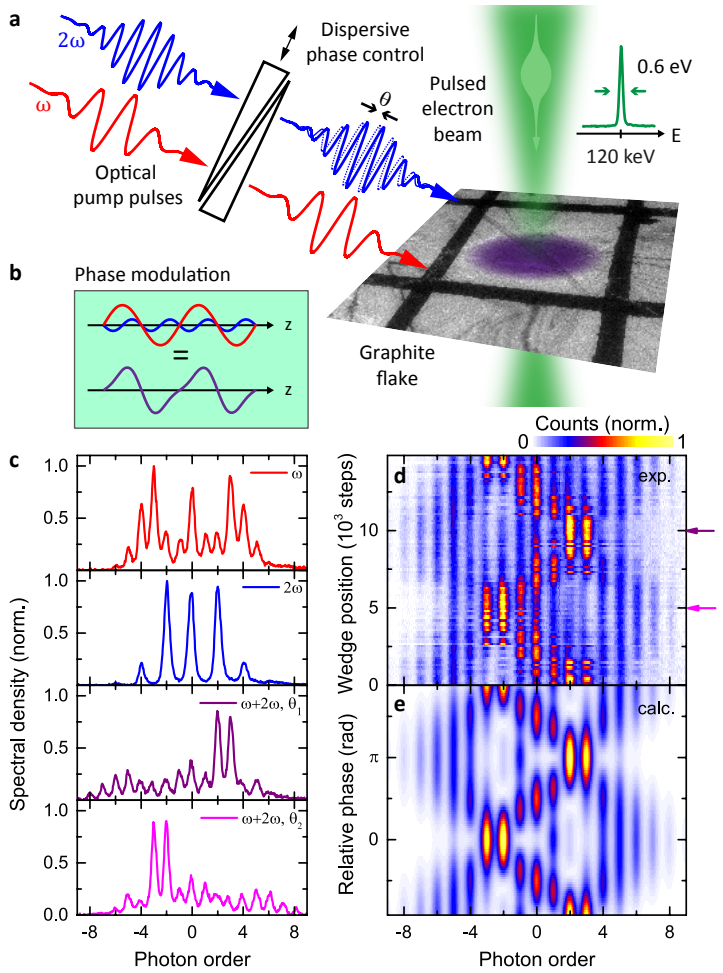

Figure 3.1: Experimental scheme. **a** Optical pump pulses at frequencies ω ($\lambda = 800\,\text{nm}$) and 2ω ($\lambda = 400\,\text{nm}$) are spatially and temporally overlapped with a pulsed electron beam on a single-crystalline graphite flake. Fused silica wedges are used to control the relative phase between the laser pulses. An electron-energy-loss spectrometer (EELS) records the electron energy spectrum, which initially exhibits a narrow peak at a central energy of 120 keV and an energy width of 0.6 eV. **b** The electron-light-interaction can be described as a phase modulation of the electron wavefunction. For two-colour laser fields, the phase modulation becomes non-sinusoidal (purple curve). **c** Experimental electron energy spectra recorded for single-colour (red and blue curves) and two-colour excitation (purple and magenta curves). In the latter case, the spectra are strongly asymmetric and depend on the relative phase of the two colours ($\theta_1 = \pi$, $\theta_2 = 0$). **d** The measured spectral shape oscillates back and forth for varying wedge insertion. The spectra in **c** are taken from the positions marked by the purple and magenta arrows. **e** The corresponding calculated spectra (Eq. 3.2) using coupling constants $g_\omega = 2.20$ and $g_{2\omega} = 0.76$ for the fundamental and second harmonic, respectively. Contributions from low-loss plasmon bands were subtracted from all spectra. Note that, throughout the paper, the photon order refers to the energy gain in integer multiples of $\hbar\omega$.

as previously reported in the context of photon-induced near-field electron microscopy (PINEM) [27, 28, 31, 32, 124] and free-electron Rabi-oscillations [28, 135]. Coupled to both near-fields, however, the electron spectrum develops a strong asymmetry (lower two panels in Fig. 3.1**c**) towards energy gain or loss, controlled by the relative phase of both fields (cf. Fig. 3.1**d**).

These observations can be rationalized by adapting the theoretical description of inelastic electron-light scattering [28, 31, 124, 135, 151] to the present two-colour scenario. For interaction with a single light field at frequency ω, the spatial wavefunction of the free-electron quantum state $|\psi\rangle$ experiences a sinusoidal phase modulation in the beam direction [28, 31],

$$\psi(z) = \exp\left(-2i|g_\omega|\sin\left(\frac{\omega z}{v} + \arg(\mathrm{g}_\omega)\right)\right)\psi_{\mathrm{in}}(z) =: A(g_\omega,\omega)\psi_{\mathrm{in}}(z). \tag{3.1}$$

Here, $\psi_{\mathrm{in}}(z)$ denotes the wavefunction of the unperturbed electron quantum state (leaving out dependencies on transverse coordinates for simplicity), v the electron velocity, z the spatial coordinate along the electron trajectory, and g_ω is a dimensionless coupling constant as defined in Refs. [28, 31]. Equivalently, the quantum state can be written as a coherent superposition of momentum sidebands [28, 31, 124]. The action of two fields at frequencies ω and 2ω is now described in terms of two superimposed phase modulations, which for the typically small total energy changes (relative to the initial electron energy) results in the electron quantum state

$$\psi_{\mathrm{out}}(z) = A(g_\omega, 2\omega)\psi_{\mathrm{in}}(z), \tag{3.2}$$

where g_ω and $g_{2\omega}$ are the two complex coupling constants. Overall, the dual phase modulation is non-sinusoidal (cf. Fig. 3.1**b**), resulting in the observed asymmetric electron spectra. The phase-dependent experimental spectrograms (Fig. 3.1**d**) are reproduced by a cycling of the relative phase $\theta = \arg(\mathrm{g}_\omega) - \arg(\mathrm{g}_{2\omega})/2$ in Eq. 3.2. A rich variety of tailored quantum states is accessible by variation of the relative phase and amplitudes of such bichromatic fields, and a further design of such momentum state synthesis may be realized by optical pulse-shaping techniques [152].

3.2 SQUIRRELS: Free-Electron Quantum State Reconstruction

Multiple phase-controlled interactions at one or more frequencies not only enable the preparation but also the characterization of free-electron quantum states, as we demonstrate in the following. Slightly shifting our perspective on the experimental scenario, we now regard the interaction of the electron with the 2ω-field as the preparation of a specific quantum state, described by a density operator ρ to account for the possibility of mixed states, which is then probed by the ω-field. Based on this interpretation, we introduce a new variant of quantum state tomography [47, 51] termed "Spectral QUantum Interference for the Regularised Reconstruction of free-ELectron States", abbreviated as "SQUIRRELS". As illustrated in Fig. 3.2**a** and detailed in the Methods (Section 3.5.3), SQUIRRELS reconstructs the free-electron density matrix ρ in the longitudinal momentum basis from experimental spectrograms. Specifically, the action of the ω-field on ρ, described by a unitary transformation U, results in a final quantum state ρ_{out} that depends on the relative phase θ,

$$\rho_{\mathrm{out}}(\theta) = U(\theta)\rho U^{\dagger}(\theta) \;\text{ with }\; \langle N|U(\theta)|M\rangle = e^{i(N-M)\theta} J_{N-M}(2|g_{\omega}|). \tag{3.3}$$

Here, the integers N and M label the electron momentum states of the individual photon sidebands (positive/negative for energy gain/loss), denoted "photon order" in the Figures, and J_{N-M} is the Bessel function of the first kind. Note that Eq. 3.3 generalizes Eq. 3.1 to mixed states and treats the ω-field as a type of local oscillator, which in the present context is regarded as an ideal phase modulator. The populations $p_{N,\theta} = \langle N|\rho_{\mathrm{out}}(\theta)|N\rangle$ constitute our observables, namely the phase-dependent sideband intensities in the spectrogram (Fig. 3.2**b**). While the diagonal entries of ρ, namely the populations $\langle N|\rho|N\rangle$ of the prepared quantum state, can be readily measured in a single-colour experiment, the off-diagonal terms or coherences $\langle N|\rho|M\rangle$, $N \neq M$ initially remain unknown and must be reconstructed from the two-colour data $p_{N,\theta}$. In order to obtain the full density matrix ρ, we thus use Eq. 3.3 to solve a linear system of coupled equations, which in mathematical terms is ill-posed. Stable solutions of the resulting (ill-conditioned) matrix equation are achieved by iterated Tikhonov regularization, as detailed in the Methods (Section 3.5.3), employing the positive-semidefiniteness of physical density matrices as a constraint on ρ. We note that the present scenario is closely related to established techniques for the retrieval of spectral phases of ultrashort and attosecond optical pulses, such as FROG

[153] and RABBITT [154]. In the Methods (Section 3.5.5), we also apply RABBITT to reconstruct the free-electron quantum state.

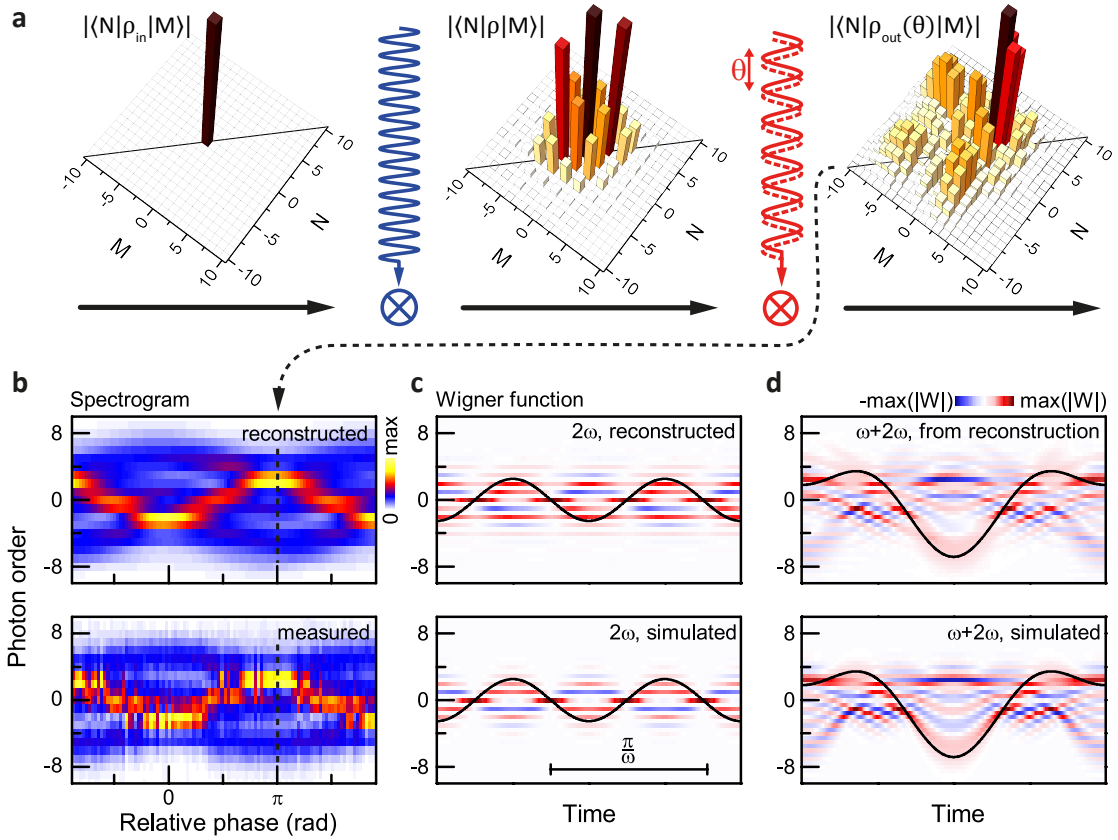

Figure 3.2: SQUIRRELS reconstruction of the free-electron quantum state. **a** Reconstructed density matrices and illustration of the underlying tomographic principle: Preparation of the free-electron quantum state with density matrix ρ is obtained by applying a laser pulse at frequency 2ω to the incident quantum state ρ_{in}. In a second step, a laser pulse at frequency ω and relative phase θ with respect to the first pulse probes the quantum state ρ by transforming it into ρ_{out}. Note that only the populations (diagonal elements, marked by the black line) of the density matrices ρ are accessible in the measurement, the coherences (off-diagonal elements) remain unknown. The shown density matrices ρ and $\rho_{\mathrm{out}}(\theta = \pi)$ were reconstructed from experimental data. **b** Spectrogram containing the phase-dependent populations $\rho_{\mathrm{out}}(\theta)$. Upper panel: reconstructed, lower panel: measured. **c** The reconstructed and simulated Wigner functions for the single-colour quantum state ρ illustrate the sinusoidal phase modulation. **d** Corresponding two-colour Wigner functions for $\rho_{\mathrm{out}}(\theta = \pi)$. The lower panels in **c** and **d** show model calculations for pure quantum states ($g_\omega = 2.16$, $g_{2\omega} = 0.63$). Black solid lines: phase modulation according to Eq. 3.1 or 3.2 as guide to the eye.

Figure 3.2 presents an exemplary SQUIRRELS reconstruction, in the form of Wigner functions [53] of the intermediate (ρ) and final quantum state (ρ_{out}). The Wigner function is a quantum-mechanical quasi-probability distribution in phase space that completely describes the quantum state of the electron ensemble, and whose marginal distributions, i.e., integrals along horizontal and vertical axes, correspond to the density distributions of the longitudinal momentum and position, respectively. Negative values of the Wigner function illustrate the non-classical nature [53, 54] of the electron quantum state. Albeit being equivalent to the density matrix, the Wigner function provides a more intuitive representation by revealing the sinusoidal momentum modulation (Fig. 3.2**c**) induced by the interaction (Further reconstructions at growing field amplitudes are shown in Fig. 3.9). This sinusoidal shape is complemented by a mirrored sinusoidal feature composed of alternating positive (red) and negative (blue) stripes, such that electron energies corresponding to non-integer photon numbers destructively interfere. The non-sinusoidal momentum modulation of the corresponding final two-colour state ρ_{out} is apparent in Fig. 3.2**d**.

3.3 Attosecond Electron Pulse Trains

Instead of employing two-colour fields in a single interaction plane, quantum state reconstruction is also possible by sequential actions in separate planes, either by dual or single-colour fields. In the following, we implement this concept in two scenarios, namely a µm-sized and a millimetre-sized separation of interaction distances. Figure 3.3 presents SQUIRRELS applied to a measurement conducted in the geometry introduced in Ref. [135], with a few-micron distance between two phase-locked near-field interactions of the same frequency. Excellent agreement between the reconstructed density matrix and Wigner function (Fig. 3.3**c**) with a corresponding simulation (Fig. 3.3**d**) is found, with only minor loss of phase coherence indicated by damped elements far off the main diagonal.

We now apply this scheme to experimentally demonstrate the creation of a train of attosecond density spikes, as recently proposed [28]. In the measurements presented in Fig. 3.4, the distance to the second interaction plane is increased to 1.5 mm. This allows for a dispersive reshaping of the electron density by a shearing of the phase-space distribution, as also utilized in accelerator-based applications of longitudinal beam structuring [155, 156]. In Figure 3.4**b**, the final spectrum is displayed as a function of relative phase over multiple cycles. Using SQUIRRELS, we retrieve the corresponding sub-cycle

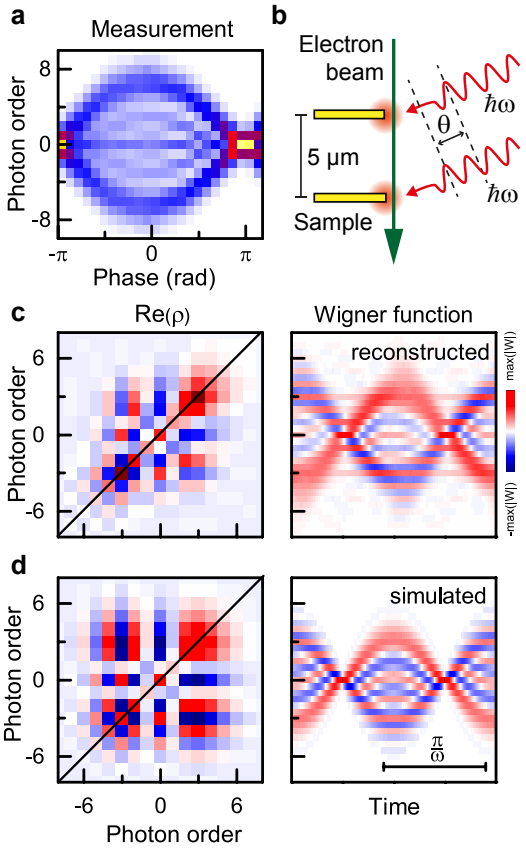

Figure 3.3: Application of SQUIRRELS to spatially separated optical near-fields. **a** Experimental spectrogram (data from structure in Ref. [135]). **b** Sketch of the experimental scenario. **c** Reconstructed density matrix (left) and Wigner function (right) of the electron quantum state prepared by the first optical near-field after free-space propagation over a distance of 5 μm. **d** Corresponding simulations for a pure state with $g = 1.97$.

electron density structure (Fig. 3.4**d**), which exhibits a baseline density at 0.27 of the maximum value, and, notably, a train of attosecond peaks of a width of 655 as (full-width-at-half-maximum; root-mean-square or rms: 277 as). Accordingly, the high-quality Wigner function reconstruction (Fig. 3.4**c**) exhibits a sheared sinusoidal shape, with many fine interference features. From a comparison with model simulations, we estimate that spatial and temporal averaging over different mutual phases in both planes is limited to below 189 mrad (80 as rms, cf. Fig. 3.10). In the present experiments, geometrical constraints limited the dispersive propagation to 1.5 mm, while the shortest attosecond pulses are expected for 2.75 mm propagation for $g_{\mathrm{pump}} = 3.95$. The pronounced attosecond density modulation achieved here will enable the nanoscale exploration of optically-driven, coherent linear and nonlinear electronic charge displacements by electron diffraction and spectroscopy with sub-cycle, attosecond accuracy. In future experiments, a further reduction in pulse duration to less than 100 as seems feasible, employing optimized propagation distances, field strengths and phase stability. Moreover, also the quantitative reconstruction of isolated attosecond electron pulses, generated, for example using pre-compression techniques, will be possible by adapting the approach presented.

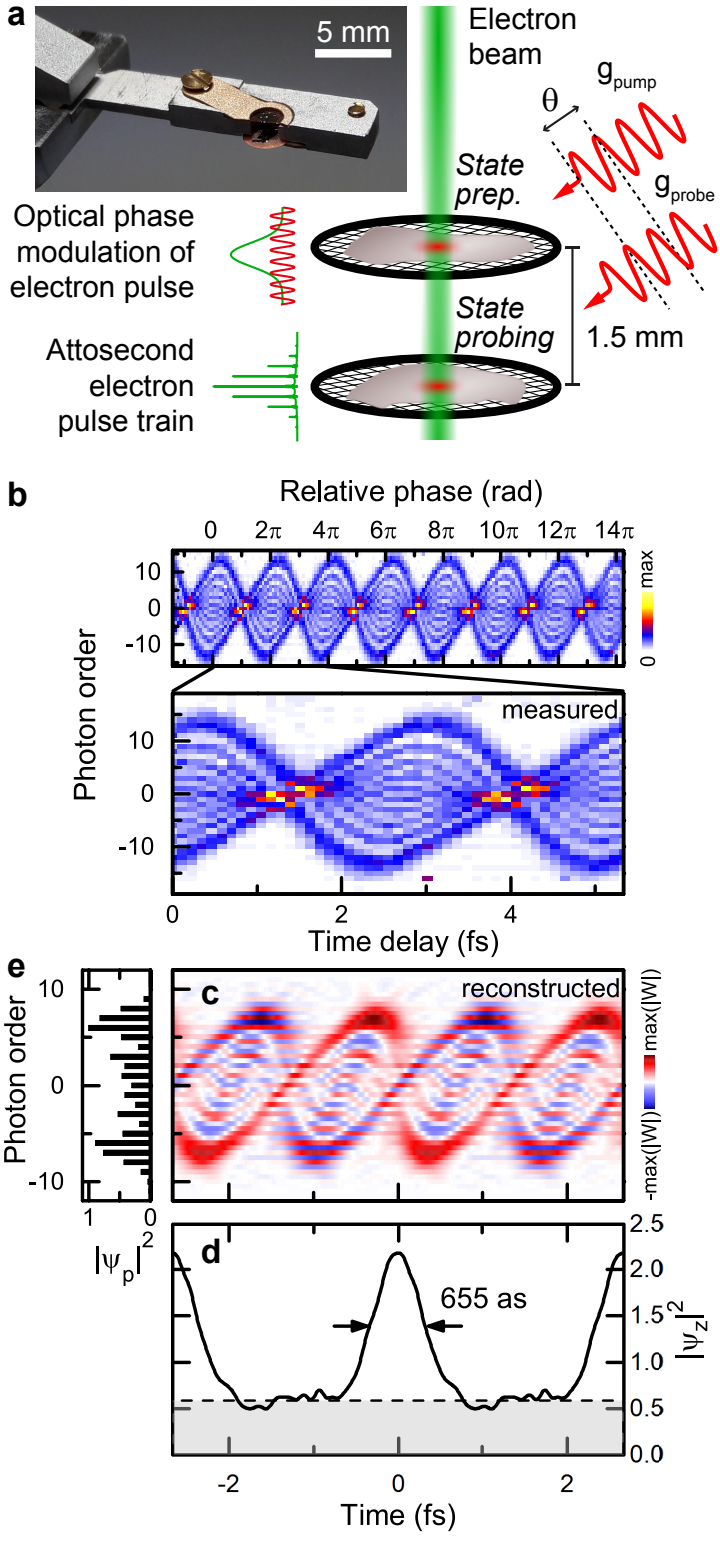

Figure 3.4: Experimental demonstration of attosecond electron pulse trains. **a** Sketch of the experimental setup employing two graphite flakes for the preparation (upper plane) and characterization (lower plane) of attosecond electron pulse trains. Inset: Photograph showing the custom-built TEM sample holder. **b** Experimental spectrogram recorded over multiple optical cycles and close-up of two cycles. **c** The reconstructed Wigner function (using $g_{\mathrm{probe}} = 3.52$) reveals a pronounced shearing due to free-space propagation. **d** The temporal projection of the Wigner function exhibits density modulations with a full-width-at-half-maximum of 655 as (after subtraction of a baseline indicated by the grey-shaded area; rms pulse duration: 277 as). **e** Corresponding electron energy spectrum (momentum projection). The results are in excellent agreement with calculations employing pure states (cf. Fig. 3.10).

3.4 Conclusions

In conclusion, we demonstrated the coherent control, quantum state reconstruction and attosecond structuring of free-electron beams. The approach links ultrafast transmission electron microscopy with tools from both attosecond spectroscopy and quantum optics. We envisage the application of this framework in novel quantum measurement schemes in electron microscopy, yielding structural and electronic observables with nanometre spatial and attosecond temporal resolutions, possibly on the level of single quantum systems. Extending the approach to transverse scattering of electrons will establish the programmable, three-dimensional shaping of free-electron wave packets as a basic element of free-electron quantum optics technology.

3.5 Methods

3.5.1 Experimental Details

The experiments were performed in an ultrafast transmission electron microscope equipped with a nanoscopic tip emitter, as described in detail in Refs. [28, 83, 135]. Figure 3.5 depicts the optical beam path and the interferometer designs used for the two different sets of measurements. A pulsed laser beam from an amplified fs-laser system (250 kHz repetition rate, 800 nm central wavelength, 50 fs pulse duration) is split in two parts, one of which is frequency-doubled in a β-barium borate (BBO) crystal and focused onto a zirconium-oxide covered tungsten tip to generate a pulsed photoelectron beam (probe beam). For the two-colour experiments, an interferometer labelled 'A' in Fig. 3.5 was set up: The second part of the laser beam (pump beam) is frequency-doubled in another BBO crystal and separated into two beam paths at 800 nm and 400 nm wavelength. The 800-nm and 400-nm pump pulses are stretched to a duration of 2.7 ps and 1.3 ps (cf. Fig. 3.6), by propagation through a 19-cm SF6 and a 10-cm BK7 glass slab, respectively. This ensures laser pulse durations exceeding that of the electron pulse, such that the electrons experience a constant near-field amplitude (see Ref. [28]) and the electron-light interaction can be described by a single coupling constant as in Eq. 3.3, a requirement for the present reconstruction algorithm. The two laser beams at frequencies ω and 2ω are recombined and focused onto the sample within the TEM chamber ($\approx 30\,\mu$m spot size) after passing two wedges (fused silica, wedge angle 4°) for precise phase control. No

active phase stabilization was applied. The electron beam (≈ 17 nm focus size) and both pump laser beams are spatially and temporally overlapped on a single crystalline graphite flake (about 100 nm thick), obtained by mechanically cleaving a natural graphite single crystal.

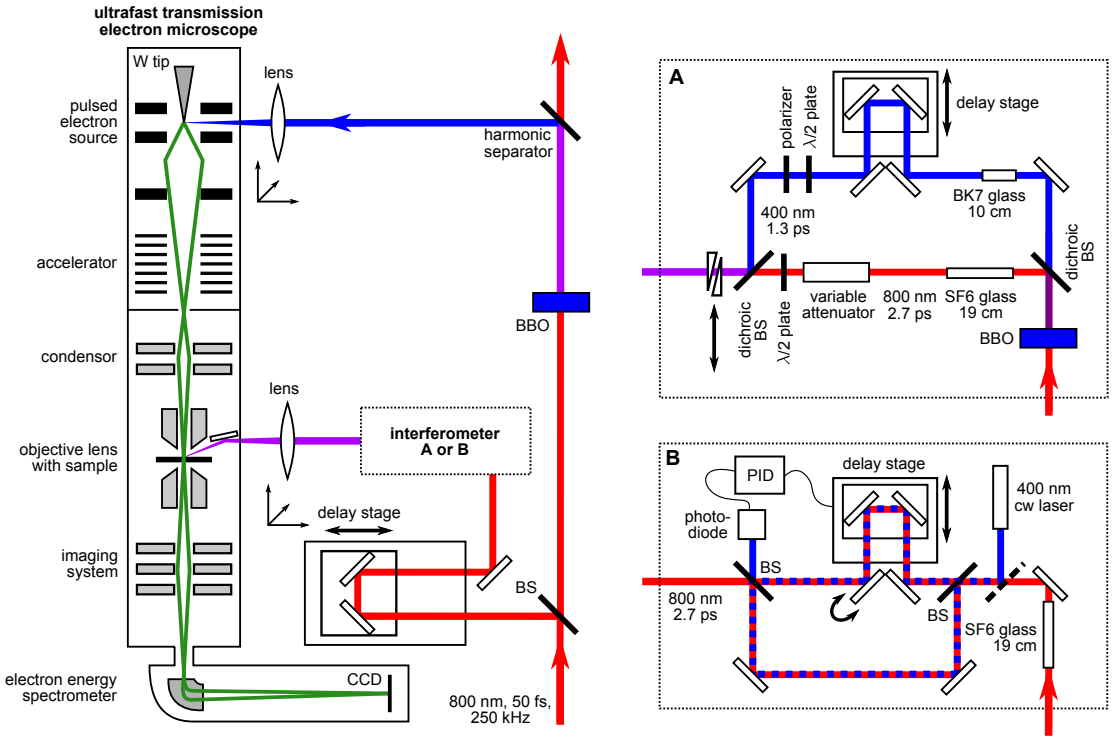

Figure 3.5: Experimental setup. The electron pulses are generated by single-photon photoemission from a heated ZrO/W Schottky-field-emitter using laser pulses at 50-fs pulse duration, frequency doubled to 400-nm wavelength in a BBO crystal. Part of the same laser beam is used for sample excitation to ensure synchronization between the laser-pump and electron-probe pulses. For two-colour excitation (interferometer A), this part of the beam is further split into two parts, one of which is also frequency-doubled. The linear polarization state as well as the laser intensity can be individually adjusted for both colours. After beam recombination, the relative phase between the two pulses is controlled with fused-silica wedges. For the spatially-separated structure, interferometer B is used. A motorized mirror mount in one of the two beam paths allows to create two spatially-separated laser foci within the UTEM. The interferometer is stabilized by a feedback loop (PID control).

To measure the attosecond temporal structuring of the electron density, we implemented a custom TEM holder capable of carrying two TEM grids with single-crystalline graphite flakes, spatially separated by 1.5 mm. A second interferometer (labelled 'B' in

Fig. 3.5) equipped with a motorized mirror mount in one of the interferometer arms allows for an independent control of the laser focus positions on the top and bottom sample planes. The interferometer is actively stabilized using a 400-nm cw-laser. The electron beam diameter was increased to a $\approx 3\,\mu$m focus size to reduce the influence of mutual phase differences between the optical excitation of the top and bottom interaction regions. For both experiments, the resulting electron energy distribution is recorded in an electron spectrometer with 5 s and 40 s integration time, respectively.

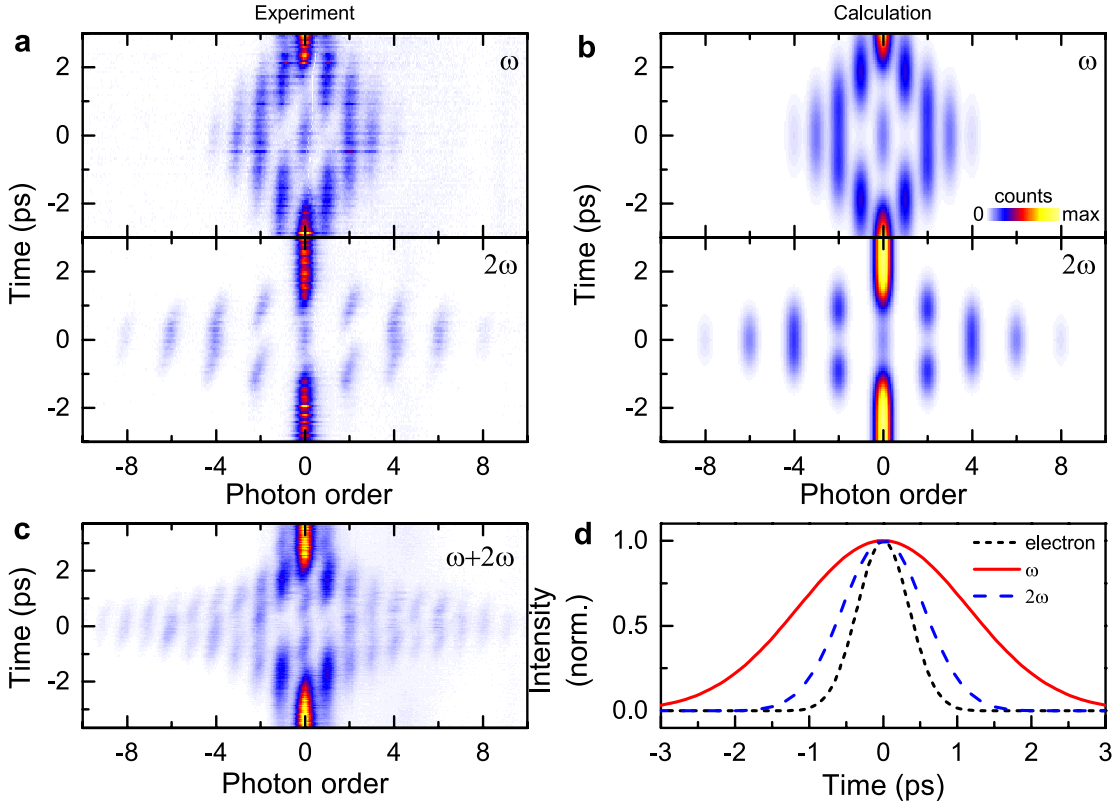

Figure 3.6: Electron-photon cross-correlation. **a** Measured electron energy spectra as a function of the time-delay between the electron and laser pulses at frequency ω (upper panel) and 2ω (lower panel). **b** Corresponding calculations employing Eq. (21) from Ref. [31]. **c** Electron-photon cross-correlation for two-colour excitation to confirm optimized temporal overlap between both laser pulses. **d** Intensity envelopes of the three pulses involved, used for the calculation shown in (**b**). Retrieved pulse durations (FWHM of intensity): 820 fs (electron pulse), 2.7 ps (ω pulse), 1.3 ps (2ω pulse). Electron pulse chirp is not included in the calculation, so that the experimentally observed tilt of the photon sidebands [44] is not reproduced.

3.5.2 Data Analysis

Besides the coherent interaction with the optical near-field, the electron may also interact with the sample itself, e.g. by plasmon excitation, giving rise to a weak, spectrally broad energy-loss feature in the recorded spectra, which was removed from the data. While the energy spectra are recorded with an energy resolution better than the photon energy, we reduce the experimental data to the photon sideband populations for further analysis. To this end, we employ a global fit function consisting of Pseudo-Voigt profiles separated by the photon energy, which are offset by an asymmetric Gaussian describing the plasmon contribution. The obtained sideband amplitudes constitute a reduced form of the spectrograms, which serve as the input to the reconstruction algorithm.

A reliable reconstruction result requires knowledge of the probe pulse coupling constant g_ω, since it is a parameter entering the unitary operator U in the reconstruction algorithm. The value of g_ω can be obtained in multiple ways: For instance, if an experimental single-colour spectrum has been recorded for the same excitation conditions as in the two-colour spectrogram, fitting Bessel amplitudes to this single-colour spectrum yields g_ω (see also Methods section of Ref. [135]). Alternatively, the two-colour spectrogram can be fitted by Eq. 3.2, yielding values for both g_ω and $g_{2\omega}$ corresponding to the pure states which are closest to the experimental conditions. Finally, g_ω can be obtained with an optimization routine on the SQUIRRELS algorithm which minimizes the discrepancy between the experimental and reconstructed spectrogram under variation of g_ω. All approaches have resulted in very similar values for the coupling constants.

3.5.3 Description of SQUIRRELS Algorithm

Let us consider the electron density matrix reconstruction within the framework of closed quantum systems. In this case, the density operator evolves according to the time-dependent Liouville-von Neumann equation

$$\frac{\mathrm{d}\rho}{\mathrm{d}t} = -\frac{i}{\hbar}\left[H + H_{2\omega}(t) + H_\omega(t), \rho(t)\right], \tag{3.4}$$

where H is the Hamiltonian of the electron in the absence of any laser field, and $H_{2\omega}(t)$ and $H_\omega(t)$ describe its interaction with two overlapping quasi-monochromatic laser pulses, $A_{2\omega}(t)\cos(2\omega t)$ and $A_\omega(t)\cos(\omega t + \theta)$, respectively. As was shown in Refs. [28, 135], if the energy transfer during the interaction is small compared with the initial energy of the

electron, then $H_{2\omega}(t)$ and $H_{\omega}(t)$ can be regarded as commuting operators. Consequently, the unitary transformation in the interaction picture can be split into a product of two commuting unitary operators, $U_{2\omega}$ and U_{ω}, associated with each laser pulse. As a result, the quantum evolution from an initial state ρ_{in} at $t=-\infty$ to a final state ρ_{out} at $t=+\infty$ can be seen as a two-step process passing through an intermediate state. This situation may be illustrated by the diagram

$$\rho_{\text{in}} \xrightarrow{U_{2\omega}} \rho \xrightarrow{U_{\omega}(\theta)} \rho_{\text{out}}(\theta) \tag{3.5}$$

In this diagram, the first action serves as the preparation of a quantum state, with which a second, phase-controlled field interacts. The main difficulty in the determination of a quantum state stems from the lack of knowledge about the coherent (off-diagonal) part of the density matrix in quantum measurements. Here, we show how this information can be retrieved in a series of von Neumann's selective projective measurements [157], where the diagonal elements of $\rho_{\text{out}}(\theta)$ are measured at different phase delays θ between the two fields. This provides statistical information necessary for a reconstruction of the unknown off-diagonal elements of the intermediate-state's density matrix ρ.

The second step in the diagram is described, in the interaction picture, by the unitary transformation

$$\rho_{\text{out}}(\theta) = U_{\omega}(\theta)\rho U_{\omega}^{\dagger}(\theta), \quad U_{\omega}(\theta) = \mathscr{T}\exp\left(-\frac{i}{\hbar}\int_{-\infty}^{\infty} H_{\omega,\text{int}}(t)\mathrm{d}t\right), \tag{3.6}$$

where $\mathscr{T}$ is the time-ordering operator. We use the dagger notation (†) to denote the Hermitian conjugation. In the basis of eigenstates of H, $H|l\rangle = (E_0 + l\hbar\omega)|l\rangle$, $U_{\omega}(\theta)$ is given by [28, 31, 135]

$$\langle k|U_{\omega}(\theta)|l\rangle = \exp(i(k-l)\theta)J_{k-l}(2|g|), \tag{3.7}$$

where $J_{k-l}(2|g|)$ is the Bessel function of the first kind, and g is the coupling constant associated with the second laser pulse. The measurement is described by a positive operator-valued measure (POVM) with operators $\Pi_l = |l\rangle\langle l|$ such that the probability for the outcome l to occur in the experiment with a given set of phase delays $\theta \in (0,\pi)$ is given by $p_{l,\theta} = \text{tr}[\Pi_l \rho_{\text{out}}(\theta)] = \langle l|\rho_{\text{out}}(\theta)|l\rangle$. Combining this expression with Eq. 3.6,

we obtain the mapping of the unknown density matrix ρ to the experimental data

$$[T(\rho)]_{l\theta} = p_{l,\theta}, \tag{3.8}$$

where T is a linear operator defined by $[T(\rho)]_{l\theta} := \langle l|U_\omega(\theta)\rho U_\omega^\dagger(\theta)|l\rangle$. Although the Hilbert space is infinite-dimensional, in practice essentially only a finite number of states $m = 2l_{max}+1 \approx \Delta E/\hbar\omega$ is occupied, corresponding to the expected energy width ΔE of the quantum state ρ. Therefore, T is very well approximated by an operator on the finite-dimensional space $\mathscr{X}$ of Hermitian complex matrices ρ with $\rho_{kl} = 0$ if k or l are odd. The latter follows from the fact that only states $|l\rangle$ with even l can couple to $|0\rangle$ due to the second harmonic interaction. $\mathscr{X}$ is naturally equipped with the Hilbert-Schmidt inner product $\langle\rho,\tilde{\rho}\rangle = \mathrm{tr}(\rho^\dagger\tilde{\rho})$ and the corresponding norm $\|\rho\|^2 = \langle\rho,\rho\rangle = \sum_{k,l}|\rho_{kl}|^2$.

It turns out that the inverse problem 3.8 is ill-posed in the sense that T does not have a bounded inverse with respect to any natural norm, which leads to ill-conditioned finite matrices and implies that noise in the experimental data is strongly amplified by "naïve" matrix inversions. A remedy against ill-posedness is regularization. We use variational or Tikhonov regularization as one of the most well-known and commonly used regularization methods (see, e.g., Ref. [158]), since it is very flexible and in particular allows us to incorporate the a-priori knowledge that ρ is positive semidefinite as a constraint into the inversion process:

$$\rho_\alpha = \underset{\rho\in\mathscr{X}}{\mathrm{argmin}}\left[\|T(\rho)-p\|^2 + \alpha\|\rho-\rho^{(0)}\|^2\right] \text{ subject to } \mathrm{tr}(\rho)=1,\ \rho\geq 0. \tag{3.9}$$

The penalty term $\alpha\|\rho-\rho^{(0)}\|^2$ with a regularization parameter $\alpha > 0$ and some initial guess $\rho(0)$ (in our case, $\rho(0) = 0$) already restores stability, but the constraint $\rho \geq 0$ has an additional strongly stabilizing effect. Equation 3.9 can also be interpreted as a maximum posterior estimator from a Bayesian point of view where the term $\alpha\|\rho-\rho^{(0)}\|^2$ corresponds to the prior [159]. Equation 3.9 has the form of a quadratic semidefinite program (SDP) [160], the numerical solution of which will be discussed later.

Often, the approximation error can be reduced by iterating Eq. 3.9 in the form

$$\rho_\alpha^{(j+1)} = \underset{\rho\in\mathscr{X}}{\mathrm{argmin}}\left[\|T(\rho)-p\|^2 + \alpha\|\rho-\rho^{(j)}\|^2\right] \text{ subject to } \mathrm{tr}(\rho)=1,\ \rho\geq 0. \tag{3.10}$$

This is known as iterated Tikhonov regularization [158] and can also be interpreted as an

instance of the proximal point algorithm [161] for minimizing $\|T(\rho) - p_{\text{out}}\|^2$ under the constraints $\text{tr}(\rho) = 1$ and $\rho \geq 0$. We always performed three iterations of Eq. 3.10 since on simulated data we only obtained significant improvements in the first three iterations. To choose the regularization parameter α in Eq. 3.10, we use the discrepancy principle [158]

$$\alpha = \sup_{\beta \in \mathscr{A}} \beta, \quad \mathscr{A} = \{\beta : \beta > 0 \| T\left(\rho_\beta^{(3)}\right) - p\| \leq \tau\delta\}. \tag{3.11}$$

Classically, δ denotes a bound on the noise level, i.e. $\|T(\hat{\rho}) - p_{out}\| \leq \delta$ where $\hat{\rho}$ is the true (unknown) density matrix. Since such a bound is difficult to obtain in our case, we chose $\delta = \lim_{\alpha \to 0} \|T\left(\rho_\alpha^{(3)}\right) - p\|$. We point out that, in our case, $\|T\left(\rho_\alpha^{(3)}\right) - p\|$ is a monotonically increasing function of α, and thus the limit δ is always non-negative. With this definition, the signal-to-noise ratio $\|\rho_{\text{out}}\|/\delta$ takes values between 3.8 and 6.4 for our experimental data sets. With the parameter $\tau = 1.01$, the choice of α according to Eq. 3.11 yields good results for simulated data in all our experimental settings and plausible results for our experimental data.

We return to Eq. 3.9 and discuss an equivalent transformation of the quadratic SDP 3.9 into a linear SDP with a quadratic cone constraint [162], which we solve with the help of the open source optimization software SDPT3-4.0 [163]. Let $\boldsymbol{T}$ be a matrix representation of the linear operator T, and $\boldsymbol{R}^\dagger \boldsymbol{R} = \boldsymbol{T}^\dagger \boldsymbol{T} + \alpha \boldsymbol{I}$ be the Cholesky decomposition with $\boldsymbol{R} \in \mathbb{C}^{m^2 \times m^2}$. Then $\|T(\rho) - p\|^2 + \alpha\|\rho - \rho^{(0)}\|^2 = \|R(\rho)\|^2 - 2\langle \rho, T^\dagger(p) + \alpha\rho^{(0)}\rangle + C$, where R is the operator associated with the matrix $\boldsymbol{R}$, and C is a constant independent of ρ. Therefore, the problem 3.9 is equivalent to

$$\begin{aligned} \rho_\alpha &= \operatorname*{argmin}_{\rho,t,s} \left[\frac{t}{2} - \langle \rho, T^\dagger(p) + \alpha\rho^{(0)}\rangle\right] \\ &\text{subject to } t \geq \|s\|^2,\ s = R(\rho),\ \text{tr}(\rho) = 1,\ \rho \geq 0. \end{aligned} \tag{3.12}$$

The paraboloid $\{(t,s) \in \mathbb{R} \times \mathbb{C}^{m\times m} : t \geq \|s\|^2\}$ can be described as a section of the quadratic cone $\mathscr{K} := \{(u,v,s) \in \mathbb{R}^2 \times \mathbb{C}^{m\times m} : u^2 \geq \|s\|^2 + v^2\}$ by a change of variables $t = 2v - 1 = 2u + 1$. This leads to the equivalent linear semidefinite program (SDP)

$$\rho_\alpha = \operatorname*{argmin}_{\rho \in \mathscr{X}, (u,v,s) \in \mathscr{K}} \left[v - \langle \rho, T^\dagger(p) + \alpha\rho^{(0)}\rangle\right] \text{ subject to } s = R(\rho),\ \text{tr}(\rho) = 1,\ \rho \geq 0, \tag{3.13}$$

which was solved by SDPT3-4.0 using an infeasible primal-dual interior point method. Actually, this software cannot treat complex SDPs directly, but supports the conversion of complex SDPs into equivalent real SDPs with matrices of double size.

3.5.4 Performance of Reconstruction

We would like to comment on how to choose the probe strength g_ω for optimal reconstruction results. While our reconstruction method could in principle be applied for arbitrarily small probe strengths, it is advised to employ values $g_\omega = 2g_{2\omega}$, as we will discuss in the following. To test the algorithm performance, we conducted numerical experiments in which we added Poisson noise to synthetic spectrograms calculated from pure-state density matrices. The numerical experiments were repeated for six different values of $g_{2\omega}$ to exclude a dependence on the absolute pump strength. Fig. 3.7 illustrates the main findings: The reconstruction error decreases exponentially with the probe-pump ratio, until a noise level dependent minimal value is reached around $g_\omega/g_{2\omega} \approx 3.5$. This illustrates severe ill-posedness of the inverse problem 3.8 for small values of $g_\omega/g_{2\omega}$ corresponding to an exponential decay of the singular values of T. We observed numerically that the condition number of discrete representations of T increases exponentially as $g_\omega/g_{2\omega} \to 0$. If $g_\omega/g_{2\omega}$ is increased beyond 3.5, the reconstruction results slowly deteriorate. For $g_\omega/g_{2\omega} = 2$, the respective single-colour electron energy spectra have the same absolute energy width (the factor of two results from the ratio of the probe and pump photon energies). Consequently, all sidebands are being interfered with each other, and information about the corresponding coherences is directly encoded in the spectrogram. If g_ω is small, however, higher-order off-diagonals in the reconstructed density matrix are significantly underestimated, especially for highly noisy data (cf. Fig. 3.7**b**). Mixed states arising from an incoherent average of relative phases between pump and probe pulse would be described by a similar density matrix, such that pure states with noisy spectrograms and true mixed states are indistinguishable for small g_ω. Hence, the probe coupling strength g_ω should preferably be chosen about two to four times the pump coupling strength $g_{2\omega}$, and noise contributions must be kept below a tolerable level.

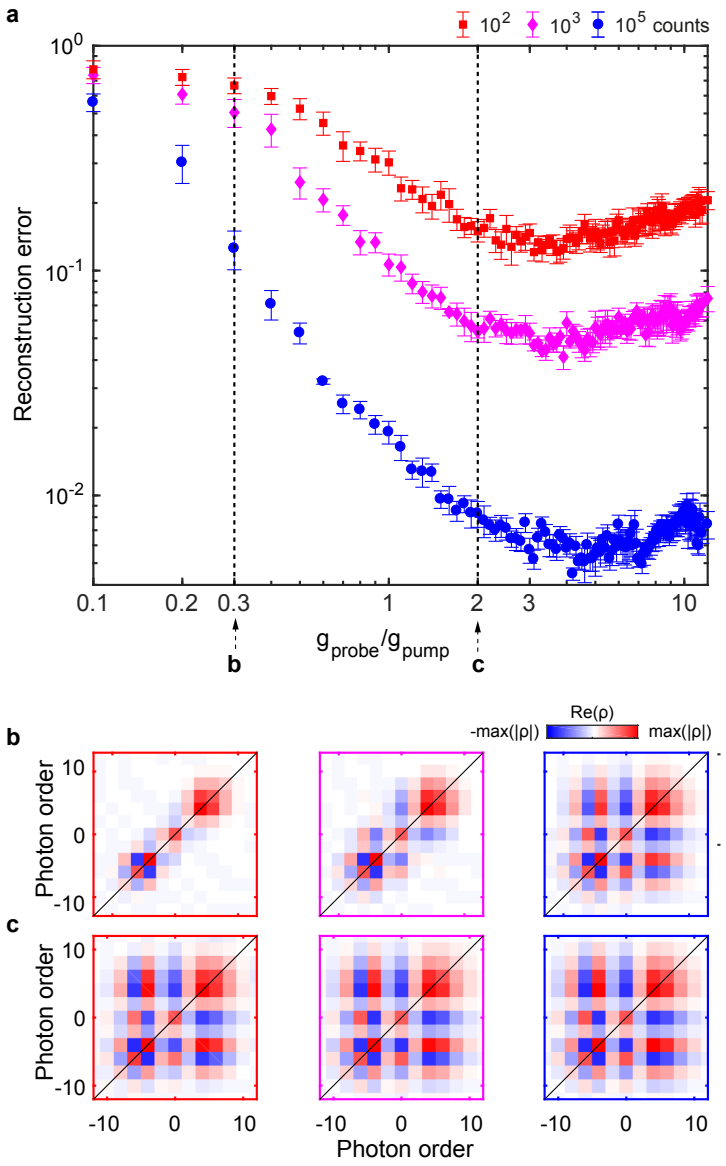

Figure 3.7: Algorithm performance for noisy synthetic data. **a** We applied the reconstruction algorithm to synthetic spectrograms with different degrees of Poisson noise, i.e., spectra for different numbers of counts per spectrum. The reconstruction error $\|\rho - \hat{\rho}\|_{\mathrm{Fro}}$ decreases with increasing ratio of the probe and pump coupling constant, until it reaches a noise-dependent minimum, followed by a slow increase of the error for even larger ratios. Best reconstruction results are obtained for probe-pump-ratios around three to four. Error bars correspond to the standard deviation of the arithmetic mean of reconstruction errors obtained for six different values of $g_{2\omega}$. **b**,**c** Reconstructed density matrices for decreasing Poisson noise (from left to right) with ratio $g_{\omega}/g_{2\omega} = 0.3$ (**b**) and 2 (**c**). The reconstruction significantly improves with smaller noise levels and larger ratios $g_{\omega}/g_{2\omega}$. Pump coupling strength $g_{2\omega} = 1.73$.

3.5.5 Application of RABBITT

In this Section, we show that a technique known as RABBITT, which stands for "reconstruction of attosecond beating by interference of two-photon transitions" and was invented to measure the relative phases of two neighbouring sidebands in high harmonic generation [154], can be adapted to our experimental scenario. To this end, we consider the case where the coupling to the ω-field is small enough to only populate the first-order sidebands $N = \pm 1$, i.e. $|g_\omega| < 0.5$. A pure quantum state prepared by the 2ω-field can be written as

$$|\psi\rangle = \sum_{N\,even} c_n |N\rangle \text{ with } c_N = e^{i\frac{N}{2}\arg(g)} J_{\frac{N}{2}}(2|g|) = |c_N| e^{i\varphi_N}, \tag{3.14}$$

where $\langle z|N\rangle = e^{ik_N z} = e^{i(k_0+\Delta k)z}$ is a plane wave with an electron momentum shifted from its initial value $\hbar k_0$ by $\Delta k = N\hbar\omega/v$. The magnitude $|c_N|$ of the sideband amplitudes is readily calculated from the measured spectrogram, while the sideband phases φ_N are not directly accessible. In the presence of the weak ω-field, the energy spectrum of the quantum state is only slightly perturbed, but odd-order sidebands are occupied (Fig. 3.8**a**). The population of these intermediate energy levels is governed by interference between the two adjacent sidebands, and is explicitly given by

$$\begin{aligned} |a_N(\theta)|^2 = J_1(2|g|)^2 [&|c_{N-1}|^2 + |c_{N+1}|^2 \\ &+ 2|c_{N-1}||c_{N+1}| \cos(2\theta + \pi + \varphi_{N+1} - \varphi_{N-1})], \quad N \text{ odd}, \end{aligned} \tag{3.15}$$

where θ is the relative phase between the two laser fields. According to Eq. 3.15, the populations of the odd-order sidebands oscillate in a cosine-fashion upon variation of θ, which is clearly visible in the experimental spectrogram (Fig. 3.8**b**). The phase offset in oscillations from different orders encodes the phase difference $\varphi_{N+1} - \varphi_{N-1}$ between two neighbouring energy levels, which can thus be obtained from a fit of cosine functions to the experimental sideband intensities. Note that in contrast to the common RABBITT scheme, here, the electrons undergo free-free instead of bound-free transitions, so that atomic phases naturally do not occur and do not have to be accounted for.

The retrieved sideband phases (red squares, Fig. 3.8**c**) are in good agreement with the values expected from Eq. 3.14 (black circles). There are, however, two drawbacks in the RABBITT-approach. The first issue concerns experimental uncertainties: The sideband

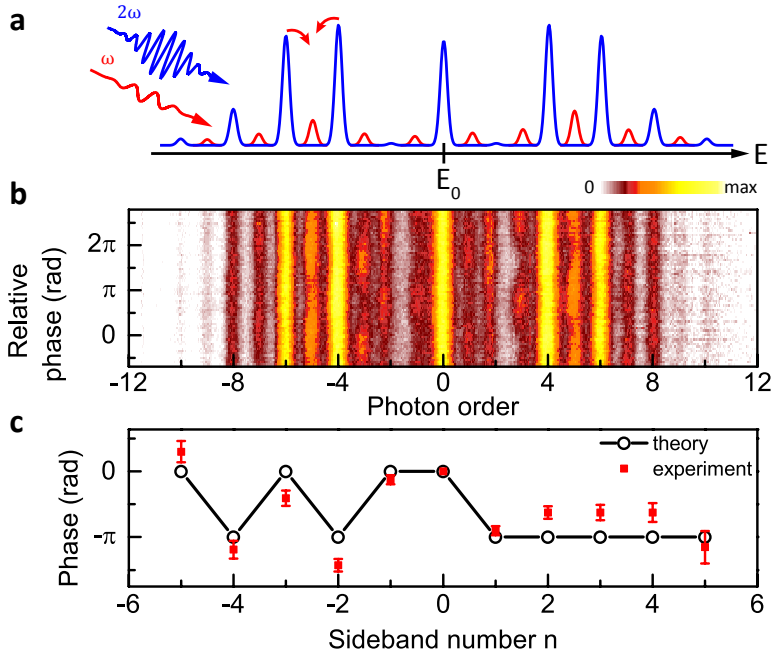

Figure 3.8: Application of RABBITT to obtain the electron quantum state. **a** Illustration of the underlying principle: A weak probe pulse ($g_\omega = 0.42$) populates intermediate energy levels (red) in the electron energy spectrum (blue) of the free-electron quantum state as prepared by coherent interaction with the 2ω pulse ($g_{2\omega} = 1.77$). **b** Experimental spectrogram obtained by varying the relative phase of the two-colour excitation. The phase-dependent populations of the odd order sidebands exhibit a cosine modulation, whose phase offset encodes the phase difference between two adjacent sidebands. **c** The phases of the sideband amplitudes (solid red squares) retrieved from the experimental spectrogram are in good agreement with the values expected from theory (open black circles). The error bars are determined by error propagation of the standard deviation of the phase differences obtained from the fit.

phases are retrieved by adding up phase differences, such that experimental errors cumulate in the higher orders. To overcome this issue, in SQUIRRELS, we employ stronger probe pulses that couple several (ideally all) sidebands to each other. Consequentially, Eq. 3.15 is no longer valid, and new algorithms such as SQUIRRELS are required to recover the sideband phases from spectrograms. The second issue concerns the scope of the RABBITT method: Equation 3.14 implies a pure quantum state, which generally may not be the case. Pure state (i.e., fully coherent) descriptions may for instance severely underestimate the retrieved pulse durations in ultrashort-pulse characterization methods using partially coherent beams, as discussed in Ref. [164]. Our SQUIRRELS method includes the possibility of mixed states, which are generally closer to experimental scenarios, and is thus more widely applicable.

Data Availability

The data that support the plots within this paper and other findings of this study are available from the corresponding author upon reasonable request.

Code availability

The code for the SQUIRRELS algorithm used to reconstruct the free-electron density matrix is available as the zip-encoded Supplementary Data file.

Acknowledgements

We gratefully acknowledge funding by the Deutsche Forschungsgemeinschaft (DFG) (Schwerpunktprogramm (SPP) 1840 'Quantum Dynamics in Tailored Intense Fields', Sonderforschungsbereich (SFB) 1073 'Atomic Scale Control of Energy Conversion', project A05 and SFB 755 'Nanoscale Photonic Imaging', project C08 and C09), support by the Lower Saxony Ministry of Science and Culture and funding of the instrumentation by the DFG and VolkswagenStiftung. We thank O. Kfir for useful discussions. T.H. would like to thank Anja Fischer (Göttingen) and Kim-Chuan Toh (Singapore) for helpful discussions on semidefinite programming.

Author Contributions

K.E.P. built the two-colour interferometer setup, conducted the two-colour experiments with contributions from A.F., analysed the data and tested the reconstruction algorithm. Ch.R. conducted the measurements of the attosecond pulse trains and analysed the data, both with contributions from K.E.P.. S.V.Y. and C.R. devised the quantum state reconstruction scheme, which was implemented by S.V.Y.. The reconstruction algorithm using regularization and semidefinite programming (SDP) was developed by T.H. with contributions from S.V.Y.. The manuscript was written by K.E.P. and C.R. with contributions from all authors. C.R. and S.S. conceived and directed the study. All authors discussed the results and the interpretation.

Additional Information

Supplementary information is available in the online version of the paper. Correspondence and requests for materials should be addressed to C.R.

3.6 Supplementary Information

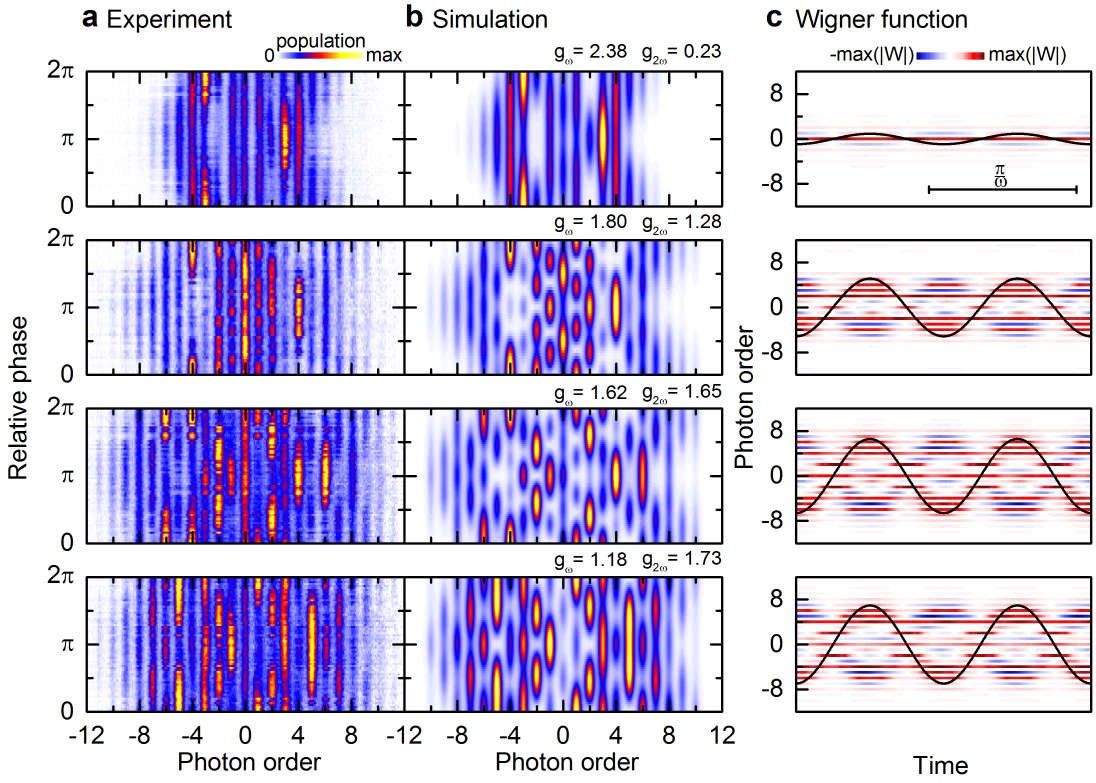

Figure 3.9: Experimental and calculated spectrograms and corresponding reconstructed Wigner functions. **a** Measured spectrograms after subtraction of the low-loss plasmon band with the full spectral resolution provided by the spectrometer. **b** Calculations employing coupling constants as given in the figure reproduce well the prominent phase-dependent spectral features, while minor differences are attributed to phase averaging effects not accounted for in Eq. 3.2. **c** Wigner function reconstructed from experimental spectrograms. The increase of the coupling constant $g_{2\omega}$ from top to bottom is reflected in a growing amplitude of the sinusoidal phase modulation. Black solid lines according to Eq. 3.1 serve as guide to the eye.

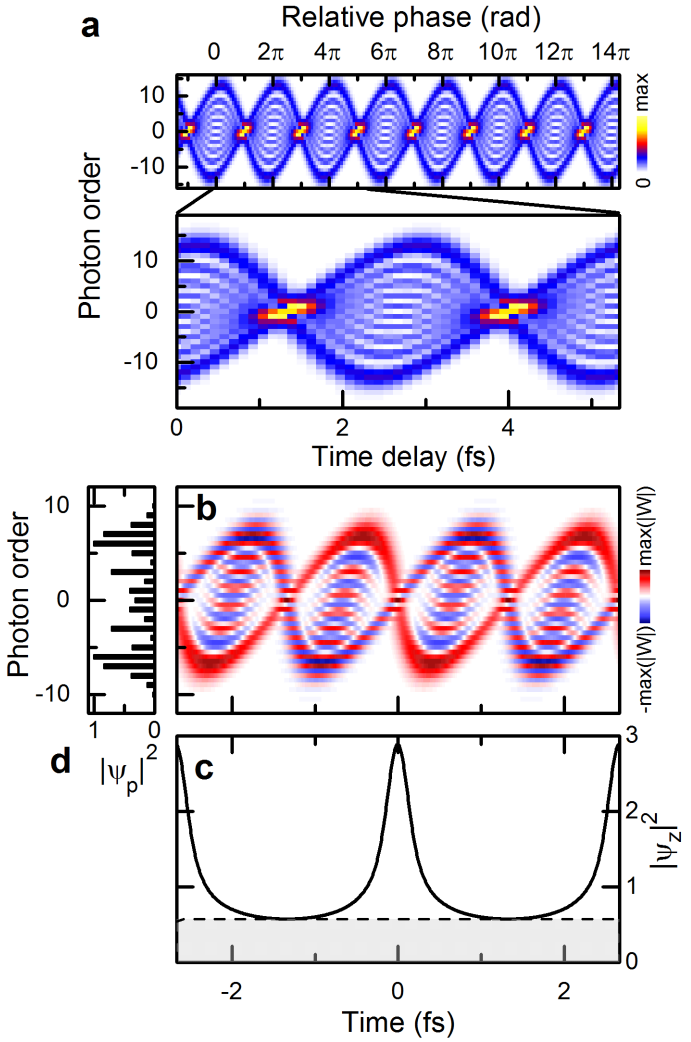

Figure 3.10: Simulation of attosecond temporal reshaping **a** Simulated spectrogram assuming a pure state with $g_{\mathrm{pump}} = 3.95$ and $g_{\mathrm{probe}} = 3.52$, including a small timing jitter of 80 as (3% of the optical period). These parameters correspond to the experimental values in Fig. 3.4. **b** Corresponding Wigner function. **c** The temporal projection of the Wigner function exhibits density modulations with a FWHM pulse duration of 531 as (after baseline subtraction, rms pulse duration: 296 as). **d** Corresponding electron energy spectrum (momentum projection).

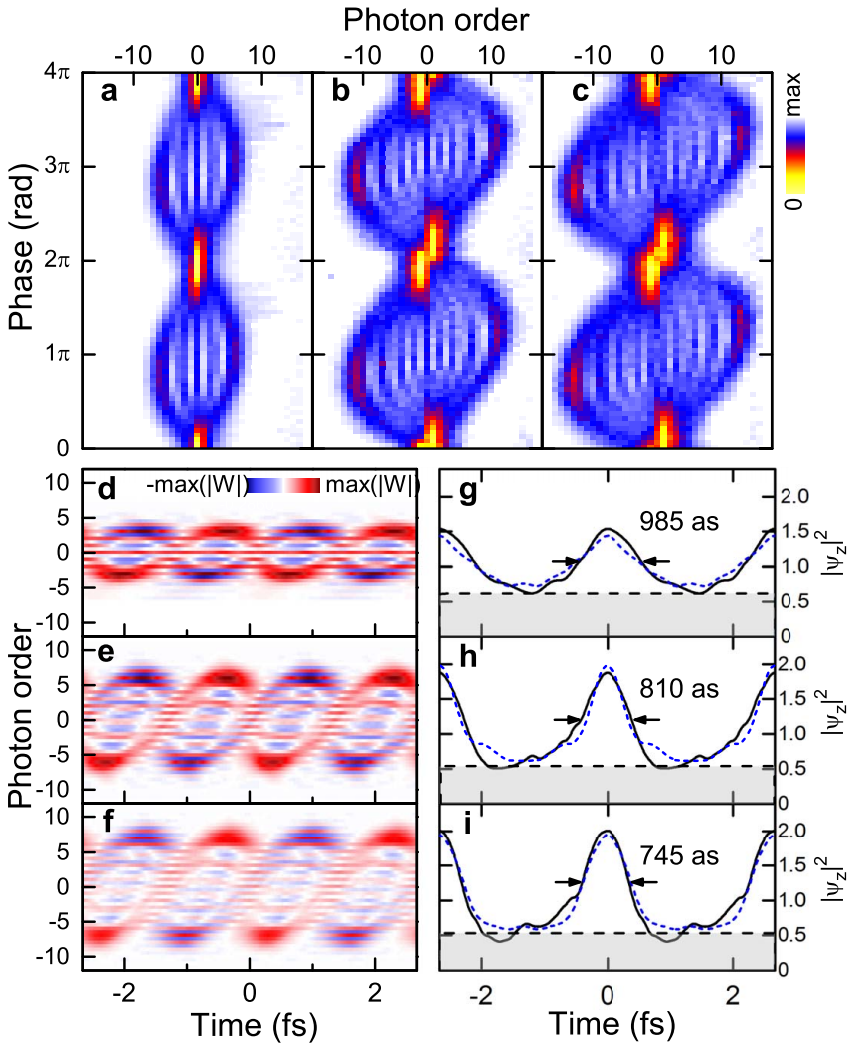

Figure 3.11: Further measurements of attosecond temporal reshaping **a**,**b**,**c** Experimental spectrograms recorded for pump and probe strengths ($g_{\mathrm{pump}} = 1.98$, $g_{\mathrm{probe}} = 1.76$), $(3.42, 3.05)$ and $(3.95, 3.52)$, from left to right. **d**,**e**,**f** Corresponding Wigner functions. Larger pump field strengths result in higher amplitudes of the sinusoidal phase modulation and shorter final attosecond pulse structures at the measurement position. **g**,**h**,**i** The temporal projection of the reconstructed Wigner function (black solid line) exhibits density modulations with a FWHM pulse duration (after baseline subtraction) as given in the Figure that decreases with increasing g_{pump}. Model calculations taking into account a timing jitter of 120 as (dashed blue line) are in good agreement with the reconstruction.

Chapter 4

Discussion

Free electrons perhaps constitute one of the most simple and fundamental quantum systems apart from photons, such that it practically suggests itself to transfer quantum optical methods from photons to free electrons. In the present work, inelastic electron-light scattering is introduced as a powerful means for the preparation, coherent manipulation and characterisation of free-electron quantum states, building on concepts from both attosecond physics and quantum optics. The underlying principle of optical phase-modulation together with the advanced capabilities of *in-situ* and sub-cycle light shaping renders all-optical control of free electrons highly versatile. Moreover, the interaction of free electrons and light does not suffer from dephasing mechanisms and thus preserves quantum coherence.

In the following, a summary of the work presented in the preceding Chapters will be given, pointing out the key results and setting them into perspective. Specifically, our approach for the reconstruction of quantum states will be discussed in a broader context, including related concepts from ultrashort pulse characterisation and coherent diffractive imaging. Potential future applications in time-resolved electron microscopy and free-electron quantum optics will be elucidated in more detail.

4.1 Summary

Chapter 2 reports the experimental implementation of a Ramsey-type electron-light interferometer based on sequential near-field interactions. Depending on the relative phase between two near-fields, the sinusoidal phase-modulation imprinted in the first interaction region can be enhanced or cancelled by the second interaction. This results from the time-

reversal symmetry of unitary operations, a fundamental property of quantum mechanical time evolution. Electron-light scattering can be interpreted as a continuous quantum random walk on an infinitely extended, equidistant energy ladder. In this picture, it becomes clear that the degree of reversibility is a measure of quantum coherence: In the incoherent limit of a classical random walk, the energy spectrum could not be recompressed to its initial width [165]. The observed near-perfect reversibility of the phase-modulation thus reconfirms the quantum coherence of the prepared free-electron quantum state, which was also demonstrated in Ref. [28] by the observation of Rabi-oscillations.

Going beyond the elementary case of sinusoidal phase modulations, two-colour near-fields are employed in Chapter 3. Although the light shaping capabilities of our setup fall short of spatial light modulators, merely changing the relative phase and intensities of two laser beams at commensurate frequencies proved to be a powerful approach for free-electron coherent control. Two-colour interactions actually present more than a first step towards more complex phase modulations: Quantum state tomography for free electrons based on phase-controlled multi-field interactions was successfully demonstrated. This is a particularly important application, since state characterisation is a cornerstone technique for (free-electron) quantum optics. In Spectral QUantum Interference for the Regularised Reconstruction of free-ELectron States (SQUIRRELS), the density matrix is reconstructed in the longitudinal momentum basis from experimental spectrograms.

SQUIRRELS is not limited to the combination of fundamental and second harmonic pulses. Essentially any pulse pair at commensurate frequencies, including pulses at the same frequency, can be employed. To avoid phase-ambiguities in the reconstructed state in the case of differing frequency, the smaller frequency pulse must be used as the probe. Moreover, reconstruction is possible irrespective of whether the interactions take place at the same or spatially separated positions. Consequently, SQUIRRELS is ideally suited for the quantitative characterisation of attosecond electron pulse trains, that occur after time-periodic phase modulations due to dispersive free-space propagation and thus require a means for probing at a position distant from the preparation region. The temporal envelope of the electron pulse is obtained from the marginal distribution of the reconstructed Wigner function, and in a first experiment, trains of sub-fs pulses were measured.

4.2 Quantum State Reconstruction

The possibility to determine the quantum state of free-electrons presents a key result of this work. In the following, possible sources of decoherence that reduce the purity of the free-electron quantum states will be discussed, before SQUIRRELS will be compared to other characterisation techniques from ultrafast optics and attosecond science.

4.2.1 Purity of the Quantum States

Since the IELS interaction as described by Eq. 1.3 corresponds to a unitary transformation under which purity is conserved, free-electron quantum states with purity close to one are expected, given that the incident state can be described by the pure state $|\psi\rangle = |0\rangle$ in the photon-sideband basis $\{|N\rangle\}$. The purities observed in Chapter 3, though, range between $P = 0.10$ and 0.30 for the attosecond pulse train data and between $P = 0.20$ and 0.55 for the two-colour measurements.[1] Higher purities should be achievable in the experiments by avoiding the main effects leading to their reduction, which will be elucidated in the following.

Possible sources of mixedness can be categorised in

(i) incoherent ensemble averages in the preparation of the initial quantum state (i.e., probabilistic shot-to-shot variations in the photoemission process),

(ii) non-ideal interactions during the time evolution that are not describable by a single unitary transformation and

(iii) variations of the electron wavefunction in degrees of freedom that are not resolved in the measurement and therefore traced out in the description.

As stated in Sec. 1.2.1, any quantum state that can be written as a wavefunction is in a pure state. Effects (i)-(iii), though, require the state to be written as an incoherent sum over multiple wavefunctions that describe differing initial wavefunctions (i) and unequal phase-modulations stemming from pulse-to-pulse variations in the light field (ii) or from spatially varying field strengths (iii). Figure 4.1 illustrates some examples, which will be explained in more detail in this Section.

[1] These values should be set in relation to the minimum possible purity, which is $1/d$ for $d \times d$-dimensional density matrices. With $d \approx 4|g| + 1$, the minimum purity lies in the range of 0.05 to 0.11 for typical coupling constants $2 \lesssim g \lesssim 4$.

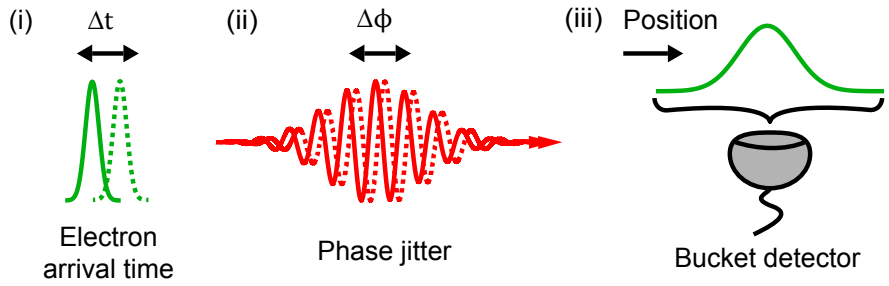

Figure 4.1: Possible sources of mixedness corresponding to the three cases mentioned in the text. Note that cases (i) and (ii) have different effects on the state as the absolute time frame is fixed by the probe pulse (not shown).

The electron-light coupling constant g is generally position- and time-dependent, but in the measurement, the energy spectra are spatially integrated over the electron beam area and temporally integrated for a few seconds. In particular, the coupling constant may vary in phase due to temporal jitter between the optical pump and probe beams (category (ii)), and both in magnitude and phase due to spatially inhomogeneous near-fields across the interaction area (category (iii)). Spatial averaging is especially significant for nanostructures with small radii of curvature, such as the sample employed in Chap. 2. The high spatial coherence of the electron source, however, permits to focus the electron beam down to nanometre spot sizes, and allows us to invoke nearly constant coupling strengths. For the planar graphite flake used in Chap. 3, spatial averaging is inherently negligible. Temporal jitter is absent in the dual near-field structure in Chap. 2, since the relative phase is controlled via the polarisation of a single incident laser pulse. In the two-colour interferometer in Chap. 3, which was not actively stabilised, temporal jitter is, however, the main source of decoherence.

The purity of the free-electron quantum states is in fact most severely affected by temporal jitter. Already small phase uncertainties (standard deviation 5% of the optical period) reduce the purity below 0.5 for typical coupling constants. As illustrated in Fig. 4.2, the outermost off-diagonal elements of the density matrix are most sensitive to phase jitter and vanish first, given that they correspond to the coherences between the most distant sidebands that oscillate at the highest frequencies (proportional to the difference in sideband number). For this reason, purity is lost more easily for stronger couplings that lead to the population of higher sidebands. Ultimately, if the phase jitter is large enough, only the main diagonal elements of the density matrix remain, and any light-phase dependent features in the Wigner function vanish.

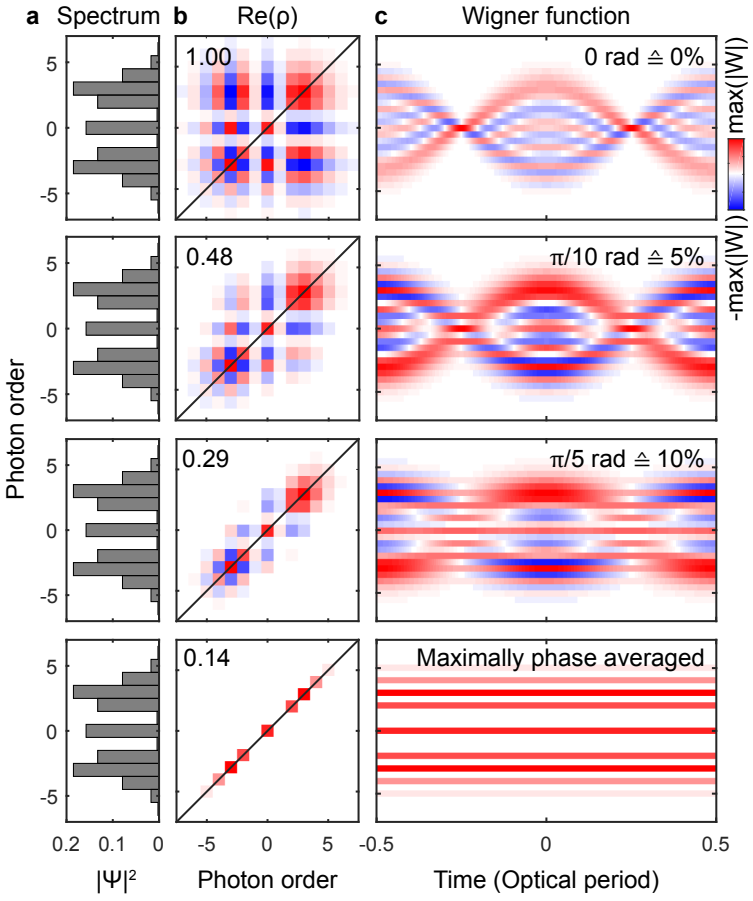

Figure 4.2: Effect of phase averaging on the quantum state's purity. **a** The spectrum remains unchanged. **b** With growing phase jitter (from top to bottom), the outermost coherence terms are increasingly suppressed, and the purity $\mathrm{tr}(\rho^2)$ (number in upper left corner) decreases. **c** In the Wigner function, the phase jitter corresponds to a convolution with a Gaussian along the time axis. Eventually, all time dependencies are averaged out. Numbers in the upper right corner: Standard deviation of phase relative to one optical period. Calculations for $g = 2$.

Another form of incoherent temporal averaging stems from the mixedness of the initial electron ensemble (category (i)) and is revealed if the laser pulse duration is comparable to or shorter than the electron pulse duration.[2] Consider a long electron pulse that consists of an incoherent ensemble of temporally shifted, but otherwise identical electron wavepackets. Because the laser pulse significantly changes its field strength over the electron pulse duration, the individual electrons within the ensemble experience different coupling strengths g depending on their temporal shift. Consequently, the final quantum state is given by an incoherent average over these coupling strengths. This effect most likely contributed to the reduced purity in the two-colour experiments, in which the 2ω-pulse was only moderately longer than the electron pulse (cf. Fig. 3.6). It were absent if

[2]Note that the purity is, in this case, reduced due to the incident electron state and not due to the electron-light interaction. The mixedness of the initial state can, however, not be captured by the density matrix in a momentum basis representation with an energy spacing that exceeds the initial electron energy width. A finer-resolved momentum basis will be considered in Sec. 4.3.4.

the incident electron pulse were in a pure state or if the laser pulse can be approximated as a continuous wave.

Besides temporal and spatial averaging, the limited energy resolution of the EEL spectrometer may generally contribute to decoherence. In the present experiment, the different sidebands are non-overlapping, given that the 0.4 eV energy resolution of our spectrometer is sufficient to resolve the photon sidebands that are separated by $\hbar\omega = 1.55\,\mathrm{eV}$. Also, the initial electron energy width is much smaller than the photon energy. Therefore, the energy resolution does not influence the purity.

In addition to the various physical averaging effects discussed above, also the data quality, the choice of measurement parameters (in particular the probe coupling strength g and the number and distribution of relative phases) and assumptions on the probe pulse affect the purity of the reconstruction result. For instance, noise in the experimental data reduces the purity. Furthermore, the coupling constant g must be large enough to directly interfere each sideband with all the others to reliably reconstruct all coherence terms from noisy spectrograms, as demonstrated in Fig. 3.7. In other words, g must correspond to at least half the number of populated sidebands in the state that is to be reconstructed. In particular, a RABBITT trace (see Sec. 4.2.2), in which only neighbouring sidebands are coupled to each other, does not contain sufficient information for a reliable reconstruction of the coherences [164].

The SQUIRRELS algorithm incorporates a unitary operator that describes the probe pulse as a continuous wave. Besides the fact that this approximation is only valid if the probe pulse is a few times longer than the electron pulse, this leads to errors if the algorithm is applied to extended spectrograms, in which the probe pulse is scanned across the entire electron pulse. Therefore, SQUIRRELS will have to be modified for a correct characterisation of the complete electron pulse. Note that a non-cw probe pulse has a different effect on the purity compared to the pulse used for state preparation, which was discussed above. While incoherent averaging due to non-cw excitation in the state preparation merely reduces the purity of the quantum state, a non-cw probe field is not adequately described by the unitary operator used in the current version of the algorithm. To avoid consequential errors in the reconstruction, the operator has to be adapted to the physical situation.

To summarise, the main physical source of decoherence in the current experimental setup is phase jitter, which should be suppressed in future experiments by actively stabilising the interferometer. In order to reliably retrieve also the highest-order coherences,

large probe field strengths that allow for direct coupling of the outermost sidebands should be employed. Furthermore, a new version of SQUIRRELS should be developed that is applicable to time-dependent probe-fields and uses a continuous momentum basis. Section. 4.3.4 outlines a possible route towards such a new version.

4.2.2 Comparison with RABBITT

In this Section, SQUIRRELS, which essentially recovers missing phase information from intensity measurements, will be compared to *RABBITT* (Reconstruction of Attosecond Beating By Interference of Two-photon Transitions), a phase-retrieval method which is used to characterise attosecond pulse trains produced by high harmonic generation [154].

Phase retrieval is generally required when complex quantities are dealt with and knowledge of both amplitude and phase is important, but only phase-less intensities can be measured. In addition to quantum optics, this inverse problem, which is also known as the *phase problem*, occurs in a number of different areas of engineering and physics, and a correspondingly great variety of solutions has been developed. Examples can be found in imaging, signal processing or ultrashort-pulse characterisation and range from large scale applications in astronomy [166], to nanoscale applications in x-ray crystallography [167], electron microscopy [168] and coherent diffractive imaging (CDI) [169, 170]. In ultrafast optics and attosecond science, frequency-resolved optical gating (FROG) [153], spectral phase interferometry for direct electric-field reconstruction (SPIDER) [171] and RABBITT are now established pulse characterisation techniques. However, in contrast to algorithms from quantum optics and coherent diffractive imaging, FROG, SPIDER and RABBITT do not take into account partial coherence.

In Section 3.5.5, we demonstrated that the RABBITT algorithm can in principle be applied to spectrograms if the quantum state is prepared by the second harmonic field and probed by the corresponding fundamental, and if the coupling strength of the probe field is chosen small enough to couple only neighbouring sidebands. In comparison to SQUIRRELS, much weaker probe pulses are sufficient (and even required) for RABBITT, and the reconstruction is straightforward. Despite these advantages, RABBITT is in general not the better choice, given that it can only yield a rough estimate of the quantum state if its purity significantly differs from one. For illustration, a state that is mixed due to temporal jitter will be considered.

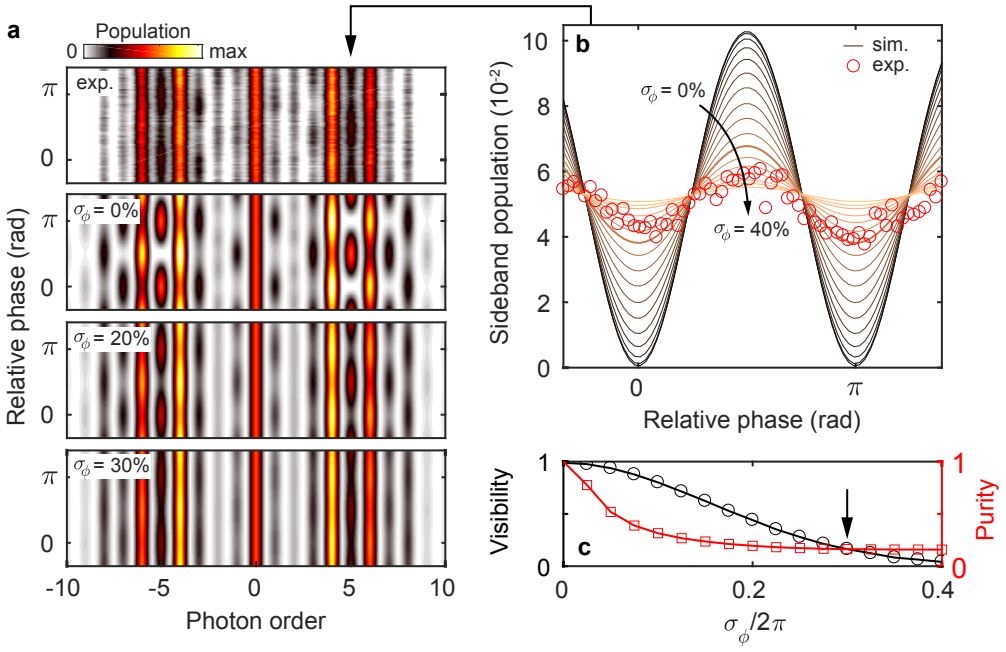

Figure 4.3: Influence of phase jitter on RABBITT traces. **a** Experimental trace and calculations for increasing phase jitter (top to bottom). **b** Phase-dependent population of the $N = 5$ sideband (marked by black arrow in **a**). The experimental curve has a low interference visibility of only 16%. **c** For increasing phase jitter σ_ϕ, both purity and interference visibility decrease. The experimental data are well described by 30% phase jitter (standard deviation relative to optical period, black arrow). Calculations for $g_\omega = 0.42$, $g_{2\omega} = 1.77$.

Temporal jitter essentially corresponds to a convolution of an ideal spectrogram with a Gaussian distribution along the phase axis and thus reduces the interference contrast in the spectrogram, as illustrated in Fig. 4.3. A fit to model calculations reveals that in the experimental RABBITT trace, temporal jitter amounts to approximately 30% (standard deviation relative to the optical period), reducing the quantum state's purity to $\mathrm{tr}(\rho^2) = 0.16$. The RABBITT algorithm yet assumes pure states and only takes into account the phases of the sideband oscillations (which in the case of phase jitter actually remain unchanged!). Thus, if temporal jitter is the sole source of decoherence, the reconstruction yields the underlying pure state that would have been observed in the absence of jitter[3]. If mixedness is ignored in the characterisation of XUV pulse trains, and likewise of attosecond electron pulses, the retrieved pulse durations significantly underestimate the factual one [164]. In conclusion, RABBITT should only be applied for high interference visibility, which indicates a high purity of the quantum state.

[3]Note that this coincidence does not occur if the mixedness arises from amplitude variations of g. Furthermore, the RABBITT-reconstructed pure state would, in that case, not be describable by Eq. 1.3.

4.2.3 Alternative Approaches for Quantum State Reconstruction

Continuing the discussion from Sec. 4.2.2, in this Section, SQUIRRELS will be compared to further phase retrieval methods. In particular, an alternative reconstruction method based on generalised projections will be elaborated on in more detail, followed by possible directions for future algorithmic developments.

The central goal of any phase retrieval algorithm is of course the unique and robust reconstruction of the missing phase information, which is usually inferred from either additional prior information, e.g. the spatial support of a sample in CDI, or additional intensity measurements such as in SQUIRRELS. Phase-retrieval algorithms can be roughly categorised in *iterative* and *analytic* solutions. SQUIRRELS belongs to the second kind of algorithms, which are usually faster, but require prior knowledge or assumptions, which might not be exactly fulfilled and thus potentially limit the accuracy. In SQUIRRELS, for instance, the probe pulse is assumed to be an ideal phase modulator with spatially and temporally homogeneous interaction strengths, which in the present experiments is fulfilled quite well. Iterative algorithms, on the other hand, often cannot guarantee convergence, struggle with local minima and imply lengthy computations. Some algorithms therefore combine both approaches and use results from analytic algorithms as initial values for iterative methods.

One of the most widely used iterative phase-retrieval algorithms is the principal component generalised projection algorithm (PCGPA) [172] known from FROG, and the non-iterative SQUIRRELS algorithm should be benchmarked against it. In FROG, the spectral phase of an ultrashort optical pulse is reconstructed from a so-called FROG trace $S(\omega, \delta t)$, that is, a spectrally resolved autocorrelation. The pulse $P(t)$ to be reconstructed is overlapped in a nonlinear medium with a gate $G(t)$. In the most common form of FROG employing second harmonic generation (SHG), the gate is given by the time-delayed replica $G(t) = F(t - \delta t)$ of the pulse $P(t) = F(t)$ to be reconstructed. Note that the algorithm works also if $G(t)$ and $P(t)$ are totally different functions, as in our case. Spectrally resolved measurements for various time delays yield the spectrogram

$$S(\omega, \delta t) = \left| \int_{-\infty}^{\infty} \mathrm{d}t \; G(t - \delta t) \cdot P(t) \cdot e^{i\omega t} \right|^2 . \tag{4.1}$$

The one-dimensional dataset obtained by an intensity autocorrelation does not have a unique solution. In FROG, in contrast, both gate and pulse can be reconstructed in ampli-

tude and phase from these two-dimensional datasets, even without knowledge of G (this is referred to as "blind FROG"). Equation 4.1 is mathematically equivalent to a SQUIRRELS spectrogram $I(k,\Delta\varphi)$ for a pure electron quantum state:

$$\begin{aligned} I(k,\Delta\varphi) &= \left| \int_{-\infty}^{\infty} \mathrm{d}z\, G(z-\Delta z)\cdot P(z)\cdot e^{ikz} \right|^2 \\ \text{with}\;\; G(z) &= \exp\left(2i|g_1|\sin\left(\frac{\omega_1 z}{v}\right)\right), \\ P(z) &= \exp\left(2i|g_2|\sin\left(\frac{\omega_2 z}{v}\right)\right)\cdot\psi_{\mathrm{in}}(z) \;\text{ and }\; \Delta\varphi = \frac{\omega_1}{v}\Delta z. \end{aligned} \tag{4.2}$$

Because the algorithm is independent of the physical process generating the spectrogram, it can equally be applied to Eq. 4.2 to reconstruct the phase-modulated free-electron wavefunction.

Details on the PCGPA can be found in Ref. [172]. The working principle is sketched in Fig. 4.4**a** and will be outlined in the following. Two constraints have to be fulfilled: In Fourier space, the spectrogram intensities equal the measured intensity. In real space, the signal corresponds to the outer product of gate and pulse. Further constraints can improve convergence, e.g., in our case, both gate and pulse are assumed to be pure phase functions $e^{i\varphi}$ that are periodic within an optical laser cycle. Starting with an initial guess for G and P, the algorithm iteratively applies the respective projections in real and Fourier space. In the latter, the intensities are replaced by the measured ones. In real-space, the *principal component*, i.e., the outer product pair corresponding to the largest eigenvalue, which gives the algorithm its name, is determined as follows: The outer product form of pulse and gate in their vector representations $P=[P_1,P_1,\dots P_N]$ and $G=[G_1,G_1,\dots G_N]$ is given by

$$O(t,t') = \begin{bmatrix} P_1G_1 & P_1G_2 & \dots & P_1G_N \\ P_2G_1 & P_2G_2 & \dots & P_2G_N \\ \vdots & \vdots & \ddots & \vdots \\ P_NG_1 & P_NG_2 & \dots & P_NG_N \end{bmatrix}. \tag{4.3}$$

Rotation of all row elements to the left by the row number -1 reveals a one-to-one correspondence between the spectrogram (with shifted column order) and the outer product form:

$$O(t-\tau) = \begin{array}{c} \begin{matrix} \tau{=}0 & \tau{=}\Delta t & \dots & \tau{=}-\Delta t \end{matrix} \\ \begin{bmatrix} P_1G_1 & P_1G_2 & \dots & P_1G_N \\ P_2G_2 & P_2G_3 & \dots & P_2G_1 \\ \vdots & \vdots & \ddots & \vdots \\ P_NG_N & P_NG_1 & \dots & P_NG_{N-1} \end{bmatrix} \end{array}. \tag{4.4}$$

Therefore, one can reversibly switch between the two by row rotation. Ideally, the product form $O(t,t')$ would be a rank one matrix, i.e., it would only have one non-zero eigenvalue and correspond exactly to the outer product of two vectors. In practice, this matrix will, however, have several eigenvalues. To retrieve P and G from the spectrogram $O(t-\tau)$, the outer product form $O(t,t')$ is obtained by inverse row rotation. Then, the principal component, which is the closest approximation to the true solution, is determined with the power method [172, 173]. The algorithm is terminated when the error defined as the discrepancy between the measured and reconstructed spectrogram falls below a certain threshold. The PCGPA is particularly fast, as it does not require minimisation steps and guarantees reduction of the error in every iteration.

Figure 4.4 exemplifies the algorithm's performance using the experimental dataset shown in Fig. 3.1. As in SQUIRRELS, phase ambiguities are avoided by using the ω-pulse as the gate, which was kept fixed as $\exp\left(2i|g_\omega|\sin\left(\frac{\omega_z}{v}\right)\right)$. The coupling strength $g_\omega = 1.18$ was separately determined from the single-colour spectrum in Fig. 3.1**c**. A phase function with randomly distributed phases from $-\pi$ to π was chosen as the initial guess for the pulse. The retrieved phase modulation shown in Fig. 4.4**d** (black squares) recovers the expected phase $2|g_{2\omega}|\sin\left(\frac{2\omega_z}{v}+\varphi\right)$ (blue line) with deviations around the extrema of the sine-function, which can mainly be attributed to incoherent averaging effects.

The PCGPA as presented here works reasonably well, but in order to compete with SQUIRRELS, some issues still have to be worked on. For instance, in SQUIRRELS the number of data points along the phase and energy axes are independent of each other, and the phases can be chosen randomly, whereas the PCGPA is less flexible and requires square-matrix spectrograms and equidistant phases with periodic boundary conditions. Therefore, the sidebands had to be padded with zeros and parts of the spectrogram were concatenated to span a full optical cycle. But most importantly, in its present form,

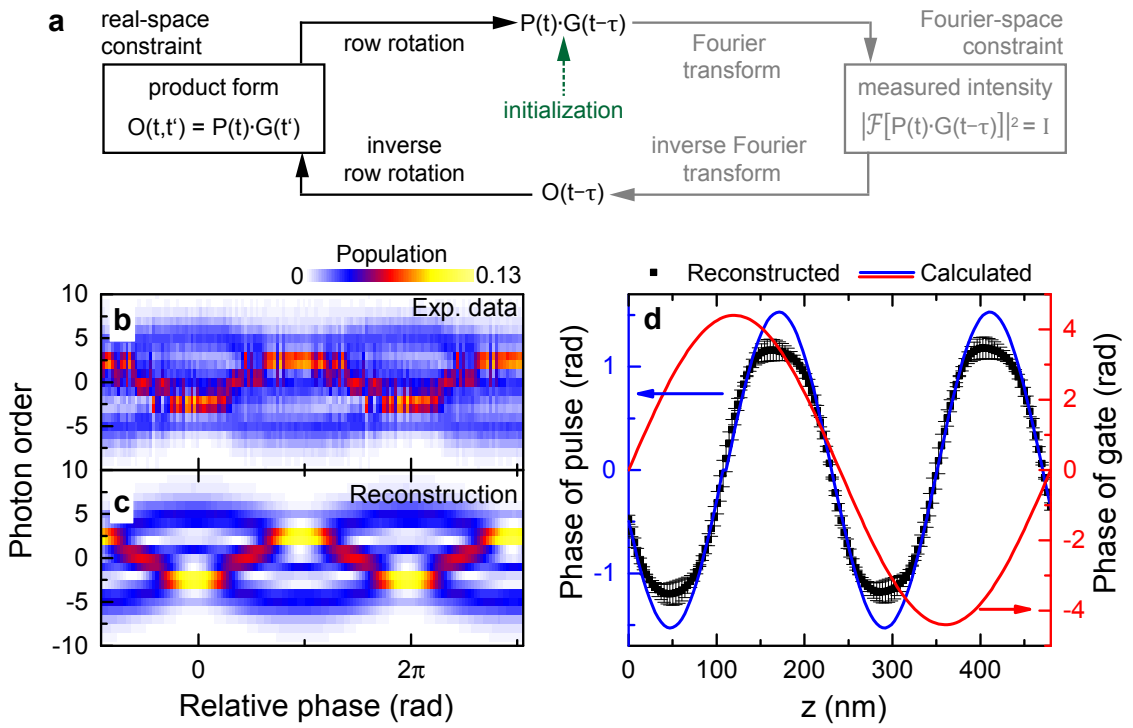

Figure 4.4: Quantum state reconstruction based on PCGPA. **a** Algorithmic scheme. **b** Experimental spectrogram. **c** Reconstruction using the PCGPA (250 iterations, result averaged over all runs with error $\varepsilon < 9 \cdot 10^{-3}$). **d** Theoretically expected phases of pulse (blue line) and gate (red line) and corresponding reconstruction from experimental spectrogram (black squares).

PCGPA, just like RABBITT, cannot account for mixed quantum states, as Eq. 4.2 inherently assumes pure states.

SQUIRRELS certainly is not the only way to retrieve mixed states and it might be worthwhile to consider other approaches. Recently, an extension of PCGPA to mixed states has been demonstrated for partially coherent attosecond XUV pulses[164]. Another promising approach is to transfer concepts from ptychography [174, 175] to ultrafast pulse characterisation [176] in a mixed state version [177], which outperforms PCGPA in terms of data requirements: In ptychography, as in SQUIRRELS, the number of spectra in the spectrogram can be chosen independent of the energy sampling. In particular, it was demonstrated that only very few spectra are needed for a robust reconstruction [176]. Because ptychographic approaches feature the possibility of blind reconstruction, that is, retrieval of both gate and pulse without *a priori* knowledge of the gate, future work in this direction may improve free-electron quantum state tomography, possibly outperforming SQUIRRELS, which in its current form is limited to quasi-continuous wave probe fields.

4.3 Outlook

The following Sections will give an outlook on how quantum interference in IELS could possibly be harnessed in various areas of research, in particular time-resolved electron microscopy and quantum information.

4.3.1 Programmable 3D Phase-Shaping of Free Electrons and 3D Quantum State Reconstruction

Programmable pulse shapers are nowadays able to produce virtually any desired optical waveform [5, 178], and a similar degree of controllability is desirable for free electrons to further extend the functionality of electron microscopes [179]. It has for instance been suggested to utilise the ponderomotive potential of intense light fields to create a Zernike phase-plate for phase-contrast imaging of biological samples in TEM [180, 181] and to transfer orbital angular momentum from photons to free-electrons for all-optical generation of electron vortex beams [88]. The possibility of in-situ and sub-cycle shaping of laser light renders all-optical control techniques highly versatile.

Coherent electron-light scattering opens a new route towards three-dimensional phase-shaping of free electrons. For the purpose of this work, in which optical phase-modulation is used as a programmable, temporal phase-plate for free electrons, it is sufficient to treat the electron in one dimension and to neglect transverse degrees of freedom. In general, absorption and emission of photons does not only result in a longitudinal momentum kick, but also sideways, as illustrated in Fig. 4.5**a**. If the electron wavefunction coherently extends laterally to several optical wavelengths, transverse momentum sidebands appear. Therefore, optical phase-modulation may be utilised to control both the longitudinal and transverse components of the electron wavefunction. Due to the large initial momentum $k_0 \approx 1.9\,\mathrm{pm}^{-1}$, the photon-induced electron deflection is on the order of µrad, two orders of magnitude smaller than typical beam divergences. Analogously to the longitudinal phase modulation, the transverse momentum sidebands lead to a spatial focusing at a certain propagation distance. As in the longitudinal variant, the amplitude and phase of the transverse phase modulation can be tailored, for example by using nanostructures with spatially dependent field enhancements, by interfering multiple waves, e.g. two counter-propagating waves [130] or by shaping the transverse laser beam profile.

Because the transverse phase modulation is largely analogous to the longitudinal one,

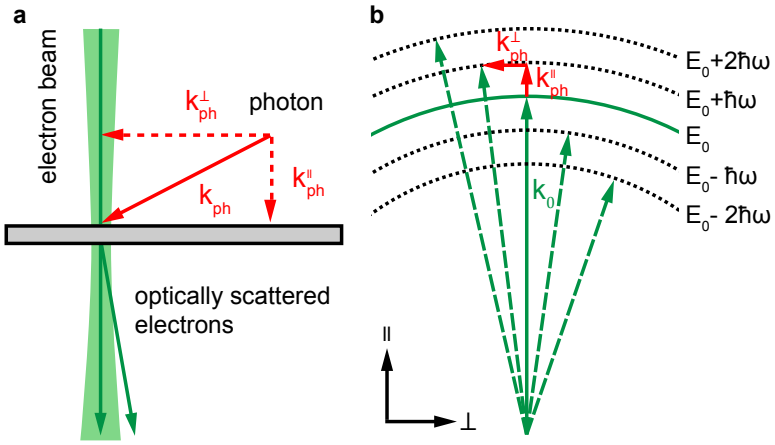

Figure 4.5: Three dimensional picture of coherent electron light scattering. **a** Experimental scenario. The incident photons transfer momentum to the electrons both parallel and perpendicular to the initial electron momentum $\hbar k_0$. **b** In momentum space, the photon sidebands correspond to circles of constant total momentum. Green arrows: Electron momenta. Red arrows: Momentum change due to photon absorption or emission. Sketch not to scale, $k_{ph}/k_0 \approx 10^{-6}$.

SQUIRRELS should be adaptable to the reconstruction of the transverse free-electron quantum state in momentum representation. "Transverse SQUIRRELS" could for instance be realised by recording electron diffraction patterns instead of energy spectra after interaction with two-colour optical near-fields for various relative phases between the two colours. To cover both transverse directions, either the electron beam or the optical excitation would have to be rotated around the electron beam axis, ideally by 90°. The three-dimensional quantum state could be obtained by combining both momentum- and energy-resolved measurements.

It should be pointed out that the idea of "Transverse SQUIRRELS" is related to a recent proposal by Lubk *et al.* to employ off-axis electron holography for reconstructing the transverse position-space representation of the electron density operator [182, 183]. In holography, information on the electron spatial coherences is gained by interfering two partial waves $\psi(\vec{x}-\vec{d}/2)$ and $\psi(\vec{x}+\vec{d}/2)$ that are split and spatially displaced by $\vec{d}$ using a Möllenstedt biprism [184]. The proposal by Lubk *et al.* would extend conventional holography, which can essentially be viewed as quantum state reconstruction constricted to pure states, to include partially coherent states, just as SQUIRRELS extends RABBITT. To reconstruct the density matrix, a set of interference patterns would be recorded for varying displacements $\vec{d}$ and for two different biprism orientations. Besides investigating incoherent processes like inelastic scattering, a reconstruction of the transverse quantum

state allows for characterising the electron beam itself, including aberrations introduced in the TEM column, opening the possibility of *a posteriori* aberration correction.

4.3.2 Attosecond Electron Microscopy

Attosecond electron microscopy promises time-resolved studies of sample dynamics with nanometre spatial and attosecond temporal resolution, but it has not been demonstrated yet due to the lack of attosecond electron pulses. In accelerator science, a large variety of schemes for attosecond bunching have been devised, since bunched multi-electron beams can be harnessed for the generation of coherent hard x-ray pulses. Examples range from laser-plasma interactions, such as wakefield accelerators [185] and overdense plasmas [186], over inverse free-electron laser interactions [156] to ponderomotive scattering [187]. These schemes work in the MeV regime, though, and such energetic electrons resulting in small scattering cross section and diffraction angles are not convenient for electron microscopy. As shown in this thesis, IELS allows to temporally shape free-electron beams at keV energies on a sub-cycle time scale. Attosecond electron microscopy, perhaps one of the most exciting applications of IELS, should therefore now be feasible, if the following conditions are fulfilled:

1. Free-space isolated electron pulses or electron pulse trains can be generated such that they have attosecond duration at the sample position.

2. Electron pulse compression is robust under realistic experimental conditions.

3. The electron pulse or pulse train is synchronised to the sample excitation with attosecond precision. Synchronisation must furthermore be achieved over the entire sample area that is illuminated by the electron beam in order not to corrupt the attosecond temporal resolution.

4. The ultrashort process under study yields a measurable signature in the electron diffraction pattern, real space image, or energy spectrum.

In the next Section, the pulse compression scheme developed in this work will be contrasted to a related proposal by Baum and Zewail from 2007 [148] that is likewise suitable for keV electron energies, followed by an examination of our scheme with respect to the above-mentioned requirements.

Generation of Attosecond Electron Pulses by a Moving Intensity Grating

The idea of Baum and Zewail is based on the Kapitza-Dirac effect [25], in which an electron is diffracted from the ponderomotive potential of a standing light wave that is oriented perpendicular to the electron beam axis. Absorption of a photon from one of the two light fields and stimulated emission of a photon into the other field leads to a $2\hbar k$ momentum change of the electron. Note that the Kapitza-Dirac effect is based on the $\vec{A}^2$-term in the Hamiltonian, whereas inelastic light-scattering relates to the much larger $\vec{A} \cdot \vec{p}$-term, which does, however, not contribute in this case due to the energy-momentum mismatch.

If two counter-propagating light fields at different frequencies ω_1 and ω_2 are employed, a moving intensity grating is produced. For a suitable choice of ω_1 and ω_2 and a propagation direction parallel to the electron beam, this moving intensity grating corresponds to a longitudinal standing wave in the electron rest frame. Because the ponderomotive potential is co-moving with the electron pulse during the entire interaction time, parts of the electron pulse positioned at a rising slope of the potential experience a net acceleration and those at falling slope a net deceleration. Further free-space propagation after the interaction leads to a self-compression of the electron pulse.

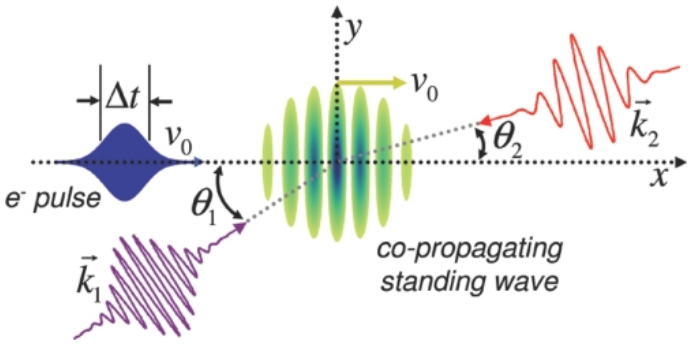

Figure 4.6: Scheme for the generation of attosecond electron pulse trains by a moving intensity grating. The laser pulses travel at angles $\theta_{1,2}$ with respect to the electron beam to achieve energy-momentum conservation. Reprinted with permission from Ref. [149].

Figure 4.6 displays a generalisation of this proposal by Hilbert *et al.* [149], which has recently been realised experimentally by Kozak *et al.* [188]. In contrast to the original proposal, in which energy-momentum conservation can only be obtained for certain electron energies, in the generalised version this is achieved for any given parameter set of electron energy and laser wavelengths by using laser fields with non-zero incident angles θ_1 and θ_2 with respect to the electron beam axis.

In comparison to the approach discussed in this thesis, this alternative method for the generation of attosecond electron pulse trains offers the following advantages:

- As the (longitudinal) Kapitza-Dirac effect does not require a nanostructure to allow for energy-momentum conservation, it does not suffer from electron-matter interaction, which otherwise results in electron loss due to absorption or dephasing by plasmon or phonon excitation.

- The period T of the intensity grating and thereby the separation of the attosecond peaks can be adjusted by choice of the angles $\theta_{1,2}$. Because T can acquire values around tens of femtoseconds, already rather long incident electron pulses may result in the generation of a single attosecond electron burst, which otherwise requires incident pulse durations τ shorter than the optical period (2.66 fs for $\lambda = 800\,\mathrm{nm}$).

- The interaction strength is spatially very homogeneous, as long as the electron beam diameter is kept well below the optical focal spot size.

At the same time, the following disadvantages are encountered:

- The intensity grating approach requires light intensities that are two orders of magnitude larger than for IELS to achieve the same energy broadening.[4]

- The setup is more difficult to adjust than ours, in that two laser beams and one electron beam oriented at specific angles have to be spatially and temporally overlapped. Our approach requires only one laser pulse, and its incident angle is of no importance as long as there exists a field component pointing along the electron trajectory.

- In practical applications of pulse trains for attosecond time resolved electron microscopy, the sample excitation has to be synchronised to the pulse train. This can be achieved by difference frequency mixing of the two pulses used to generate the moving intensity grating [188], but frequency conversion reduces the available pump power. In our experiment, the same high-intensity laser pulses can be used both for the phase modulation and sample pumping.

[4] The light intensity I must be strong enough to obtain an energy broadening ΔE that supports attosecond pulse durations. To achieve 15 as, a broadening of $\Delta E \approx 30\,\mathrm{eV}$ is required. As detailed in Ref. [148], for 31 keV electron pulses and an intensity grating formed by $\lambda = 520\,\mathrm{nm}$ and 1040 nm light pulses with 300 fs duration, this corresponds to $I = 8 \times 10^{11}\,\mathrm{W\,cm^{-2}}$. Inelastic electron-light scattering (with the $\lambda = 520\,\mathrm{nm}$ light pulse) achieves the same ΔE already for $I = 2.3 \times 10^{9}\,\mathrm{W\,cm^{-2}}$, assuming the same laser parameters as in Ref. [148] and typical near-field Fourier components for 30 keV electrons in the order of $0.1\,\mu\mathrm{m} \cdot F$, where F is the field strength.

Overall, the longitudinal Kapitza-Dirac effect is an interesting alternative for the generation of attosecond electron pulse trains. Geometrical constraints due to the TEM design renders an implementation into the current UTEM setup technically challenging, but the scheme may be considered for future UTEMs that feature larger pole piece gaps.

Applicability of This Work's Scheme

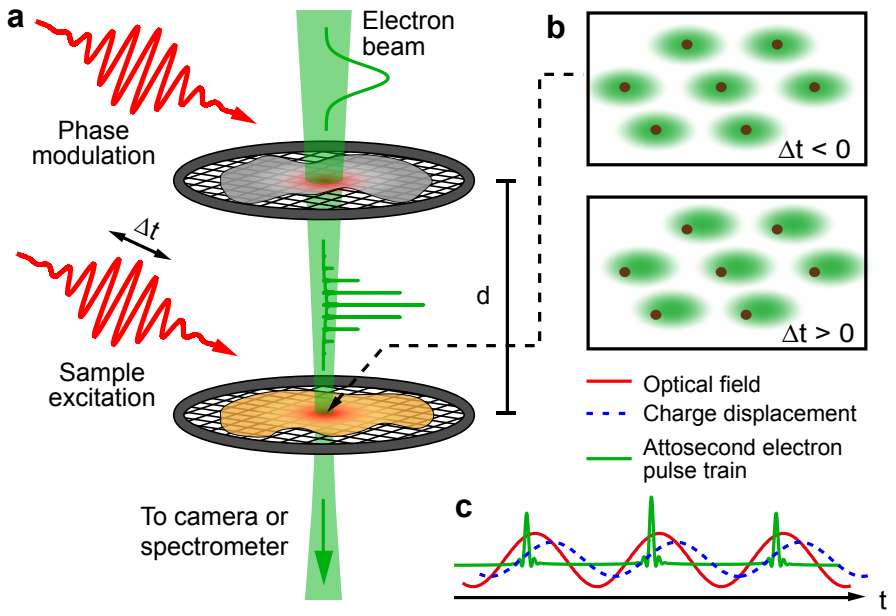

Figure 4.7: Experimental scheme for attosecond electron microscopy. **a** The electron beam is phase-modulated by IELS. Subsequent free-space propagation over a distance d reshapes the electron pulse envelope into an attosecond electron pulse train. A synchronised pump pulse optically excites a sample that is placed in the temporal focus position. A diffraction pattern, real space image or electron spectrum is recorded for varying time delays Δt between the phase-modulating and the pump pulse. **b** Microscopic cartoon of charge displacement induced by the optical field. **c** The phase-locked electron pulse train probes the sample's electron dynamics with attosecond precision.

This Section discusses the practical applicability of the attosecond electron pulse trains generated by IELS in real experiments. Figure 4.7 illustrates the considered scenario: A sample is placed at a specific distance d below the layer in which the electron pulse is phase-modulated by an optical near-field. The distance d corresponds to the temporal focus position, that is, the propagation distance for which the electron density exhibits the highest peak intensity. A pump laser beam initiates an optical-phase dependent dynamics

in the sample, for example, a charge displacement, which is probed at various time delays by the phase-locked attosecond pulse train.

To fit in the gap between the pole pieces of the TEM objective lens, the focal distance d must lie in the range of few millimetres. It can be controlled by the optical field strength and wavelength, as illustrated in Fig. 4.8**a**: Stronger couplings g and larger photon energies result in a broader electron energy distribution, corresponding to larger differences in propagation velocities, so that the bunching occurs at shorter distances. Furthermore, shorter optical periods require less phase-space shearing to reach the temporal focus. Overall, the focal distance scales as $d \propto \lambda^2/g$ [189]. Sufficient intensity provided, smaller wavelengths are thus preferable.

The achievable time resolution is determined by the minimal pulse duration of the individual density peaks in the train, which can also be controlled by the coupling strength and optical wavelength. Figure 4.8**b** shows that the pulse duration for sinusoidal phase modulations scales inversely with the coupling strength g and linearly with λ. Sub-100 as durations can be achieved for coupling constants as low as $g = 2$ for $\lambda = 400$ nm, values that are easily obtained in experiments. Note that not the sinusoidal phase modulations considered so far, but parabolic phase modulations would result in optimal pulse compression [189]. Experimentally, programmable laser pulse shaping could provide the complex optical waveforms required for optimised, non-sinusoidal phase modulations.

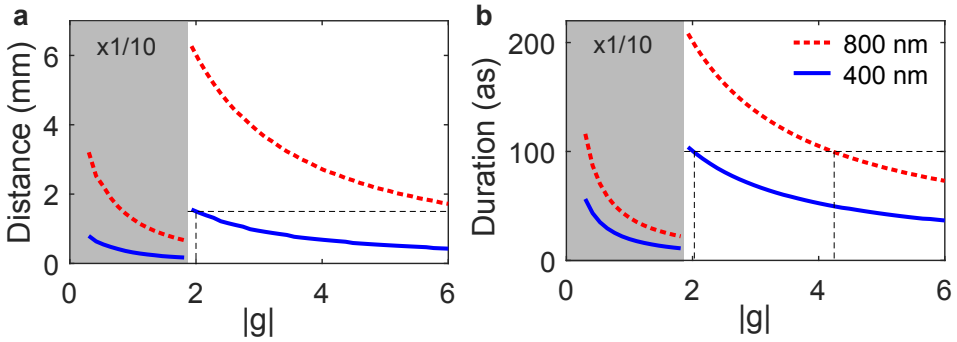

Figure 4.8: Influence of coupling strength and wavelength on pulse train properties for sinusoidal phase modulation. **a** The focal distance d decreases with increasing g. Horizontal dashed line: $d = 1.5$ mm, corresponding to the sample holder distance used in our experiments. For $\lambda = 400$ nm, this is reached for $g = 2$, while much stronger couplings are required for $\lambda = 800$ nm. **b** The FWHM pulse duration of the individual peaks in the pulse train already drops below 100 as (horizontal dashed line) for $g = 2$ at $\lambda = 400$ nm. Note that values in the grey shaded area are scaled by a factor 1/10 for clarity.

Experimental uncertainties deteriorate the best possible temporal resolution. Figure 4.9 demonstrates that the minimal pulse duration is fortunately rather robust against typical variations in the coupling strength and initial electron energy width. A distribution of initial electron energies only slightly reduces the contrast of the interference features. Since the focal distance is g-dependent, averaging over coupling strengths elongates the region of propagation distances over which the electron appears to be temporally focused without severely increasing the pulse duration.

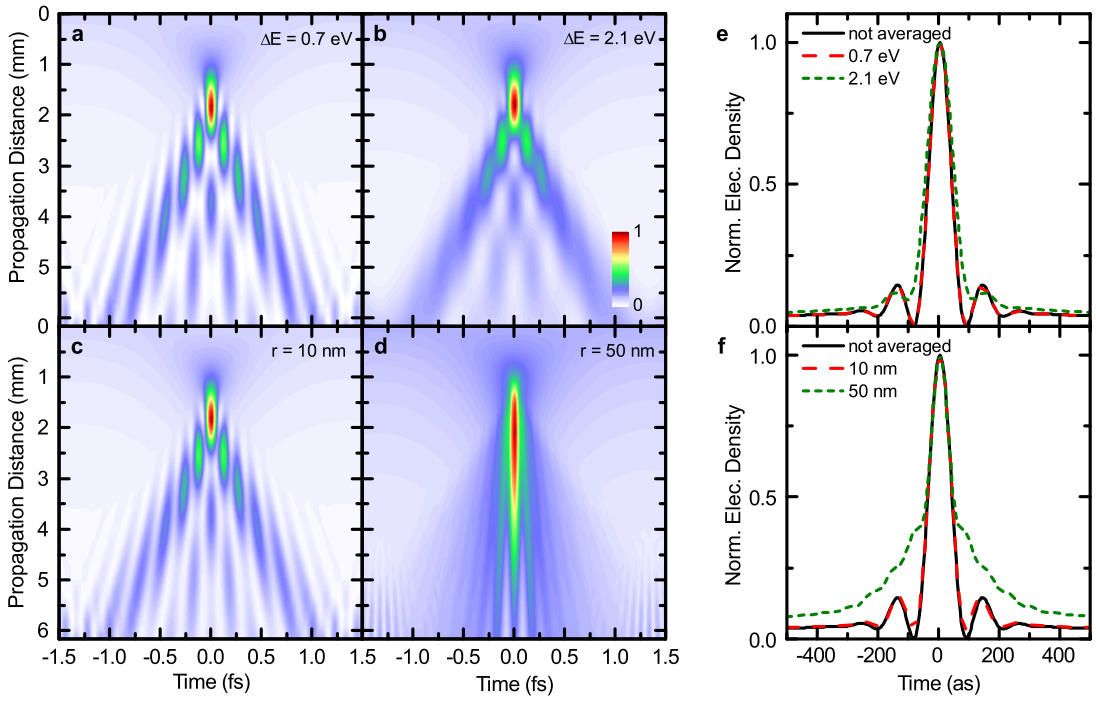

Figure 4.9: Robustness of generation of attosecond pulse trains against averaging over initial electron energies (upper row) and coupling strengths in a spatially inhomogeneous near-field (lower row, decay length 90 nm). **a**-**d** Electron density as a function of propagation distance below the electron-light interaction plane. **e**,**f** Line profiles at the propagation distance with maximum peak intensity. Reprinted with permission from Ref. [28].

In contrast, phase jitter between the phase-modulating and pump pulse convolutes the temporal electron envelope with the phase distribution and thereby easily corrupts the time resolution. Such phase matching issues will become even more critical if smaller wavelengths are used for the phase modulation. In the current setup, the active phase-stabilisation of the interferometer suppresses shot-to-shot phase variations stemming from different relative arrival times of the pulses, but near-field phase variations across the electron beam area lead to spatial phase averaging within each shot. Possible countermeasures

include cutting out a smaller part of the beam with an aperture – at the cost of significant electron loss and consequently long acquisition times – or phase-matching by sample tilting, as illustrated in Fig. 4.10. If electron and light pulses propagate parallel to each other ($\beta = 0°$), perfect phase matching would automatically be achieved over the entire interaction area. This is, however, not an option for planar samples required for spatially homogeneous coupling strengths, since there is no electric field component pointing along the electron trajectory,[5] and thus the coupling strength $g = 0$ vanishes. A simple geometric calculation shows that the optimal sample tilt angle is given by $\sin(\alpha) = \frac{v}{c}\sin(\alpha+\beta)$. The tilt angle $\beta = 55°$ between electron and laser beam in the current setup unfortunately does not allow for phase matching by sample tilt, as this requires the laser pulse to illuminate the sample almost parallel ($\xi \approx 0°$), which will lead to shadowing effects, but for smaller angles β, sample tilting will be well suitable for phase matching. In the current setup, the pulse broadening due to phase averaging was reduced to $\sigma_\phi = 80\,\text{as}$ by inserting an aperture in the beam path. In order to avoid the associated loss in electron current, phase matching by sample tilting should be implemented in future experiments.

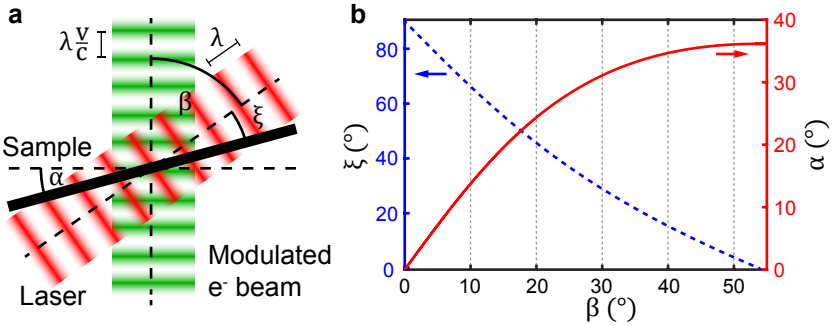

Figure 4.10: Phase matching between the laser pulse and the attosecond electron pulse train by sample tilting. **a** Geometry. **b** Sample tilt α and corresponding angle of incidence ξ of the laser beam on the sample for a given tilt angle β between electron and laser beam to achieve phase matching. Calculation for electrons with $E_0 = 120\,\text{keV}$.

In conclusion, the millimetre-scale focal distances are suitable for conventional TEM geometries. The inherent synchronism between the electron pulse train and the generating optical field allow for laser-pump electron-probe measurements with attosecond precision. Spatial phase averaging remains a challenge, but already with the current setup and sample geometry, pulse durations of few 100 as duration are within reach.

[5] Focused light exhibits weak field components that are longitudinally polarised. Furthermore, it is possible to create strongly longitudinally polarised light fields by focussing a radially polarised light beam [190], such that normal light incidence could still be an option.

Signatures in Electron Diffraction and Spectroscopy

This Section briefly considers the sensitivity of diffraction and spectroscopy to optically induced temporal changes in the charge density on the attosecond time scale, such as non-resonantly driven polarisations, resonant transitions from bonding to anti-bonding states and excitation of coherent superpositions of different electronic states.

Since atomic positions are essentially frozen on attosecond time scales, Bragg spot positions in the diffraction patterns remain fixed. Electron density variations, however, alter the scattering cross section and thus the Bragg spot intensities. Numerical studies of electron diffraction in prototype systems like hydrogen molecules and graphene using isolated attosecond electron pulses predict well observable, few percent intensity changes in the diffraction spots [191–195], but their interpretation may be challenging.

Attosecond electron pulses require several tens of eV bandwidth, so that spectral details narrower than this bandwidth may be obscured in spectroscopic measurements. Shao *et al.* theoretically investigated the feasibility of energy-resolved attosecond electron diffraction [196]. They showed for the simple system of an H atom that a good compromise between spectral and temporal information can be made and that spectroscopic measurements give valuable additional information on inelastic probe-sample interactions, which cannot be obtained from imaging or diffraction alone.

So far, the numerical studies considered the ideal case of isolated attosecond electron pulses. It remains to be analysed which kind of information on attosecond charge dynamics are retrievable from time-resolved diffraction or spectroscopy with attosecond electron pulse trains. Besides, the present theoretical models will have to be extended to the description of more complex materials to facilitate the interpretation of experimental data.

Lastly, it should be noted that the broad energy distribution does not only influence the spectral, but also the spatial resolution. Because electron optics exhibit chromatic aberration, an energy difference ΔE with respect to the initial energy $E_0 = e \cdot U$ results in a displacement in the image plane by $\delta = C_c \Delta E / U\beta$, where C_c is the coefficient of chromatic aberration, $U = 120\,\mathrm{keV}$ the acceleration voltage and β the collection angle [197]. In attosecond electron microscopy as proposed in this work, the loss in resolution by chromatic aberrations would be present for any time delay between the laser pump and the attosecond electron probe pulse and not only during temporal overlap, since the incident electron pulse would have to be energy-broadened. Plemmons and Flannigan estimate a moderate deterioration of resolution for energy widths $\Delta E \approx 30\,\mathrm{eV}$ [197], which would

be required for sub-100 attosecond pulses, indicating that simultaneous sub-nanometre spatial and attosecond temporal resolution should be achievable. Furthermore, chromatic aberrations could be reduced by improved C_c correctors [198, 199].

Isolated Attosecond Electron Pulses

The possibility to generate attosecond electron pulse trains marks already a major step forward in the field of time-resolved electron microscopy. In principle, they allow for the study of attosecond dynamics, however, the processes under study must be temporally confined to less than one optical cycle or have the periodicity of the driving field. Otherwise, averaging over parameters that change from cycle to cycle would prohibit the extraction of useful information from the data, since the measured signal is accumulated over many cycles. Just as for attosecond light pulses, the next important step will therefore be the generation of isolated attosecond electron pulses, due to the fact that they allow to study a broader range of processes.

Isolated attosecond pulses can be obtained by optical phase-modulation if the incident electron pulse is already shorter than the optical period. This would, however, require pre-compression stages as mentioned in Sec. 1.4. Alternatively, one could isolate a single attosecond peak from the train, e.g. by deflecting all other cycles by transverse acceleration with an optical field [145]. This "attosecond light house" [200] for electrons would, however, come at the expense of significant loss in count rate.

Another route towards isolated attosecond electron pulses is based on energy filtering and was suggested already soon after the discovery of PINEM [93, 150, 201]. It relies on the fact that inelastic electron-light interaction is instantaneous, i.e. the photon sidebands in the electron energy spectrum are only significantly populated during the presence of the light field. Consequently, the part of the electron wavepacket that gained energy has a duration that is comparable to the light pulse and can be isolated by energy filtering. Because space-charge induced pulse broadening is not limiting the temporal resolution in this scheme, the number of electrons per pulse may be chosen much larger than one, so that the gated electron pulse can deliver enough electrons to the sample to achieve a good signal-to-noise ratio in the images.

A modified version of temporal gating could employ polarisation-shaped laser pulses, that are experimentally easier to achieve than optical attosecond pulses. In analogy to polarisation gating for single attosecond light pulses [202], IELS could be temporally

confined to less than one optical cycle by a fast modulation of the laser polarisation state in combination with a polarisation-sensitive nanostructure, such as a planar graphite flake, without the explicit need for attosecond optical excitation.

4.3.3 Novel Seed for Free-Electron Lasers?

Bunching of freely propagating electrons is not only of interest for ultrafast electron microscopy: Free-electron lasers (FELs) heavily rely on electron bunching in order to produce coherent electromagnetic radiation. While the underlying electron-light interaction leading to bunching is somewhat different, it might be worthwhile to consider coherent electron-light scattering as a tool for the seeding of x-ray FELs.

Details on the physics of FELs can be found in the review by Pellegrini *et al.* (Ref. [203]), which will be briefly summarised here. The FEL, invented by Madey in 1971, uses free electrons as a lasing medium. An undulator consisting of dipole magnets with periodically alternating magnetic fields forces the electrons to travel on a sinusoidal trajectory, giving rise to synchrotron radiation due to the transverse acceleration. Initially, the spontaneous emission of photons is incoherent. In an optical cavity, the radiation forms a standing wave which ponderomotively accelerates the electrons. This leads to a periodic bunching of the electrons and thus to coherent emission of radiation, since all bunches emit in phase. X-ray FELs are particularly challenging due to the lack of high quality x-ray mirrors that would be required for a cavity. Instead, the electrons are bunched by self-amplified spontaneous emission (SASE) during the propagation in a long undulator. SASE comes at the cost of a random start of the bunching process leading to poor longitudinal coherence and large pulse-to-pulse fluctuations, that are a major challenge for x-ray FELs.

A possible remedy against these fluctuations is seeding, and a number of different approaches have been developed, including direct seeding, self-seeding, high-gain harmonic generation (HGHG) [204] and echo-enabled harmonic generation (EEHG) [205]:

- In *direct seeding*, electromagnetic radiation at the FEL resonant wavelength is coupled to the electrons. This requires, however, strong radiation sources at these wavelengths. For soft-x-ray wavelengths, HHG is a promising candidate.

- In *self-seeding*, the undulator is split in two parts. The SASE FEL radiation of the first part is spectrally cleaned and used as a seed for the second part.

- In *High-Gain Harmonic Generation* (HGHG) [204], a seed laser modulates the energy of the electrons, which is transformed in a chicane into a density modulation with pronounced peaks that contain higher harmonics. A second FEL stage called *radiator* is tuned to a specific harmonic of the seed laser, which is then amplified. This approach is, however, limited to lower harmonics, as high harmonics require large energy modulations, which at a certain level become too strong to support high-gain FEL amplification. Very high harmonics can be reached by *Echo-Enabled Harmonic Generation* (EEHG) [205], which is based on two modulator stages.

In some analogy to HGHG and EEHG, coherent electron-light scattering may present another option to seed a FEL. One deals, however, with very different regimes in terms of electron energy and density: The UTEM currently operates in a one-electron per pulse mode at 120 keV kinetic energy, while FELs typically employ $10^8 - 10^9$ electrons per bunch at 20 GeV. At present, it is unclear if the concept works at all for such high energies and electron numbers, regarding for example space-charge effects. An option could be to phase-modulate the electron beam at few 100 keV energies using optical wavelengths and then automatically reach x-ray wavelengths by Lorentz contraction due to acceleration to the GeV range, but space-charge broadening will be huge as long as the electron pulse's energy is small. Space-charge effects play a minor role in the GeV regime, but phase modulation at x-ray wavelengths will have to cope with the same problem that appears in direct seeding, that is seeding with the FEL resonant wavelength: It requires intense x-ray sources, that are not available.

An advantage from the experimental point of view would be the easier alignment: The light field does not need to co-propagate with the electrons, but only overlap temporally and spatially at the interaction plane. Because it is a first-order electron-photon interaction, IELS may be more efficient, i.e. require smaller field strengths compared to ponderomotive electron acceleration that is a second-order process.

Besides seeding, IELS may be an interesting alternative for further FEL methods that rely on energy modulation of the electron beam. For example, ultrashort x-ray pulses can be generated by slicing [206], which is conceptually strongly related to the proposed energy slicing method for the generation of isolated attosecond electron pulses [93, 201] mentioned in Sec. 4.3.2. In this technique, only a part of the electron beam is energy-modulated by an ultrashort laser pulse. Because the energy modulation is larger than the energy width of the electron beam, the modulated part can be spatially separated from the

rest of the beam by a bending magnet, so that the radiation from this part is emitted in a different direction. These ultrashort x-ray pulses could then be spatially filtered out.

At present, it is unclear if IELS brings advantages compared to the current techniques used in FEL facilities. It is for instance an open question if IELS is able to obtain larger bunching factors or x-ray pulses with higher temporal coherence. This will have to be clarified in future work.

4.3.4 Reconstructing the Quantum State in a Continuous Energy Basis

This Section outlines a possible route towards high-resolution (HR) SQUIRRELS, i.e. an extension of SQUIRRELS to a continuous energy basis.[6] No concrete algorithm has been developed yet, but concepts and generally conceivable components for future algorithms will be discussed below.

In SQUIRRELS as introduced in this work, the free-electron quantum state is described in a discretised basis of momentum states $\{|N\rangle\}$, where N corresponds to the number of absorbed or emitted photons. All information contained in the spectrogram sidebands is thus cast into a single number, and more detailed properties of the initial electron state ρ_0 are not characterised. HR-SQUIRRELS would aim at retrieving this information.

Figure 4.11 illustrates several possible initial quantum states ρ_0. If all photoelectrons emitted from the nanotip are identical, i.e., they all have identical emission times relative to the photoemission pulse, identical central energies and identical coherent energy widths, the ensemble average over several shots can be described as a pure quantum state. The upper two rows depict such coherent wavepackets before (**a**) and after (**b**) free-space propagation. The temporal evolution is described by Eq. 2.8, i.e. by a phase-shift that is quadratic in p, which is clearly visible in the density matrix in Fig. 4.11**b**. Dispersion is more intuitively pictured in the Wigner function, which becomes sheared due to the different velocities arising from the finite energy width.

A realistic electron pulse will not be describable as a coherent wavepacket, given that photoemission is a statistical process [207]. For instance, the emission time is distributed within the temporal envelope of the laser pulse and the initial energy varies from shot to shot due to the excess photon energy above the metal work function, as the photoelectron can be emitted from different levels within the conduction band. Both effects lead to

[6] Continuous refers to choosing the discretisation step ΔE in the numerical implementation much smaller than the photon energy $\hbar\omega$.

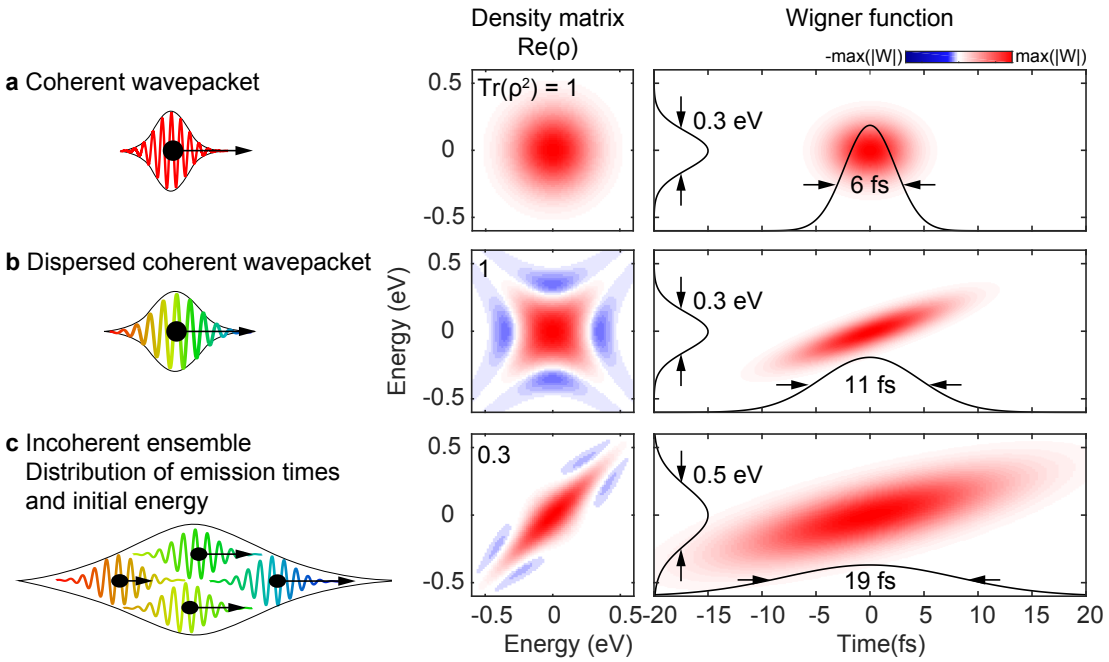

Figure 4.11: Exemplary quantum states of an electron pulse. Left column: physical picture, middle column: density matrix, right column: Wigner function (colour scale) and marginal distributions (solid black lines). **a** Gaussian wavepacket with coherent energy width 0.3 eV. **b** The same wavepacket as in **(a)** after free-space propagation over 2 m. Dispersion introduces a quadratic phase, leading to a spreading of the wavefunction and a shearing of the phase space distribution. **c** The off-diagonal terms in the density matrix are suppressed for an incoherent Gaussian distribution of electron wavepacket emission times (5 fs standard deviation) and an incoherent Gaussian distribution of initial energies (0.16 eV standard deviation). Both the energy width and pulse duration of the ensemble are increased. The number in the upper left corner of the density matrix plots states the purity $\mathrm{tr}(\rho^2)$ of the quantum states. Note that the energy axes are given with respect to the central energy $E = 120\,\mathrm{keV}$ of the electron pulse.

varying arrival times at the sample. Consequently, the electron ensemble is in a mixed state, such as the one illustrated in Fig. 4.11**c** with purity $\mathrm{tr}(\rho^2) = 0.3$. Similar to the mixed states discussed in Sec. 4.2.1, the coherence terms (off-diagonal elements) in the density matrix of the incoherent electron ensemble are strongly suppressed.

Unfortunately, the different states illustrated in Fig. 4.11 cannot be distinguished in the $\{|N\rangle\}$ basis. Besides, a discretised description is insufficient if the bandwidth of the optical excitation is on the order of the electron energy width so that the electron-light interaction alters the sideband shape. A quantum state reconstruction that uses a continuous momentum basis is desirable, as it is more generally applicable and gives more detailed information.

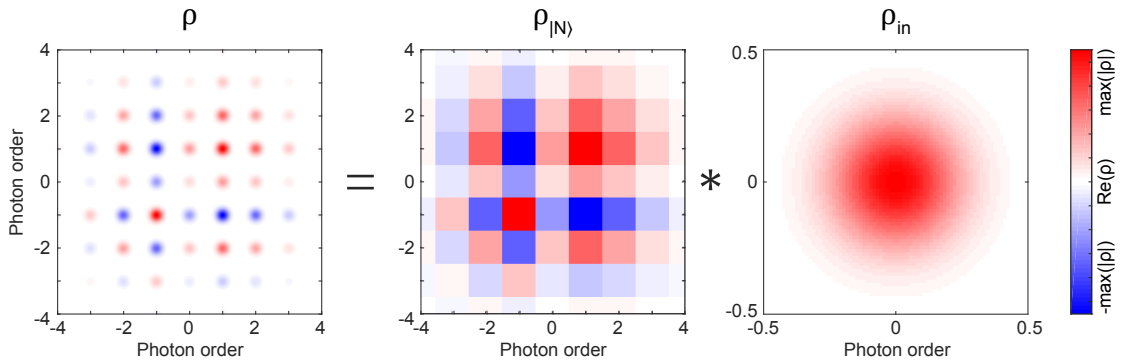

Figure 4.12: For IELS with continuous-wave optical fields, the final density matrix ρ is given by a convolution of the incident state ρ_{in} and the final state in a discrete momentum basis $\rho_{|N\rangle}$. Note the different scaling of the axes. Calculation for initially Gaussian wavepacket with energy width smaller than the photon energy and coupling strength $g = 1$.

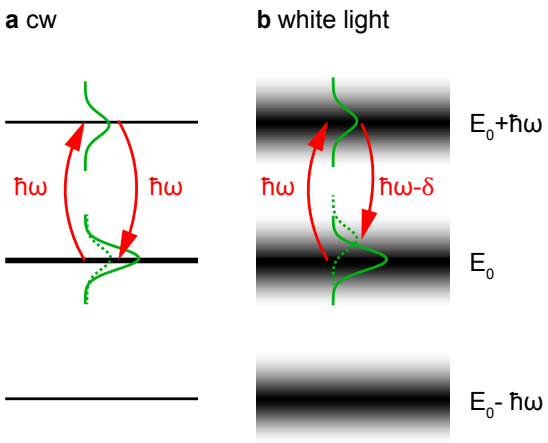

Figure 4.13: Energy level diagram. **a** For continuous-wave excitation, the sidebands are energetically sharp. Photon absorption and subsequent emission shifts a part of the wavepacket back to its initial energy, and the sideband shape remains unchanged. **b** The large bandwidth of white light broadens the energy levels (black shaded area). Multi-photon interactions may result in a significant energy shift δ on the order of the electron energy width. Interference between different parts of the wavepacket modulates the sideband shape.

The energy spectrum and temporal envelope of the electron pulse are experimentally easily accessible with the spectrometer by recording a single spectrum or an electron-photon cross-correlation, respectively. As discussed in Sec. 1.2, knowledge of these two marginal distributions of the Wigner function is yet insufficient to reconstruct the quantum state. Building upon the same principle that underlies SQUIRRELS, the off-diagonal elements of the fine-resolved density matrix should be retrievable by interfering different parts of the electron spectrum within one sideband with each other. As illustrated in Fig. 4.12 and 4.13**a**, this cannot be achieved by IELS with continuous light fields, since the entire energy spectrum is shifted between energetically narrow photon sidebands, and no information on the inner-sideband spectral phase is gained. If, however, white light with a

large bandwidth on the order of the coherent energy width of the electron wavepacket ΔE was used, the energy levels would be broad and allow for effective energy shifts $\delta \approx \Delta E$ (Fig. 4.13**b**). Information on the spectral phase would be encoded in the resulting shape of the sideband, which would be modulated due to interference between different parts of the wavepacket. By introducing a well-characterised chirp in the broadband laser pulse, each modulation frequency could be mapped onto a specific interaction time. The final electron energy spectrum recorded in dependence of the time delay between the chirped laser and the electron pulse should contain enough information to recover the coherence terms of the electron quantum state in a quasi-continuous momentum basis.

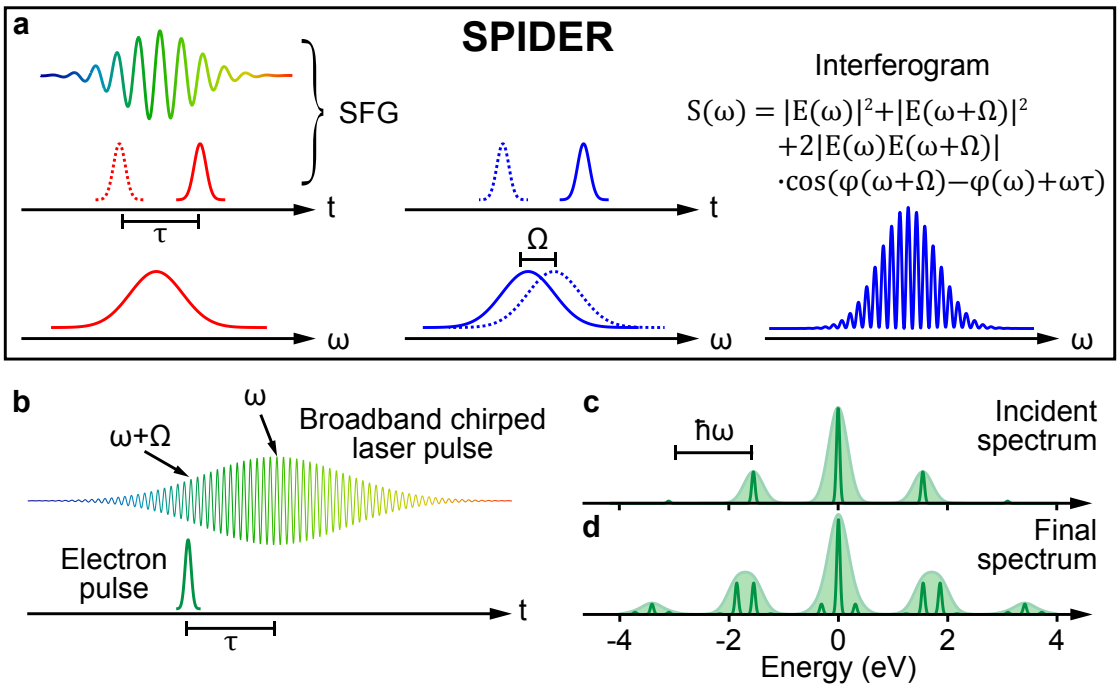

Figure 4.14: Comparison of SPIDER to HR-SQUIRRELS. **a** Principle of SPIDER: Sum frequency generation (SFG) of a chirped pulse and two time-delayed replica of the unchirped pulse results in two pulses that are spectrally shifted by Ω. The spectral phase $\phi(\omega)$ is encoded in the interference pattern that can be measured with a spectrometer. **b** In the to be developed method of HR-SQUIRRELS, the electron pulse that is in a specific momentum superposition state could be characterised by phase-modulation using a broadband, chirped laser pulse. The instantaneous modulation frequency $\omega + \Omega$ could be adjusted by the time delay τ between electron and laser pulse. **c**, **d** Expected incident and final electron energy spectra before and after interaction with a chirped laser pulse, respectively. Spectral interference would result in strongly modulated sideband shapes (solid green line), that would, however, be masked by the 0.4 eV spectrometer resolution (green shaded area).

The proposed scheme is conceptually related to the pulse characterisation technique SPIDER (Spectral Phase Interferometry for Direct Electric-field Reconstruction) [171], which retrieves the spectral phase of ultrashort optical pulses by spectral shearing interferometry. Note that SPIDER, like FROG and RABBITT, does not account for partial coherence, whereas HR-SQUIRRELS would reconstruct the density matrix. Figure 4.14**a** illustrates the principle of SPIDER: Two spectrally shifted replica of an ultrashort optical pulse are produced by sum frequency generation of two temporally delayed copies of the pulse with another chirped copy of the pulse. The resulting interferogram is strongly modulated due to spectral interference between the two spectrally shifted pulses and allows for an unambiguous reconstruction of the spectral phase $\phi(\omega)$ with a non-iterative algorithm. Similarly, in HR-SQUIRRELS, spectral quantum interference between different parts of the electron wavefunction would modulate the sideband shapes. In contrast to SPIDER, no simple spectral shear would be employed in this proposal. A one-to-one transfer of SPIDER from optical to electron pulses would require the electron wavefunction to be split in two parts, one of which is energetically shifted, and then recombined to record the interference in the energy spectrum.[7] Instead, the entire wavefunction would be phase-modulated by a laser pulse in such a way that all sidebands are mixed with each other. Because a chirped laser pulse would be used, the electron pulse would effectively "see" a modulation frequency that is detuned by Ω with respect to its initial sideband separation ω, as illustrated in Fig. 4.14**b** and **c**. Other than in the current version of SQUIRRELS, where $\Omega = 0$, two sidebands that are separated in energy by $N \cdot \hbar\omega$ would thus be interfered at an energy shift $N \cdot \hbar\Omega$, so that information on both the phase difference between the sidebands as well as the spectral phase within each sideband would be acquired.

An open question that will have to be answered in future work is to what extent the finite energy resolution compromises quantum state reconstruction in a (quasi-)continuous momentum basis. The 0.4 eV energy resolution of the current electron spectrometer is insufficient to observe modulations within a sideband (cf. Fig. 4.14**d**), but preliminary simulations that include the spectrometer resolution indicate that different incident electron quantum states nonetheless yield observable changes in the spectrogram.

On the algorithm side, optimisation in terms of computational speed is required, given that the current algorithm needs several minutes of computing time on a standard PC

[7] Apart from experimental complications, this approach would fail at retrieving the phase relation between the sidebands, because the electron energy spectrum contains many gaps due to the sideband structure.

for matrix sizes on the order of 20×20 elements, so that the handling of thousands of elements would become impractical. One may also consider alternative algorithms, such as the MSGPA mentioned in Sec. 4.2.3.

4.3.5 Quantum-State Electron Microscopy

The ability to characterise the electron quantum state in a TEM could be applied as a novel modality of electron microscopy that analyses (time-dependent) changes in the state resulting from interactions with matter. Quantum-state electron microscopy could be realised as illustrated in Fig. 4.15: The electrons traverse three subsequent interaction planes. In the first plane, the electron is prepared in a specific quantum state by optical phase-modulation. In the second plane, another optical field (generally with different parameters than the first) initiates some dynamics in a sample, which is probed at a certain time-delay Δt by the phase-modulated electron pulse. The resulting quantum state of the electron is then characterised by interacting with a laser pulse in the third plane. Energy spectra or diffraction patterns to reconstruct the longitudinal or transverse momentum components (see Sec. 4.3.1), respectively, are recorded in dependence of the phase shift $\Delta\varphi$ between the first and a third laser pulse. The time-dependent electron density matrix $\rho(\Delta t)$ is reconstructed from the corresponding spectrograms or diffraction patterns for each value of Δt by SQUIRRELS or its future continuous and/or transverse variants.

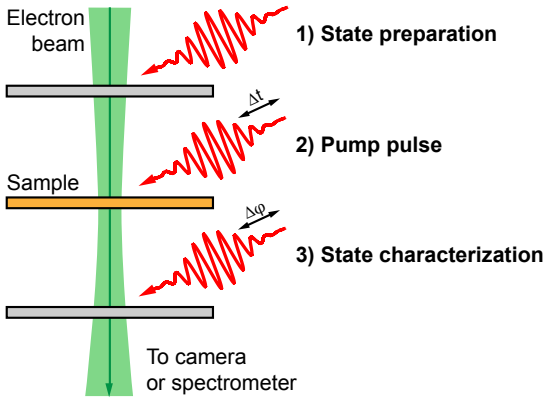

Figure 4.15: Proposed setup for quantum-state electron microscopy. The incident electron beam may contain single or multiple, possibly degenerate or entangled, electrons and traverses three interaction planes. The first and third are used to prepare and characterise the electron quantum state, respectively, and the second contains the actual sample, which may be pumped by classical (laser) light or quantum light, e.g. Schrödinger cat states [132].

If the density matrix is reconstructed in the longitudinal momentum basis, quantum-state electron microscopy will be sensitive to inelastic processes such as coupling to phonons or plasmons, that result in energy losses in the meV or eV range, respectively. Determining the transverse momentum representation of the electron density matrix could

perhaps yield information on the decay of spatial coherences, which is important for electron transport in nanoscale solid-state electronic devices [208]. Initially, the sample and electron quantum states are factorisable and the total density matrix can be written as $\rho = \rho_{\text{sample}} \otimes \rho_{\text{el}}$. Interactions will entangle the electron with the sample, so that the quantum state of the whole system comprising both electron and sample can no longer be described as a tensor product of the electron and sample state. Because only the electron is measured, the sample subspace is traced out and the purity of the electron quantum state will appear reduced, even if the state of the whole system is pure.

Many exciting open questions come to mind when thinking about the prospects of quantum-state electron microscopy: What information can be inferred about the sample from measuring the quantum state of the transmitted electrons? Can quantum-state electron microscopy obtain (time-resolved) information on decoherence? Can continuous-variable quantum state tomography help to distinguish low-loss inelastic phonon scattering within the electron energy bandwidth from elastic scattering, which is not possible with conventional EELS? How does the transmitted electron quantum state depend on the optical excitation of the sample? Can we learn more about many-body physics by exciting the sample with quantum light instead of classical light (i.e., laser light) as in quantum optical spectroscopy [132, 209], but probing with electrons? What kind of additional information do we gain by probing with electrons that were prepared in specific quantum states? What happens if degenerate multi-electron beams [210] are used as a probe [24]? Thorough theoretical and experimental work that answers these questions will shed light on quantum properties of matter.

4.3.6 Free Electrons as "Quantum Hardware" for Quantum Technologies?

Lasers, transistors and atomic clocks are the prime examples that demonstrated the usefulness of quantum effects in the so-called "first quantum revolution". The ongoing "second quantum revolution" [211] builds on the ability to prepare, manipulate and characterise quantum states. Entanglement and superposition are considered key resources for novel devices in the four areas communication (in particular cryptography), sensing, simulation and computation. There is great interest in quantum technologies, since they are expected to surpass classical devices in many aspects. Various quantum systems, including photons, trapped ions, nuclear spins, superconducting qubits and quantum dots are currently investigated [212]. This Section speculates about the question for which quantum tech-

nology applications free-electron momentum superposition states could be harnessed as a new kind of "quantum hardware".

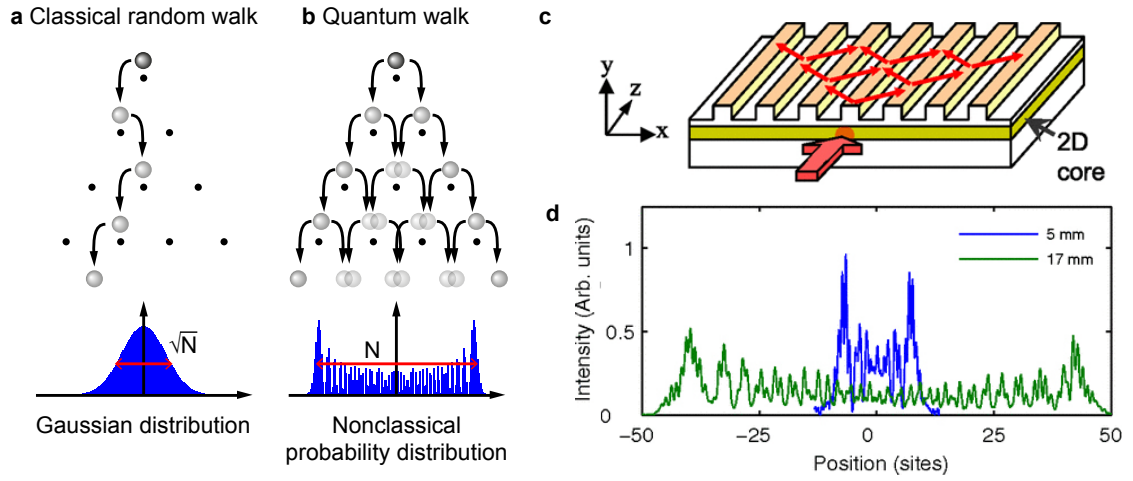

Figure 4.16: a,b Illustration of a (discrete) classical and quantum random walk on a Galton board. The width of the probability distribution scales as $\sqrt{N}$ for the classical and N for the quantum walk, respectively, where N is the number of steps. **c** Sketch of an optical waveguide array for the experimental realisation of a (continuous) quantum random walk with photons. **d** Measured intensity pattern at two different propagation distances. (**c**,**d**) reprinted with permission from Ref. [213].

Real quantum systems are usually too complex to be simulated on a classical computer, but often the quantum dynamics can also not easily be accessed in experiments. Here, quantum simulators come into play: Though not able to perform arbitrary computations as quantum computers, they are tailored to solve specific problems. Quantum simulators mimic the quantum system under investigation, but offer better experimental control. One kind of quantum simulators is based on quantum random walks (Fig. 4.16**b**), that also attract much attention due to a potential speed up of search algorithms [214–216]. Inelastic electron-light scattering corresponds to a continuous quantum random walk on an equidistant energy ladder and may thus be interesting for quantum simulation and search algorithms. An analogous quantum random walk was studied in photonic integrated circuits, namely evanescently coupled waveguide arrays (see Fig. 4.16**c**) [213, 217, 218]. In fact, the same pattern as observed for the energy distribution of sinusoidally phase-modulated free electrons was obtained for laser light propagating in such an array (Fig. 4.16**d**). Both the coupling strength between neighbouring waveguides and the dispersion properties of each individual waveguide can be geometrically tailored in photonic integrated circuits

[219], which allows to simulate different quantum mechanical systems and phenomena, for instance Bloch oscillations [218]. Inelastic electron-light scattering does unfortunately not offer such flexibility, but it may still be worthwhile to work further in this direction for several reasons. Firstly, electrons in vacuum are practically decoherence free and the light-induced energy ladder does not exhibit any imperfections, so that a large number of sidebands can be coupled coherently. Secondly, if electrons are used instead of photons, multi-particle quantum random walks that contain entanglement and therefore have no classical analogy [217, 220] will exhibit new features due to the fermionic nature of electrons, in particular the Pauli exclusion principle [24] and superselection rules that forbid coherent superpositions of even and odd numbers of fermions [221]. The high degeneracy of the multi-electron beams necessary for such experiments could possibly be achieved by temporal and spatial focusing of the electron pulses [24].

The highest expectations of all envisioned quantum technologies are probably raised by quantum computation. Swift free-electrons will, however, not be a suitable candidate for its realisation, since except for the third, they do not very well meet DiVincenzo's criteria [222], according to which quantum computation requires:

1. A physical system that is scalable and consists of well-characterised qubits,
2. a way to initialise the qubits in a specific state,
3. coherence times that exceed the gate operation times,
4. a set of universal quantum gates, and
5. a way to measure (read out) specific qubits.

As a side remark, it should be noted that the free-electron momentum superposition states present qudits and not qubits as they involve more than two energy levels, but it was shown that universal quantum gates can also be designed for qudits [223]. Qudits even promise advantages compared to qubits in terms of information storage and processing as well as channel capacity. The main problem with free electrons is that computation, i.e., the gate operations, require a controlled way to interact with *multiple* electrons such that every electron can be addressed *individually*. In the current experiment, the electron pulses contain at most a single electron. While the number of electrons can be easily increased, it is neither possible to interact with, nor to read out the state of a specific electron, not

to mention controlling interactions between multiple specific electrons that would be required for two-qudit gates. Computation with a single free-electron, in contrast, easily fulfils criteria 2, 3 and 5, and a limited number of single-qudit quantum gates should be implementable.

The quantum technology branch for which free-electron momentum superposition states will probably be more interesting is quantum metrology or quantum sensing. One example is Ramsey-type electron light interferometry presented in Chap. 2, that could be exploited for precise phase measurements. As briefly touched upon in Chapter 2, a possible application of the electron-light interferometer would be the time-resolved study of electronic dephasing. To this end, a sample could be placed in between the two interaction regions and the amount of dephasing could be inferred from the broadening of the final energy distribution. While in this approach the measurement of only a single energy spectrum would be sufficient, the retrieval of information on dephasing would be rather indirect. Therefore, quantum state tomography to characterise the free-electron state before and after electron-sample interaction as suggested in Sec. 4.3.5 will be much more convenient.

After all, many applications of free-electron quantum control will most likely be unforeseen, and further explorations of the emerging field of free-electron quantum optics will certainly deliver exciting and surprising insights into the fundamentals of light-matter interaction.

Chapter 5

Appendix

5.1 Quantum Description of Inelastic Electron-Light Scattering

5.1.1 Matrix Representation of Unitary Operator

Prepared by interaction with a time-harmonic electric field, the free-electron quantum states can be described in a discrete basis $\{|N\rangle\}$ of momentum states that is given by plane wave states with energy $E_0 + N\hbar\omega$. These are the eigenstates of the unperturbed Hamiltonian $H_0 = p^2/2m$ of a free electron: $H_0|N\rangle = (E_0 + N\hbar\omega)|N\rangle$. As introduced in Ref. [28], the transitions between the light-induced sideband energy levels can be described by raising and lowering operators $a^\dagger$ and a, which act upon the basis states $|N\rangle$ as follows:

$$a^\dagger|N\rangle = |N+1\rangle\,, \quad a|N\rangle = |N-1\rangle\,. \tag{5.1}$$

Note that these operators are different from the harmonic oscillator ladder operators, which introduce a coupling constant $\sqrt{N}$ and do not commute, whereas here $aa^\dagger = a^\dagger a$. Inelastic electron-light scattering transforms the incident electron quantum state ρ into

$$\rho_{\text{out}}(\varphi) = U(\varphi)\rho U^\dagger(\varphi), \tag{5.2}$$

where φ is the phase of the coupling constant $g = |g|\exp(i\varphi)$ with respect to some time reference (usually given by another optical field) and U is a unitary operator given by [28]

$$U(\varphi) = \exp(ga^\dagger - g^* a) = \exp\left(|g|\left(e^{i\varphi}a^\dagger - e^{-i\varphi}a^\dagger\right)\right). \tag{5.3}$$

In the following, the representation of U in the basis $\{|N\rangle\}$ will be derived following the approach in Ref. [28]:

$$\langle N|\exp\left(-g^{*}a\right)=\sum_{n=0}^{\infty}\frac{\left(-g^{*}\right)^{n}}{n!}\langle N|\,a^{n}=\sum_{n=0}^{\infty}\frac{\left(-g^{*}\right)^{n}}{n!}\langle N+n| \tag{5.4}$$

$$\exp\left(ga^{\dagger}\right)|M\rangle=\sum_{n=0}^{\infty}\frac{g^{m}\left(a^{\dagger}\right)^{m}}{m!}|M\rangle=\sum_{n=0}^{\infty}\frac{g^{m}}{m!}|M+m\rangle \tag{5.5}$$

Combining Eq. 5.4 and 5.5 and using the sum representation of the Bessel function [224]

$$J_{N}(x)=\sum_{k=0}^{\infty}\frac{(-1)^{k}}{k!(N+k)!}\left(\frac{x}{2}\right)^{2k+N}, \tag{5.6}$$

one obtains for the N,M element of the matrix representation of U

$$\begin{aligned}U_{NM}(\varphi)=\langle N|\,U(\varphi)\,|M\rangle&=\sum_{n=0}^{\infty}\sum_{m=0}^{\infty}\frac{\left(-g^{*}\right)^{n}g^{m}}{n!m!}\underbrace{\langle N+n|M+m\rangle}_{\delta_{N+n,M+m}}\\&=\sum_{n=0}^{\infty}\frac{\left(-g^{*}\right)^{n}g^{N-M+n}}{n!(N-M+n)!}=g^{N-M}\sum_{n=0}^{\infty}\frac{\left(-|g|^{2}\right)^{n}}{n!(N-M+n)!}\\&=\frac{g^{N-M}}{|g^{N-M}|}J_{N-M}(2|g|)=e^{i(N-M)\varphi}J_{N-M}(2|g|).\end{aligned} \tag{5.7}$$

Starting from the pure initial state $\rho_0=|0\rangle\langle 0|$, that is $(\rho_0)_{NM}=\delta_{N0}\delta_{M0}$ with the sideband numbers N and M, where $N=0$ labels the initial state, the matrix elements of the final state are then given by

$$\left(U(\varphi)\rho_{0}U(\varphi)^{\dagger}\right)_{NM}=e^{i(N-M)\varphi}J_{N}(2|g|)J_{M}(2|g|), \tag{5.8}$$

which corresponds to the outer product of the pure state vector $|\psi\rangle=\sum_{N}e^{iN\varphi}J_{N}(2|g|)\,|N\rangle$.

5.1.2 Spectrogram

In SQUIRRELS, an unknown state ρ is transformed into a different, phase-dependent state $\rho'(\varphi)$ by the unitary operator $U(\varphi)$. Energy measurements, described by the projection operators $\Pi_N = |N\rangle\langle N|$, result in spectrogram values

$$\begin{aligned} p_{N,\varphi} &= \mathrm{tr}\left(\Pi_N \rho'(\varphi)\right) = \mathrm{tr}\left(\Pi_N \left[U(\varphi)\rho U(\varphi)^\dagger\right]\right) \\ &= \mathrm{tr}\left(\left[U(\varphi)^\dagger \Pi_N U(\varphi)\right]\rho\right) = \mathrm{tr}\left(\Pi_N(\varphi)\rho\right). \end{aligned} \tag{5.9}$$

This equation offers an intuitive interpretation: For state tomography, one has to measure projections of the state in several directions. In analogy to conventional tomography in three-dimensional space, this can either be achieved by rotating the object (here: the quantum state ρ) and keeping the measurement apparatus fixed (here: the projection operator Π_N) or by rotating the apparatus around a fixed object. In SQUIRRELS, this "rotation" of ρ or Π_N is performed by the unitary operator $U(\varphi)$. By inserting Eq. 5.7 in Eq. 5.9, one obtains

$$p_{N\varphi} = \left(\rho'(\varphi)\right)_{NN} = \sum_{jk} e^{i(j-k)\varphi} J_{N-j}(2|g|) J_{N-k}(2|g|) \rho_{jk} \tag{5.10}$$

The task of SQUIRRELS is to extract the ρ_{jk} from these $p_{N\varphi}$ for given values of φ, N and g. Interestingly, the M^{th}-order Fourier component of $p_{N\varphi}$ is directly connected to the M^{th} side diagonal of ρ via

$$\begin{aligned} \int_0^{2\pi} \frac{\mathrm{d}\varphi}{2\pi} p_{N\varphi} e^{-iM\varphi} &= \sum_{jk} \underbrace{\int_0^{2\pi} \frac{\mathrm{d}\varphi}{2\pi} e^{i(j-k-M)\varphi}}_{\delta_{j-k,M}} J_{N-j}(2|g|) J_{N-k}(2|g|) \rho_{jk} \\ &= \sum_j J_{N-j}(2|g|) J_{N-j-M}(2|g|) \rho_{j,j+M} \end{aligned} \tag{5.11}$$

This means that pronounced, fast oscillations of the N^{th}-order sideband population in dependence of the relative phase φ indicate a large coherence and a correspondingly high purity of the incident state ρ. Also, Eq. 5.11 once more shows that coupling constants g on the order of the maximum value of $N - M \approx \Delta E / 2\hbar\omega$ are required to obtain sufficient information also on the highest order coherences, as the Bessel function $J_{N-M}(2|g|)$ tends to zero if $N - M \gg 2|g|$.

5.2 Analytic Description of Near-field at Flat Surface and Cylinder

The coupling constant g, which is proportional to the optical field strength F and given by the Fourier transform of the optical near-field along the electron trajectory, evaluated at $k = \omega/v$, can be controlled by F and by the shape of the near-field. To analytically determine the coupling constant g, the electric field $F(z)$ along the electron trajectory is calculated and then Fourier transformed. In this thesis, two geometries were considered: A planar flake and an infinitely extended cylinder (to model a nanowire or the shaft of a nanotip). Exemplary calculation results are presented in Fig. 5.1.

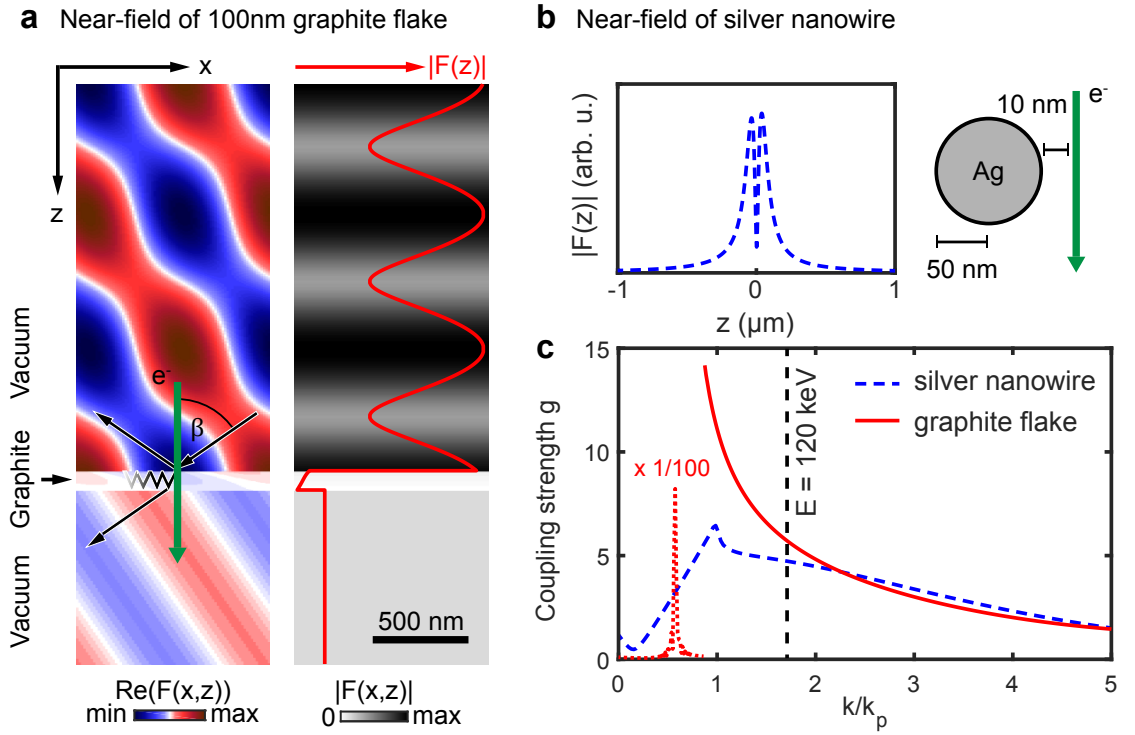

Figure 5.1: Analytic determination of coupling strength g for two different scenarios. **a** Scenario 1: Electric field F at 100 nm thick graphite flake illuminated with $\lambda = 800$ nm light at angle $\alpha = 55°$. Most of the intensity is reflected, but a fraction penetrates into the graphite flake. Red solid line in right panel: Absolute value of electric field along electron trajectory (green arrow in left panel). **b** Scenario 2: Electric field of a 50 nm thick silver nanowire along electron trajectory passing by at a distance of 10 nm for illumination parallel to the electron beam. **c** Fourier transform of $F(z)$ for both scenarios in units of photon momentum $\hbar k_p$. The coupling strength g is given by the Fourier component at $k = \omega/v = k_p c/v$. For the electron energy $E = 120$ keV, this corresponds to $k = 1.66\,k_p$ (indicated by vertical dashed line). Coupling strength calculated for electric field amplitude $E_0 = 0.1\,\mathrm{V\,nm^{-1}}$.

Figure 5.1**a** displays the electric field of a graphite flake (thickness 100 nm) in vacuum, oriented such that its surface normal is parallel to the electron beam, and illuminated at an angle $\beta = 55°$. The overall field strength along the electron trajectory is obtained using a transfer matrix formalism for multilayer reflections at oblique incidence as described in Chap. 7 and 8 of Ref. [225]. The near-field of an infinite silver cylinder is calculated according to Mie theory using the MATLAB package *MatScat* by Jan Schäfer.[1] For both sample geometries, the Fourier transform shown in Fig. 5.1**c** exhibits significant coupling strengths g at $k = 1.66\omega/c$. For a fixed sample geometry, g can further be tuned by sample tilt, which changes both the electron trajectory and the near-field distribution, by using a material with a different refractive index or by changing the electron energy. For instance, the coupling to electrons at 200 keV ($k = 1.44\,k_p$) is stronger than at 120 keV.

5.3 Energy Shift Analysis for an Estimation of the Electron Pulse Train's Peak Duration

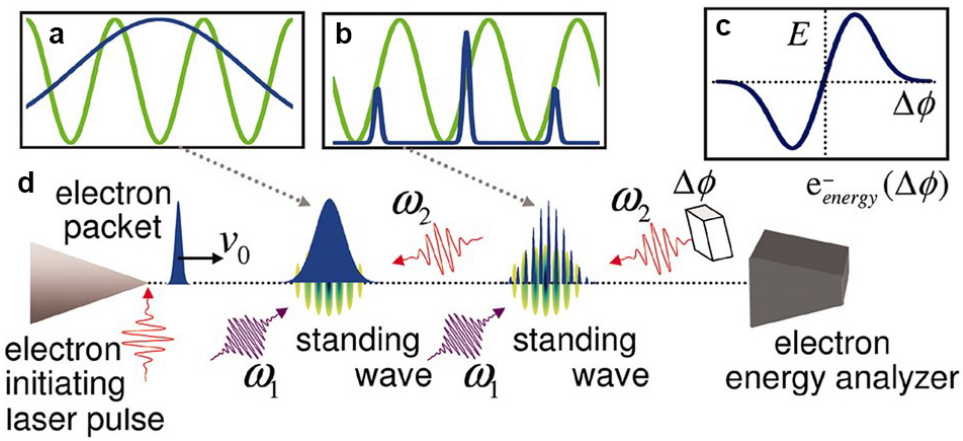

Figure 5.2: Scheme for the generation and characterisation of attosecond electron pulse trains by a moving intensity grating. **a** Spatial profile of intensity grating (green) and electron pulse (blue). **b** Same as in (**a**), but at position of temporal focus. **c** Average electron energy as a function of the relative phase between the two intensity gratings. **d** Experimental scheme. Reprinted with permission from Ref. [149].

Ponderomotive scattering is not only an alternative for the generation, but also for the characterisation of the electron pulse trains, as illustrated in Fig. 5.2. The electron pulse interacts with an identical second intensity grating at the temporal focus position and energy spectra are recorded for varying relative phases between both gratings. Shifting the

[1] http://de.mathworks.com/matlabcentral/fileexchange/36831-matscat

phase of one of the light fields that generate the second intensity grating shifts its position with respect to the pulse train, so that, depending on the phase, the electron peaks are positioned at either rising or falling slopes of the grating and thus experience an accelerating or decelerating force. Figure 5.2**c** displays the corresponding shift of the average electron energy. The strength of this phase-dependent energy shift is a direct measure of the peak duration of the pulse train, since the de- and accelerating contributions are less strongly averaged for shorter peaks.

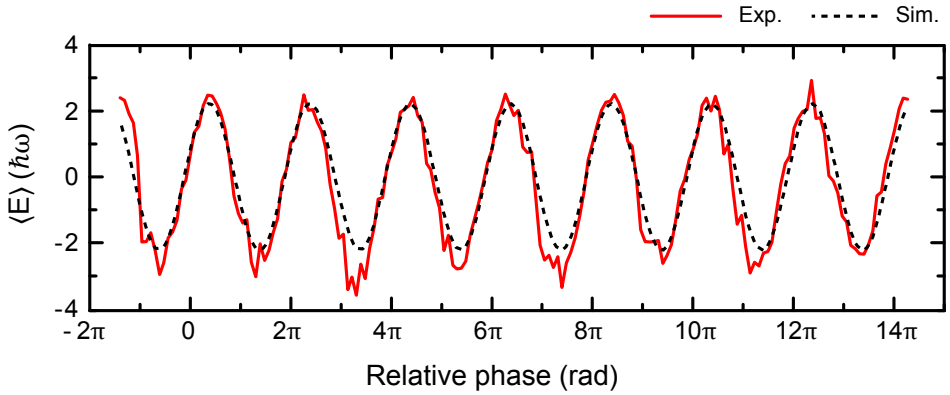

Figure 5.3: Characterisation of attosecond pulse train by analysis of average electron energy $\langle E \rangle$. The phase-dependent energy shift of the experimental data presented in Fig. 3.4 (red solid line) and the corresponding simulation presented in Fig. 3.10 (black dashed line) are in good agreement. Data courtesy of Christopher Rathje.

The attosecond pulse train spectrograms from the present work can clearly also be analysed in this way. As shown in Fig. 5.3, the average energy oscillates with the relative phase as expected. The analysis is much simpler than performing a SQUIRRELS reconstruction, and it is possible to roughly estimate the pulse duration by comparison with numerical simulations, however, this is done rather indirectly and requires assumptions for the modelling of the interaction, including experimental uncertainties. A *quantitative* characterisation facilitated by SQUIRRELS is advantageous, as it directly yields the temporal electron envelope and is generally much more powerful. SQUIRRELS in its present form is tailored to the single-photon single-electron interaction discussed in this work. The longitudinal Kapitza-Dirac effect is different, in that two photons instead of one are involved in each scattering process. SQUIRRELS should however be adaptable by replacing the unitary operator in the algorithm by one describing the Kapitza-Dirac interaction. A quantum state reconstruction and thereby a characterisation of the attosecond electron pulse train should then be possible under the following two conditions: The

initial electron energy width must be smaller than the photon energy, so that a coherent superposition of sidebands is formed (cf. Sec. 5.4), and the spectrogram must be recorded in a sideband-resolved manner.

5.4 Longitudinal Electron Coherence

Figure 5.4 illustrates that the occurrence of sidebands in the energy spectrum requires electron coherence times exceeding the optical period: Quantum interference between subsequent cycles gives rise to sidebands (Fig. 5.4**a**). For coherence times decreasing below the optical period $T = 2.66\,\mathrm{fs}$, the electrons behave more like classical point particles, and their energy follows the laser vector potential (Fig. 5.4**b**,**c**). Isolated attosecond electron pulses will produce spectrograms as shown in Fig. 5.4**c** that do not exhibit sidebands, but resemble attosecond streaking spectra obtained by photoionisation of atoms [226].

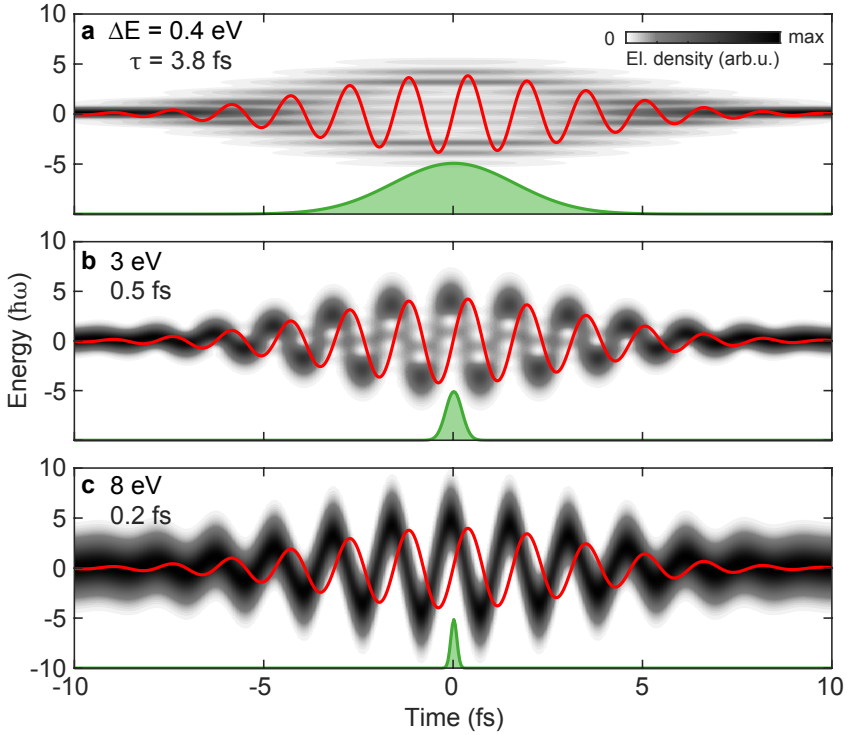

Figure 5.4: Influence of electron temporal coherence on electron-photon cross-correlation (see text). Red solid line: Electric field. Green shaded area: Electron envelope. Calculations for coherent electron wavepackets with energy width ΔE (FWHM) and corresponding coherence time τ as indicated in the figures.

Bibliography

[1] Krausz, F. and Ivanov, M. Attosecond physics. *Reviews of Modern Physics*, 81(1): 163–234, 2009. Cited on p.

[2] McPherson, A., Gibson, G., Jara, H., Johann, U., Luk, T. S., McIntyre, I. A., Boyer, K., and Rhodes, C. K. Studies of multiphoton production of vacuum-ultraviolet radiation in the rare gases. *Journal of the Optical Society of America B*, 4(4):595, 1987. Cited on p.

[3] Corkum. Plasma perspective on strong field multiphoton ionization. *Physical Review Letters*, 71(13):1994–1997, 1993. Cited on p.

[4] Beeby, A. Pump-Probe Laser Spectroscopy. In Andrews, D. L. and Demidov, A. A., editors, *An Introduction to Laser Spectroscopy*, pages 105–137. Springer US, Boston, MA, 2002. ISBN 978-1-4613-5213-6. Cited on p.

[5] Weiner, A. M. Femtosecond pulse shaping using spatial light modulators. *Review of Scientific Instruments*, 71(5):1929–1960, 2000. Cited on p.

[6] Allen, L., Beijersbergen, M. W., Spreeuw, R. J. C., and Woerdman, J. P. Orbital angular momentum of light and the transformation of Laguerre-Gaussian laser modes. *Physical Review A*, 45(11):8185–8189, 1992. Cited on p.

[7] Gustafsson, M. G. L. Surpassing the lateral resolution limit by a factor of two using structured illumination microscopy. *Journal of Microscopy*, 198(2):82–87, 2000. Cited on p.

[8] Hell, S. W. and Wichmann, J. Breaking the diffraction resolution limit by stimulated emission: Stimulated-emission-depletion fluorescence microscopy. *Optics Letters*, 19(11):780, 1994. Cited on p.

[9] Pohl, D. W., Denk, W., and Lanz, M. Optical stethoscopy: Image recording with resolution l/20. *Applied Physics Letters*, 44(7):651–653, 1984. Cited on p.

[10] Zewail, A. H. Four-dimensional electron microscopy. *Science*, 328(5975):187–193, 2010. Cited on p.

[11] van Oudheusden, T., de Jong, E. F., van der Geer, S. B., 't Root, W. P. E. M. O., Luiten, O. J., and Siwick, B. J. Electron source concept for single-shot sub-100 fs electron diffraction in the 100 keV range. *Journal of Applied Physics*, 102(9): 093501, 2007. Cited on p.

[12] Gliserin, A., Walbran, M., Krausz, F., and Baum, P. Sub-phonon-period compression of electron pulses for atomic diffraction. *Nature Communications*, 6:8723, 2015. Cited on p.

[13] Maxson, J., Cesar, D., Calmasini, G., Ody, A., Musumeci, P., and Alesini, D. Direct Measurement of Sub-10 fs Relativistic Electron Beams with Ultralow Emittance. *Physical Review Letters*, 118(15):154802, 2017. Cited on p.

[14] Williams, J., Zhou, F., Sun, T., Tao, Z., Chang, K., Makino, K., Berz, M., Duxbury, P. M., and Ruan, C.-Y. Active control of bright electron beams with RF optics for femtosecond microscopy. *Structural Dynamics*, 4(4):044035, 2017. Cited on p.

[15] Kealhofer, C., Schneider, W., Dominik Ehberger, Ryabov, A., Krausz, F., and Baum, P. All-optical control and metrology of electron pulses. *Science*, 352:429–433, 2016. Cited on p.

[16] Niikura, H., Légaré, F., Hasbani, R., Bandrauk, A. D., Ivanov, M. Y., Villeneuve, D. M., and Corkum, P. B. Sub-laser-cycle electron pulses for probing molecular dynamics. *Nature*, 417(6892):917–922, 2002. Cited on p.

[17] Blaga, C. I., Xu, J., DiChiara, A. D., Sistrunk, E., Zhang, K., Agostini, P., Miller, T. A., DiMauro, L. F., and Lin, C. D. Imaging ultrafast molecular dynamics with laser-induced electron diffraction. *Nature*, 483(7388):194–197, 2012. Cited on p.

[18] Bouwmeester, D., Pan, J.-W., Mattle, K., Eibl, M., Weinfurter, H., and Zeilinger, A. Experimental quantum teleportation. *Nature*, 390(6660):575–579, 1997. Cited on p.

[19] Freedman, S. J. and Clauser, J. F. Experimental Test of Local Hidden-Variable Theories. *Physical Review Letters*, 28(14):938–941, 1972. Cited on p.

[20] Aspect, A., Grangier, P., and Roger, G. Experimental Tests of Realistic Local Theories via Bell's Theorem. *Physical Review Letters*, 47(7):460–463, 1981. Cited on p.

[21] O'Brien, J. L., Furusawa, A., and Vučković, J. Photonic quantum technologies. *Nature Photonics*, 3(12):687–695, 2009. Cited on p.

[22] Baron, M., Rauch, H., and Suda, M. First attempt of neutron quantum state reconstruction. *Journal of Optics B: Quantum and Semiclassical Optics*, 5(3):S241–S244, 2003. Cited on p.

[23] Bocquillon, E., Parmentier, F. D., Grenier, C., Berroir, J.-M., Degiovanni, P., Glattli, D. C., Placais, B., Cavanna, A., Jin, Y., and Feve, G. Electron quantum optics: partitioning electrons one by one. *Physical Review Letters*, 108(19):196803, 2012. Cited on p.

[24] Jones, E., Becker, M., Luiten, J., and Batelaan, H. Laser control of electron matter waves. *Laser & Photonics Reviews*, 10(2):214–229, 2016. Cited on p.

[25] Kapitza, P. L. and Dirac, P. A. M. The reflection of electrons from standing light waves. *Mathematical Proceedings of the Cambridge Philosophical Society*, 29(2): 297–300, 1933. Cited on p.

[26] Freimund, D. L., Aflatooni, K., and Batelaan, H. Observation of the Kapitza-Dirac effect. *Nature*, 413(6852):142–143, 2001. Cited on p.

[27] Barwick, B., Flannigan, D. J., and Zewail, A. H. Photon-induced near-field electron microscopy. *Nature*, 462(7275):902–906, 2009. Cited on p.

[28] Feist, A., Echternkamp, K. E., Schauss, J., Yalunin, S. V., Schäfer, S., and Ropers, C. Quantum coherent optical phase modulation in an ultrafast transmission electron microscope. *Nature*, 521(7551):200–203, 2015. Cited on p.

[29] Piestrup, M. A., Rothbart, G. B., Fleming, R. N., and Pantell, R. H. Momentum modulation of a free electron beam with a laser. *Journal of Applied Physics*, 46(1): 132–137, 1975. Cited on p.

[30] Mizuno, K., Pae, J., Nozokido, T., and Furuya, K. Experimental evidence of the inverse Smith–Purcell effect. *Nature*, 328(6125):45–47, 1987. Cited on p.

[31] Park, S. T., Lin, M., and Zewail, A. H. Photon-induced near-field electron microscopy (PINEM): theoretical and experimental. *New Journal of Physics*, 12(12): 123028, 2010. Cited on p.

[32] Piazza, L., Lummen, T T A, Quiñonez, E., Murooka, Y., Reed, B. W., Barwick, B., and Carbone, F. Simultaneous observation of the quantization and the interference pattern of a plasmonic near-field. *Nature Communications*, 6:6407, 2015. Cited on p.

[33] Park, S. T. and Zewail, A. H. Relativistic effects in photon-induced near field electron microscopy. *The Journal of Physical Chemistry A*, 116(46):11128–11133, 2012. Cited on p.

[34] Cesarano, C. and Assante, D. A note on Generalized Bessel Functions. *International Journal of Mathematical Models and Methods in Applied Sciences*, 7(6): 625–629, 2013. Cited on p.

[35] Talebi, N. Schrödinger electrons interacting with optical gratings: Quantum mechanical study of the inverse Smith–Purcell effect. *New Journal of Physics*, 18(12): 123006, 2016. Cited on p.

[36] Rabi, I. I. Space Quantization in a Gyrating Magnetic Field. *Physical Review*, 51 (8):652–654, 1937. Cited on p.

[37] Eberly, J. H., Shore, B. W., Bialynicka-Birula, Z., and Bialynicki-Birula, I. Coherent dynamics of N-level atoms and molecules. I. Numerical experiments. *Physical Review A*, 16(5):2038–2047, 1977. Cited on p.

[38] Bialynicka-Birula, Z., Bialynicki-Birula, I., Eberly, J. H., and Shore, B. W. Coherent dynamics of N-level atoms and molecules. II. Analytic solutions. *Physical Review A*, 16(5):2048–2054, 1977. Cited on p.

[39] Shore, B. W. and Eberly, J. H. Analytic approximations in multi-level excitation theory. *Optics Communications*, 24(1):83–88, 1978. Cited on p.

[40] Yurtsever, A. and Zewail, A. H. Direct visualization of near-fields in nanoplasmonics and nanophotonics. *Nano Letters*, 12(6):3334–3338, 2012. Cited on p.

[41] Jeanguillaume, C. and Colliex, C. Spectrum-image: The next step in EELS digital acquisition and processing. *Ultramicroscopy*, 28(1-4):252–257, 1989. Cited on p.

[42] Lavergne, J.-L., Martin, J.-M., and Belin, M. Interactive electron energy-loss elemental mapping by the Imaging-Spectrum method. *Microscopy Microanalysis Microstructures*, 3(6):517–528, 1992. Cited on p.

[43] Nelayah, J., Kociak, M., Stéphan, O., García de Abajo, F. Javier, Tencé, M., Henrard, L., Taverna, D., Pastoriza-Santos, I., Liz-Marzán, L. M., and Colliex, C. Mapping surface plasmons on a single metallic nanoparticle. *Nature Physics*, 3 (5):348–353, 2007. Cited on p.

[44] Park, S. T., Kwon, O.-H., and Zewail, A. H. Chirped imaging pulses in four-dimensional electron microscopy: femtosecond pulsed hole burning. *New Journal of Physics*, 14:053046, 2012. Cited on p.

[45] Plemmons, D. A., Tae Park, S., Zewail, A. H., and Flannigan, D. J. Characterization of fast photoelectron packets in weak and strong laser fields in ultrafast electron microscopy. *Ultramicroscopy*, 2014. Cited on p.

[46] Kirchner, F. O., Gliserin, A., Krausz, F., and Baum, P. Laser streaking of free electrons at 25 keV. *Nature Photonics*, 8(1):52–57, 2013. Cited on p.

[47] Paris, M. and Řeháček, J., editors. *Quantum state estimation*, volume 649 of *Lecture Notes in Physics*. Springer, Berlin and New York, 2004. ISBN 978-3-540-22329-0. Cited on p.

[48] Heisenberg, W. Über den anschaulichen Inhalt der quantentheoretischen Kinematik und Mechanik. *Zeitschrift für Physik*, 43(3-4):172–198, 1927. Cited on p.

[49] Wootters, W. K. and Zurek, W. H. A single quantum cannot be cloned. *Nature*, 299(5886):802–803, 1982. Cited on p.

[50] von Neumann, J. and Beyer, R. T. *Mathematical foundations of quantum mechanics*. Princeton landmarks in mathematics and physics. Princeton University Press, Princeton, N.J., 1996. ISBN 9780691080031. Cited on p.

[51] Schleich, W. P. *Quantum Optics in Phase Space*. Wiley-VCH, 2015. ISBN 352780255X. Cited on p.

[52] Thew, R. T., Nemoto, K., White, A. G., and Munro, W. J. Qudit quantum-state tomography. *Physical Review A*, 66(1), 2002. Cited on p.

[53] Wigner, E. On the Quantum Correction For Thermodynamic Equilibrium. *Physical Review*, 40(5):749–759, 1932. Cited on p.

[54] Nogues, G., Rauschenbeutel, A., Osnaghi, S., Bertet, P., Brune, M., Raimond, J. M., Haroche, S., Lutterbach, L. G., and Davidovich, L. Measurement of a negative value for the Wigner function of radiation. *Physical Review A*, 62(5):054101, 2000. Cited on p.

[55] Vogel, K. and Risken, H. Determination of quasiprobability distributions in terms of probability distributions for the rotated quadrature phase. *Physical Review A*, 40 (5):2847–2849, 1989. Cited on p.

[56] Smithey, D. T., Beck, M., and Raymer, M. G. Measurement of the Wigner Distribution and the Density Matrix of a Light Mode Using Optical Homodyne Tomography: Application to Squeezed States and the Vacuum. *Physical Review Letters*, 70(9):1244–1247, 1993. Cited on p.

[57] Lvovsky, A. I. and Raymer, M. G. Continuous-variable optical quantum-state tomography. *Reviews of Modern Physics*, 81(1):299–332, 2009. Cited on p.

[58] Weyl, H. Quantenmechanik und Gruppentheorie. *Zeitschrift für Physik*, 46(1): 1–46, 1927. Cited on p.

[59] Case, W. B. Wigner functions and Weyl transforms for pedestrians. *American Journal of Physics*, 76(10):937–946, 2008. Cited on p.

[60] Janicke, U. and Wilkens, M. Tomography of Atom Beams. *Journal of Modern Optics*, 42(11):2183–2199, 1995. Cited on p.

[61] Kurtsiefer, C., Pfau, T., and Mlynek, J. Measurement of the Wigner function of an ensemble of helium atoms. *Nature*, 386(13):150–153, 1997. Cited on p.

[62] Dunn, T. J., Walmsley, I. A., and Mukamel, S. Experimental determination of the quantum-mechanical state of a molecular vibrational mode using fluorescence tomography. *Physical Review Letters*, 74(6):884–887, 1995. Cited on p.

[63] Leibfried, D., Meekhof, D. M., King, B. E., Monroe, C., Itano, W. M., and Wineland, D. J. Experimental Determination of the Motional Quantum State of a Trapped Atom. *Physical Review Letters*, 77(21):4281–4285, 1996. Cited on p.

[64] Grenier, C., Hervé, R., Bocquillon, E., Parmentier, F. D., Plaçais, B., Berroir, J. M., Fève, G., and Degiovanni, P. Single-electron quantum tomography in quantum Hall edge channels. *New Journal of Physics*, 13(9):093007, 2011. Cited on p.

[65] Jullien, T., Roulleau, P., Roche, B., Cavanna, A., Jin, Y., and Glattli, D. C. Quantum tomography of an electron. *Nature*, 514(7524):603–607, 2014. Cited on p.

[66] Chuang, I. L. and Nielsen, M. A. Prescription for experimental determination of the dynamics of a quantum black box. *Journal of Modern Optics*, 44(11-12):2455–2467, 1997. Cited on p.

[67] Mukamel, S. Multidimensional femtosecond correlation spectroscopies of electronic and vibrational excitations. *Annual Review of Physical Chemistry*, 51:691–729, 2000. Cited on p.

[68] Bressler, C. and Chergui, M. Ultrafast X-ray absorption spectroscopy. *Chemical Reviews*, 104(4):1781–1812, 2004. Cited on p.

[69] Miller, R. J. D. Femtosecond crystallography with ultrabright electrons and x-rays: capturing chemistry in action. *Science*, 343(6175):1108–1116, 2014. Cited on p.

[70] Gulde, M., Schweda, S., Storeck, G., Maiti, M., Yu, H. K., Wodtke, A. M., Schäfer, S., and Ropers, C. Ultrafast low-energy electron diffraction in transmission resolves polymer/graphene superstructure dynamics. *Science*, 345(6193):200–204, 2014. Cited on p.

[71] Bostanjoglo, O. Time-resolved TEM of pulsed crystallization of amorphous Si and Ge films. *physica status solidi (a)*, 70(2):473–481, 1982. Cited on p.

[72] Barwick, B., Park, H. S., Kwon, O.-H., Baskin, J. S., and Zewail, A. H. 4D Imaging of Transient Structures and Morphologies in Ultrafast Electron Microscopy. *Science*, 322(5905):1227–1231, 2008. Cited on p.

[73] Browning, N. D., Bonds, M. A., Campbell, G. H., Evans, J. E., LaGrange, T., Jungjohann, K. L., Masiel, D. J., McKeown, J., Mehraeen, S., Reed, B. W., and Santala, M. Recent developments in dynamic transmission electron microscopy. *Current Opinion in Solid State and Materials Science*, 16(1):23–30, 2012. Cited on p.

[74] Piazza, L., Masiel, D. J., LaGrange, T., Reed, B. W., Barwick, B., and Carbone, F. Design and implementation of a fs-resolved transmission electron microscope based on thermionic gun technology. *Chemical Physics*, 423:79–84, 2013. Cited on p.

[75] Kieft, E., Schliep, K. B., Suri, P. K., and Flannigan, D. J. Communication: Effects of thermionic-gun parameters on operating modes in ultrafast electron microscopy. *Structural Dynamics*, 2(5):051101, 2015. Cited on p.

[76] Cao, G., Sun, S., Li, Z., Tian, H., Yang, H., and Li, J. Clocking the anisotropic lattice dynamics of multi-walled carbon nanotubes by four-dimensional ultrafast transmission electron microscopy. *Scientific Reports*, 5:8404, 2015. Cited on p.

[77] Bücker, K., Picher, M., Crégut, O., LaGrange, T., Reed, B. W., Park, S. T., Masiel, D. J., and Banhart, F. Electron Beam Dynamics in an Ultrafast Transmission Electron Microscope with Wehnelt Electrode. *Ultramicroscopy*, 2016. Cited on p.

[78] Kuwahara, M., Nambo, Y., Aoki, K., Sameshima, K., Jin, X., Ujihara, T., Asano, H., Saitoh, K., Takeda, Y., and Tanaka, N. The Boersch effect in a picosecond pulsed electron beam emitted from a semiconductor photocathode. *Applied Physics Letters*, 109(1):013108, 2016. Cited on p.

[79] LaGrange, T., Armstrong, M. R., Boyden, K., Brown, C. G., Campbell, G. H., Colvin, J. D., DeHope, W. J., Frank, A. M., Gibson, D. J., Hartemann, F. V., Kim, J. S., King, W. E., Pyke, B. J., Reed, B. W., Shirk, M. D., Shuttlesworth, R. M., Stuart, B. C., Torralva, B. R., and Browning, N. D. Single-shot dynamic transmis-

sion electron microscopy. *Applied Physics Letters*, 89(4):044105, 2006. Cited on p.

[80] LaGrange, T., Reed, B. W., and Masiel, D. J. Movie-mode dynamic electron microscopy. *MRS Bulletin*, 40(01):22–28, 2015. Cited on p.

[81] Lummen, T. T. A., Lamb, R. J., Berruto, G., LaGrange, T., Dal Negro, L., Garcia de Abajo, F Javier, McGrouther, D., Barwick, B., and Carbone, F. Imaging and controlling plasmonic interference fields at buried interfaces. *Nature Communications*, 7:13156, 2016. Cited on p.

[82] Sun, S., Wei, L., Li, Z., Cao, G., Liu, Y., Lu, W. J., Sun, Y. P., Tian, H., Yang, H., and Li, J. Direct observation of an optically induced charge density wave transition in 1T−TaSe2. *Physical Review B*, 92(22), 2015. Cited on p.

[83] Feist, A., Bach, N., Rubiano da Silva, N., Danz, T., Moller, M., Priebe, K. E., Domrose, T., Gatzmann, J. G., Rost, S., Schauss, J., Strauch, S., Bormann, R., Sivis, M., Schafer, S., and Ropers, C. Ultrafast transmission electron microscopy using a laser-driven field emitter: Femtosecond resolution with a high coherence electron beam. *Ultramicroscopy*, 176:63–73, 2017. Cited on p.

[84] Hell, S. W. Nobel Lecture: Nanoscopy with Focused Light, 2014. Cited on p.

[85] Udem, T., Holzwarth, R., and Hänsch, T. W. Optical frequency metrology. *Nature*, 416(6877):233–237, 2002. Cited on p.

[86] Hentschel, M., Kienberger, R., Spielmann, C., Reider, G. A., Milosevic, N., Brabec, T., Corkum, P., Heinzmann, U., Drescher, M., and Krausz, F. Attosecond metrology. *Nature*, 414(6863):509–513, 2001. Cited on p.

[87] McMorran, B. J., Agrawal, A., Anderson, I. M., Herzing, A. A., Lezec, H. J., McClelland, J. J., and Unguris, J. Electron vortex beams with high quanta of orbital angular momentum. *Science*, 331(6014):192–195, 2011. Cited on p.

[88] Handali, J., Shakya, P., and Barwick, B. Creating electron vortex beams with light. *Optics Express*, 23(4):5236–5243, 2015. Cited on p.

[89] England, R. J., Noble, R. J., Bane, K., Dowell, D. H., Ng, C.-K., Spencer, J. E., Tantawi, S., Wu, Z., Byer, R. L., Peralta, E., Soong, K., Chang, C.-M., Montazeri, B., Wolf, S. J., Cowan, B., Dawson, J., Gai, W., Hommelhoff, P., Huang, Y.-C., Jing, C., McGuinness, C., Palmer, R. B., Naranjo, B., Rosenzweig, J., Travish, G., Mizrahi, A., Schachter, L., Sears, C., Werner, G. R., and Yoder, R. B. Dielectric laser accelerators. *Reviews of Modern Physics*, 86(4):1337–1389, 2014. Cited on p.

[90] Hommelhoff, P., Sortais, Y., Aghajani-Talesh, A., and Kasevich, M. A. Field emission tip as a nanometer source of free electron femtosecond pulses. *Physical Review Letters*, 96(7):077401, 2006. Cited on p.

[91] Ehberger, D., Hammer, J., Eisele, M., Krüger, M., Noe, J., Högele, A., and Hommelhoff, P. Highly Coherent Electron Beam from a Laser-Triggered Tungsten Needle Tip. *Physical Review Letters*, 114(22):227601, 2015. Cited on p.

[92] Baum, P. and Zewail, A. Femtosecond diffraction with chirped electron pulses. *Chemical Physics Letters*, 462(1-3):14–17, 2008. Cited on p.

[93] Park, S. T. and Zewail, A. H. Enhancing image contrast and slicing electron pulses in 4D near field electron microscopy. *Chemical Physics Letters*, 521:1–6, 2012. Cited on p.

[94] Eichberger, M., Erasmus, N., Haupt, K., Kassier, G., von Flotow, A., Demsar, J., and Schwoerer, H. Femtosecond streaking of electron diffraction patterns to study structural dynamics in crystalline matter. *Applied Physics Letters*, 102(12):121106, 2013. Cited on p.

[95] Scoby, C. M., Li, R. K., Threlkeld, E., To, H., and Musumeci, P. Single-shot 35 fs temporal resolution electron shadowgraphy. *Applied Physics Letters*, 102(2): 023506, 2013. Cited on p.

[96] Siwick, B. J., Dwyer, J. R., Jordan, R. E., and Miller, R. J. D. An atomic-level view of melting using femtosecond electron diffraction. *Science*, 302(5649):1382–1385, 2003. Cited on p.

[97] Storeck, G., Vogelgesang, S., Sivis, M., Schäfer, S., and Ropers, C. Nanotip-based photoelectron microgun for ultrafast LEED. *Structural Dynamics*, 4(4):044024, 2017. Cited on p.

[98] Gliserin, A., Apolonski, A., Krausz, F., and Baum, P. Compression of single-electron pulses with a microwave cavity. *New Journal of Physics*, 14(7):073055, 2012. Cited on p.

[99] Curry, E., Fabbri, S., Musumeci, P., and Gover, A. THz-driven zero-slippage IFEL scheme for phase space manipulation. *New Journal of Physics*, 18(11):113045, 2016. Cited on p.

[100] Serafini, L. and Ferrario, M. Velocity Bunching in Photo-Injectors. In Chattopadhyay, S., editor, *Physics of, and science with, the X-ray free-electron laser*, AIP conference proceedings, pages 87–106. American Institute of Physics, Melville, N.Y., 2001. ISBN 9780735400221. Cited on p.

[101] Schulz, S., Grguraš, I., Behrens, C., Bromberger, H., Costello, J. T., Czwalinna, M. K., Felber, M., Hoffmann, M. C., Ilchen, M., Liu, H. Y., Mazza, T., Meyer, M., Pfeiffer, S., Prędki, P., Schefer, S., Schmidt, C., Wegner, U., Schlarb, H., and Cavalieri, A. L. Femtosecond all-optical synchronization of an X-ray free-electron laser. *Nature Communications*, 6:5938, 2015. Cited on p.

[102] Wimmer, L., Herink, G., Solli, D. R., Yalunin, S. V., Echternkamp, K. E., and Ropers, C. Terahertz control of nanotip photoemission. *Nature Physics*, 10(6): 432–436, 2014. Cited on p.

[103] Baum, P. and Krausz, F. Capturing atomic-scale carrier dynamics with electrons. *Chemical Physics Letters*, 683:57–61, 2017. Cited on p.

[104] Talbot, H. F. LXXVI. Facts relating to optical science. No. IV. *Philosophical Magazine Series 3*, 9(56):401–407, 1836. Cited on p.

[105] Patorski, K. I The Self-Imaging Phenomenon and its Applications. In Wolf, E., editor, *Progress in Optics*, volume 27 of *Progress in Optics*, pages 1–108. North-Holland, Amsterdam, 1989. ISBN 9780444874252. Cited on p.

[106] Feynman, R. P. Space-Time Approach to Non-Relativistic Quantum Mechanics. *Reviews of Modern Physics*, 20(2):367–387, 1948. Cited on p.

[107] Hasselbach, F. Progress in electron- and ion-interferometry. *Reports on Progress in Physics*, 73(1):016101, 2010. Cited on p.

[108] Schmidt-Rohr, K. *Multidimensional Solid-State NMR and Polymers*. Elsevier Science, Burlington, 2012. ISBN 9780126266306. Cited on p.

[109] Bordé, C. Atomic interferometry with internal state labelling. *Physics Letters A*, 140(1-2):10–12, 1989. Cited on p.

[110] Mukamel, S. *Principles of nonlinear optical spectroscopy*. Oxford University Press, Oxford, 1999. ISBN 9780195092783. Cited on p.

[111] Ramsey, N. F. Experiments with separated oscillatory fields and hydrogen masers. *Reviews of Modern Physics*, 62(3):541–552, 1990. Cited on p.

[112] Itatani, J., Levesque, J., Zeidler, D., Niikura, H., Pépin, H., Kieffer, J. C., Corkum, P. B., and Villeneuve, D. M. Tomographic imaging of molecular orbitals. *Nature*, 432:867–871, 2004. Cited on p.

[113] Haessler, S., Caillat, J., Boutu, W., Giovanetti-Teixeira, C., Ruchon, T., Auguste, T., Diveki, Z., Breger, P., Maquet, A., Carré, B., Taïeb, R., and Salières, P. Attosecond imaging of molecular electronic wavepackets. *Nature Physics*, 6(3):200–206, 2010. Cited on p.

[114] Xie, X., Roither, S., Kartashov, D., Persson, E., Arbó, D. G., Zhang, L., Gräfe, S., Schöffler, M. S., Burgdörfer, J., Baltuška, A., and Kitzler, M. Attosecond probe of valence-electron wave packets by subcycle sculpted laser fields. *Physical Review Letters*, 108(19):193004, 2012. Cited on p.

[115] Weingartshofer, A., Holmes, J. K., Caudle, G., Clarke, E. M., and Krüger, H. Direct Observation of Multiphoton Processes in Laser-Induced Free-Free Transitions. *Physical Review Letters*, 39(5):269–270, 1977. Cited on p.

[116] Agostini, P., Fabre, F., Mainfray, G., Petite, G., and Rahman, N. Free-Free Transitions Following Six-Photon Ionization of Xenon Atoms. *Physical Review Letters*, 42(17):1127–1130, 1979. Cited on p.

[117] Radcliffe, P., Arbeiter, M., Li, W. B., Düsterer, S., Redlin, H., Hayden, P., Hough, P., Richardson, V., Costello, J. T., Fennel, T., and Meyer, M. Atomic photoionization in combined intense XUV free-electron and infrared laser fields. *New Journal of Physics*, 14(4):043008, 2012. Cited on p.

[118] Meyer, M., Radcliffe, P., Tschentscher, T., Costello, J. T., Cavalieri, A. L., Grguras, I., Maier, A. R., Kienberger, R., Bozek, J., Bostedt, C., Schorb, S., Coffee, R., Messerschmidt, M., Roedig, C., Sistrunk, E., Di Mauro, L. F., Doumy, G., Ueda, K., Wada, S., Düsterer, S., Kazansky, A. K., and Kabachnik, N. M. Angle-Resolved Electron Spectroscopy of Laser-Assisted Auger Decay Induced by a Few-Femtosecond X-Ray Pulse. *Physical Review Letters*, 108(6), 2012. Cited on p.

[119] Morimoto, Y., Kanya, R., and Yamanouchi, K. Light-Dressing Effect in Laser-Assisted Elastic Electron Scattering by Xe. *Physical Review Letters*, 115(12): 123201, 2015. Cited on p.

[120] Ogawa, S., Nagano, H., Petek, H., and Heberle, A. P. Optical Dephasing in Cu(111) Measured by Interferometric Two-Photon Time-Resolved Photoemission. *Physical Review Letters*, 78(7):1339–1342, 1997. Cited on p.

[121] Petek, H., Heberle, A. P., Nessler, W., Nagano, H., Kubota, S., Matsunami, S., Moriya, N., and Ogawa, S. Optical Phase Control of Coherent Electron Dynamics in Metals. *Physical Review Letters*, 79(23):4649–4652, 1997. Cited on p.

[122] Saathoff, G., Miaja-Avila, L., Aeschlimann, M., Murnane, M. M., and Kapteyn, H. C. Laser-assisted photoemission from surfaces. *Physical Review A*, 77(2), 2008. Cited on p.

[123] Mahmood, F., Chan, C.-K., Alpichshev, Z., Gardner, D., Lee, Y., Lee, P. A., and Gedik, N. Selective scattering between Floquet–Bloch and Volkov states in a topological insulator. *Nature Physics*, 12(4):306–310, 2016. Cited on p.

[124] García de Abajo, F. J., Asenjo-Garcia, A., and Kociak, M. Multiphoton absorption and emission by interaction of swift electrons with evanescent light fields. *Nano Letters*, 10(5):1859–1863, 2010. Cited on p.

[125] García de Abajo, F. J. and Kociak, M. Electron energy-gain spectroscopy. *New Journal of Physics*, 10(7):073035, 2008. Cited on p.

[126] Yurtsever, A., van der Veen, Renske M, and Zewail, A. H. Subparticle ultrafast spectrum imaging in 4D electron microscopy. *Science*, 335(6064):59–64, 2012. Cited on p.

[127] Kozák, M., McNeur, J., Leedle, K. J., Schönenberger, N., Ruehl, A., Hartl, I., Harris, J. S., Byer, R. L., and Hommelhoff, P. Optical gating and streaking of free-electrons with attosecond precision. *arXiv:1512.04394*, 2015. Cited on p.

[128] Saleh, B. E. A. and Teich, M. C. *Fundamentals of photonics*. Wiley series in pure and applied optics. Wiley, 2nd edition, 2013. ISBN 9780471358329. Cited on p.

[129] Batelaan, H. Colloquium: Illuminating the Kapitza-Dirac effect with electron matter optics. *Reviews of Modern Physics*, 79(3):929–941, 2007. Cited on p.

[130] García de Abajo, F. J., Barwick, B., and Carbone, F. Electron diffraction by plasmon waves. *Physical Review B*, 94(4):451, 2016. Cited on p.

[131] Asenjo-Garcia, A. and Abajo, F. J. García de. Dichroism in the Interaction between Vortex Electron Beams, Plasmons, and Molecules. *Physical Review Letters*, 113 (6):066102, 2014. Cited on p.

[132] Kira, M., Koch, S. W., Smith, R. P., Hunter, A. E., and Cundiff, S. T. Quantum spectroscopy with Schrödinger-cat states. *Nature Physics*, 7(10):799–804, 2011. Cited on p.

[133] Guzzinati, G., Beche, A., Lourenco-Martins, H., Martin, J., Kociak, M., and Verbeeck, J. Probing the symmetry of the potential of localized surface plasmon resonances with phase-shaped electron beams. *Nature Communications*, 8:14999, 2017. Cited on p.

[134] Verbeeck, J., Tian, H., and Schattschneider, P. Production and application of electron vortex beams. *Nature*, 467(7313):301–304, 2010. Cited on p.

[135] Echternkamp, K. E., Feist, A., Schäfer, S., and Ropers, C. Ramsey-type phase control of free-electron beams. *Nature Physics*, 12(11):1000–1004, 2016. Cited on p.

[136] Kruit, P., Hobbs, R. G., Kim, C.-S., Yang, Y., Manfrinato, V. R., Hammer, J., Thomas, S., Weber, P., Klopfer, B., Kohstall, C., Juffmann, T., Kasevich, M. A., Hommelhoff, P., and Berggren, K. K. Designs for a quantum electron microscope. *Ultramicroscopy*, 164:31–45, 2016. Cited on p.

[137] Wernet, P., Kunnus, K., Josefsson, I., Rajkovic, I., Quevedo, W., Beye, M., Schreck, S., Grübel, S., Scholz, M., Nordlund, D., Zhang, W., Hartsock, R. W., Schlotter, W. F., Turner, J. J., Kennedy, B., Hennies, F., de Groot, F M F, Gaffney, K. J., Techert, S., Odelius, M., and Föhlisch, A. Orbital-specific mapping of the ligand exchange dynamics of Fe(CO)5 in solution. *Nature*, 520(7545):78–81, 2015. Cited on p.

[138] Beaud, P., Caviezel, A., Mariager, S. O., Rettig, L., Ingold, G., Dornes, C., Huang, S.-W., Johnson, J. A., Radovic, M., Huber, T., Kubacka, T., Ferrer, A., Lemke, H. T., Chollet, M., Zhu, D., Glownia, J. M., Sikorski, M., Robert, A., Wadati, H., Nakamura, M., Kawasaki, M., Tokura, Y., Johnson, S. L., and Staub, U. A time-dependent order parameter for ultrafast photoinduced phase transitions. *Nature Materials*, 13(10):923–927, 2014. Cited on p.

[139] Grguraš, I., Maier, A. R., Behrens, C., Mazza, T., Kelly, T. J., Radcliffe, P., Düsterer, S., Kazansky, A. K., Kabachnik, N. M., Tschentscher, T., Costello, J. T., Meyer, M., Hoffmann, M. C., Schlarb, H., and Cavalieri, A. L. Ultrafast X-ray pulse characterization at free-electron lasers. *Nature Photonics*, 6(12):852–857, 2012. Cited on p.

[140] Chapman, H. N., Fromme, P., Barty, A., White, T. A., Kirian, R. A., Aquila, A., Hunter, M. S., Schulz, J., DePonte, D. P., Weierstall, U., Doak, R. B., Maia, F. R. N. C., Martin, A. V., Schlichting, I., Lomb, L., Coppola, N., Shoeman, R. L., Epp, S. W., Hartmann, R., Rolles, D., Rudenko, A., Foucar, L., Kimmel, N., Weidenspointner, G., Holl, P., Liang, M., Barthelmess, M., Caleman, C., Boutet, S., Bogan, M. J., Krzywinski, J., Bostedt, C., Bajt, S., Gumprecht, L., Rudek, B., Erk, B., Schmidt, C., Hömke, A., Reich, C., Pietschner, D., Strüder, L., Hauser, G., Gorke, H., Ullrich, J., Herrmann, S., Schaller, G., Schopper, F., Soltau, H., Kühnel, K.-U., Messerschmidt, M., Bozek, J. D., Hau-Riege, S. P., Frank, M., Hampton, C. Y., Sierra, R. G., Starodub, D., Williams, G. J., Hajdu, J., Timneanu, N., Seibert, M. M., Andreasson, J., Rocker, A., Jönsson, O., Svenda, M., Stern,

S., Nass, K., Andritschke, R., Schröter, C.-D., Krasniqi, F., Bott, M., Schmidt, K. E., Wang, X., Grotjohann, I., Holton, J. M., Barends, T. R. M., Neutze, R., Marchesini, S., Fromme, R., Schorb, S., Rupp, D., Adolph, M., Gorkhover, T., Andersson, I., Hirsemann, H., Potdevin, G., Graafsma, H., Nilsson, B., and Spence, J. C. H. Femtosecond X-ray protein nanocrystallography. *Nature*, 470(7332):73–77, 2011. Cited on p.

[141] Popmintchev, T., Chen, M.-C., Popmintchev, D., Arpin, P., Brown, S., Alisauskas, S., Andriukaitis, G., Balciunas, T., Mücke, O. D., Pugzlys, A., Baltuska, A., Shim, B., Schrauth, S. E., Gaeta, A., Hernández-García, C., Plaja, L., Becker, A., Jaron-Becker, A., Murnane, M. M., and Kapteyn, H. C. Bright coherent ultrahigh harmonics in the keV x-ray regime from mid-infrared femtosecond lasers. *Science*, 336(6086):1287–1291, 2012. Cited on p.

[142] Silva, F., Teichmann, S. M., Cousin, S. L., Hemmer, M., and Biegert, J. Spatiotemporal isolation of attosecond soft X-ray pulses in the water window. *Nature Communications*, 6:6611, 2015. Cited on p.

[143] Chatelain, R. P., Morrison, V. R., Godbout, C., and Siwick, B. J. Ultrafast electron diffraction with radio-frequency compressed electron pulses. *Applied Physics Letters*, 101(8):081901, 2012. Cited on p.

[144] van Oudheusden, T., Pasmans, P. L. E. M., Geer, S. B. van der, Loos, M. J. d., Wiel, M. J. van der, and Luiten, O. J. Compression of Subrelativistic Space-Charge-Dominated Electron Bunches for Single-Shot Femtosecond Electron Diffraction. *Physical Review Letters*, 105(26):264801, 2010. Cited on p.

[145] Kozak, M., McNeur, J., Leedle, K. J., Deng, H., Schonenberger, N., Ruehl, A., Hartl, I., Harris, J. S., Byer, R. L., and Hommelhoff, P. Optical gating and streaking of free electrons with sub-optical cycle precision. *Nature Communications*, 8: 14342, 2017. Cited on p.

[146] Flannigan, D. J. and Zewail, A. H. 4D electron microscopy: principles and applications. *Accounts of Chemical Research*, 45(10):1828–1839, 2012. Cited on p.

[147] Weathersby, S. P., Brown, G., Centurion, M., Chase, T. F., Coffee, R., Corbett, J., Eichner, J. P., Frisch, J. C., Fry, A. R., Gühr, M., Hartmann, N., Hast, C., Hettel, R., Jobe, R. K., Jongewaard, E. N., Lewandowski, J. R., Li, R. K., Lindenberg, A. M., Makasyuk, I., May, J. E., McCormick, D., Nguyen, M. N., Reid, A. H., Shen, X., Sokolowski-Tinten, K., Vecchione, T., Vetter, S. L., Wu, J., Yang, J., Dürr, H. A., and Wang, X. J. Mega-electron-volt ultrafast electron diffraction at SLAC National Accelerator Laboratory. *Review of Scientific Instruments*, 86(7): 073702, 2015. Cited on p.

[148] Baum, P. and Zewail, A. H. Attosecond electron pulses for 4D diffraction and microscopy. *Proceedings of the National Academy of Sciences of the United States of America*, 104(47):18409–18414, 2007. Cited on p.

[149] Hilbert, S. A., Uiterwaal, C. J., Barwick, B., Batelaan, H., and Zewail, A. H. Temporal lenses for attosecond and femtosecond electron pulses. *Proceedings of the National Academy of Sciences of the United States of America*, 106(26):10558–10563, 2009. Cited on p.

[150] Hassan, M. T., Baskin, J. S., Liao, B., and Zewail, A. H. High-temporal-resolution electron microscopy for imaging ultrafast electron dynamics. *Nature Photonics*, 11 (7):425–430, 2017. Cited on p.

[151] García de Abajo, F. J. Optical excitations in electron microscopy. *Reviews of Modern Physics*, 82(1):209–275, 2010. Cited on p.

[152] Wollenhaupt, M., Bayer, T., and Baumert, T. Control of Ultrafast Electron Dynamics with Shaped Femtosecond Laser Pulses: From Atoms to Solids. In Kitzler, M. and Gräfe, S., editors, *Ultrafast Dynamics Driven by Intense Light Pulses*, volume 86 of *Springer series on atomic, optical, and plasma physics*, pages 63–122. Springer International Publishing, 2016. ISBN 978-3-319-20173-3. Cited on p.

[153] Trebino, R. *Frequency-Resolved Optical Gating: The Measurement of Ultrashort Laser Pulses*. Springer US, 2000. ISBN 146151181X. Cited on p.

[154] Paul, P. M., Toma, E. S., Breger, P., Mullot, G., Augé, F., Balcou, P., Muller, H. G., and Agostini, P. Observation of a Train of Attosecond Pulses from High Harmonic Generation. *Science*, 292(5522):1689–1692, 2001. Cited on p.

[155] Hemsing, E., Dunning, M., Garcia, B., Hast, C., Raubenheimer, T., Stupakov, G., and Xiang, D. Echo-enabled harmonics up to the 75th order from precisely tailored electron beams. *Nature Photonics*, 10(8):512–515, 2016. Cited on p.

[156] Sears, C. M. S., Colby, E., Ischebeck, R., McGuinness, C., Nelson, J., Noble, R., Siemann, R. H., Spencer, J., Walz, D., Plettner, T., and Byer, R. L. Production and characterization of attosecond electron bunch trains. *Physical Review Special Topics - Accelerators and Beams*, 11(6):061301, 2008. Cited on p.

[157] Diosi, L. *A Short Course in Quantum Information Theory: An Approach From Theoretical Physics*. Springer Berlin Heidelberg, 2011. ISBN 9783642161179. Cited on p.

[158] Engl, H. W., Hanke, M., and Neubauer, A. *Regularization of inverse problems*. Kluwer Academic, Dordrecht, 2000. ISBN 9780792341574. Cited on p.

[159] Kaipio, J. P. and Somersalo, E. *Statistical and Computational Inverse Problems*, volume 160 of *Applied Mathematical Sciences*. Springer Science & Business Media, New York, NY, 2005. ISBN 0387271325. Cited on p.

[160] Vandenberghe, L. and Boyd, S. Semidefinite Programming. *SIAM Review*, 38(1): 49–95, 1996. Cited on p.

[161] Rockafellar, R. T. Monotone Operators and the Proximal Point Algorithm. *SIAM Journal on Control and Optimization*, 14(5):877–898, 1976. Cited on p.

[162] Toh, K. C., Tütüncü, R. H., and Todd, M. J. Inexact primal-dual path-following algorithms for a special class of convex quadratic SDP and related problems. *Pacific Journal of Optimization*, 3(1):135–164, 2007. Cited on p.

[163] Toh, K. C., Todd, M. J., and Tütüncü, R. H. SDPT3 — A Matlab software package for semidefinite programming, Version 1.3. *Optimization Methods and Software*, 11(1-4):545–581, 1999. Cited on p.

[164] Bourassin-Bouchet, C. and Couprie, M.-E. Partially coherent ultrafast spectrography. *Nature Communications*, 6:6465, 2015. Cited on p.

[165] Karski, M., Förster, L., Choi, J.-M., Steffen, A., Alt, W., Meschede, D., and Widera, A. Quantum walk in position space with single optically trapped atoms. *Science*, 325(5937):174–177, 2009. Cited on p.

[166] Dainty, J. C. and Fienup, J. R. Phase Retrieval and Image Reconstruction for Astronomy. In Stark, H., editor, *Image Recovery*, pages 231–275. Elsevier Science, Oxford, 1987. ISBN 0323145973. Cited on p.

[167] Millane, R. P. Phase retrieval in crystallography and optics. *Journal of the Optical Society of America A*, 7(3):394, 1990. Cited on p.

[168] Misell, D. L. A method for the solution of the phase problem in electron microscopy. *Journal of Physics D: Applied Physics*, 6(1):L6–L9, 1973. Cited on p.

[169] Gerchberg, R. W. and Saxton, W. O. A Practical Algorithm for the Determination of Phase from Image and Diffraction Plane Pictures. *Optik*, 35(2):237–246, 1972. Cited on p.

[170] Miao, J., Charalambous, P., Kirz, J., and Sayre, D. Extending the methodology of X-ray crystallography to allow imaging of micrometre-sized non-crystalline specimens. *Nature*, 400(6742):342–344, 1999. Cited on p.

[171] Iaconis, C. and Walmsley, I. A. Spectral phase interferometry for direct electric-field reconstruction of ultrashort optical pulses. *Optics Letters*, 23(10):792, 1998. Cited on p.

[172] Kane, D. J. Principal components generalized projections: a review. *J. Opt. Soc. Am. B*, 25(6):A120, 2008. Cited on p.

[173] Anton, H. and Rorres, C. *Elementary Linear Algebra: With Supplemental Applications*. Wiley, 10th edition, 2011. ISBN 0470561572. Cited on p.

[174] Hoppe, W. Beugung im inhomogenen Primärstrahlwellenfeld. I. Prinzip einer Phasenmessung von Elektronenbeugungsinterferenzen. *Acta Crystallographica Section A*, 25(4):495–501, 1969. Cited on p.

[175] Faulkner, H. M. L. and Rodenburg, J. M. Movable aperture lensless transmission microscopy: a novel phase retrieval algorithm. *Physical Review Letters*, 93(2): 023903, 2004. Cited on p.

[176] Lucchini, M., Brugmann, M. H., Ludwig, A., Gallmann, L., Keller, U., and Feurer, T. Ptychographic reconstruction of attosecond pulses. *Optics Express*, 23(23): 29502–29513, 2015. Cited on p.

[177] Thibault, P. and Menzel, A. Reconstructing state mixtures from diffraction measurements. *Nature*, 494(7435):68–71, 2013. Cited on p.

[178] Monmayrant, A., Weber, S., and Chatel, B. A newcomer's guide to ultrashort pulse shaping and characterization. *Journal of Physics B: Atomic, Molecular and Optical Physics*, 43(10):103001, 2010. Cited on p.

[179] Guzzinati, G., Clark, L., Béché, A., Juchtmans, R., van Boxem, R., Mazilu, M., and Verbeeck, J. Prospects for versatile phase manipulation in the TEM: beyond aberration correction. *Ultramicroscopy*, 151:85–93, 2015. Cited on p.

[180] Müller, H., Jin, J., Danev, R., Spence, J., Padmore, H., and Glaeser, R. M. Design of an electron microscope phase plate using a focused continuous-wave laser. *New Journal of Physics*, 12(7):073011, 2010. Cited on p.

[181] Schwartz, O., Axelrod, J. J., Tuthill, D. R., Haslinger, P., Ophus, C., Glaeser, R. M., and Müller, H. Near-concentric Fabry-Pérot cavity for continuous-wave laser control of electron waves. *Optics Express*, 25(13):14453, 2017. Cited on p.

[182] Röder, F. and Lubk, A. Transfer and reconstruction of the density matrix in off-axis electron holography. *Ultramicroscopy*, 146:103–116, 2014. Cited on p.

[183] Lubk, A. and Röder, F. Phase-space foundations of electron holography. *Physical Review A*, 92(3):416, 2015. Cited on p.

[184] Möllenstedt, G. and Düker, H. Fresnelscher Interferenzversuch mit einem Biprisma für Elektronenwellen. *Naturwissenschaften*, 42(2):41, 1955. Cited on p.

[185] Luttikhof, M. J. H., Khachatryan, A. G., van Goor, F. A., and Boller, K.-J. Generating Ultrarelativistic Attosecond Electron Bunches with Laser Wakefield Accelerators. *Physical Review Letters*, 105(12):124801, 2010. Cited on p.

[186] Naumova, N., Sokolov, I., Nees, J., Maksimchuk, A., Yanovsky, V., and Mourou, G. Attosecond Electron Bunches. *Physical Review Letters*, 93(19):195003, 2004. Cited on p.

[187] Stupakov, G. V. and Zolotorev, M. S. Ponderomotive Laser Acceleration and Focusing in Vacuum for Generation of Attosecond Electron Bunches. *Physical Review Letters*, 86(23):5274, 2001. Cited on p.

[188] Kozák, M., Eckstein, T., Schönenberger, N., and Hommelhoff, P. Inelastic ponderomotive scattering of electrons at a high-intensity optical travelling wave in vacuum. *Nature Physics*, 2017. Cited on p.

[189] Yalunin, S. V., Priebe, K. E., and Ropers, C. manuscript in preparation. 2017. Cited on p.

[190] Wang, H., Shi, L., Lukyanchuk, B., Sheppard, C., and Chong, C. T. Creation of a needle of longitudinally polarized light in vacuum using binary optics. *Nature Photonics*, 2(8):501–505, 2008. Cited on p.

[191] Baum, P. and Zewail, A. H. 4D attosecond imaging with free electrons: Diffraction methods and potential applications. *Chemical Physics*, 366(1-3):2–8, 2009. Cited on p.

[192] Baum, P., Manz, J., and Schild, A. Quantum model simulations of attosecond electron diffraction. *Science China Physics, Mechanics and Astronomy*, 53(6): 987–1004, 2010. Cited on p.

[193] Shao, H.-C. and Starace, A. F. Detecting Electron Motion in Atoms and Molecules. *Physical Review Letters*, 105(26):263201, 2010. Cited on p.

[194] Shao, H.-C. and Starace, A. F. Imaging coherent electronic motion in atoms by ultrafast electron diffraction. *Physical Review A*, 88(6):062711, 2013. Cited on p.

[195] Yakovlev, V. S., Stockman, M. I., Krausz, F., and Baum, P. Atomic-scale diffractive imaging of sub-cycle electron dynamics in condensed matter. *Scientific Reports*, 5:14581, 2015. Cited on p.

[196] Shao, H.-C. and Starace, A. F. Imaging electronic motions in atoms by energy-resolved ultrafast electron diffraction. *Physical Review A*, 90(3):032710, 2014. Cited on p.

[197] Plemmons, D. A. and Flannigan, D. J. Discrete Chromatic Aberrations Arising from Photoinduced Electron-Photon Interactions in Ultrafast Electron Microscopy. *The Journal of Physical Chemistry A*, 120(20):3539–3546, 2016. Cited on p.

[198] Rose, H. H. Optics of high-performance electron microscopes. *Science and Technology of Advanced Materials*, 9(1):014107, 2008. Cited on p.

[199] Kabius, B., Hartel, P., Haider, M., Müller, H., Uhlemann, S., Loebau, U., Zach, J., and Rose, H. First application of Cc-corrected imaging for high-resolution and energy-filtered TEM. *Journal of Electron Microscopy*, 58(3):147–155, 2009. Cited on p.

[200] Vincenti, H. and Quéré, F. Attosecond Lighthouses: How To Use Spatiotemporally Coupled Light Fields To Generate Isolated Attosecond Pulses. *Physical Review Letters*, 108(11):113904, 2012. Cited on p.

[201] Hassan, M. T., Liu, H., Baskin, J. S., and Zewail, A. H. Photon gating in four-dimensional ultrafast electron microscopy. *Proceedings of the National Academy of Sciences of the United States of America*, 2015. Cited on p.

[202] Sola, I. J., Mével, E., Elouga, L., Constant, E., Strelkov, V., Poletto, L., Villoresi, P., Benedetti, E., Caumes, J.-P., Stagira, S., Vozzi, C., Sansone, G., and Nisoli, M. Controlling attosecond electron dynamics by phase-stabilized polarization gating. *Nature Physics*, 2(5):319–322, 2006. Cited on p.

[203] Pellegrini, C., Marinelli, A., and Reiche, S. The physics of x-ray free-electron lasers. *Reviews of Modern Physics*, 88(1):015006, 2016. Cited on p.

[204] Yu, L.-H., Babzien, M., Ben-Zvi, I., DiMauro, L. F., Doyuran, A., Graves, W., Johnson, E., Krinsky, S., Malone, R., Pogorelsky, I., Skaritka, J., Rakowsky, G., Solomon, L., Wang, X. J., Woodle, M., Yakimenko, V., Biedron, S. G., Galayda, J. N., Gluskin, E., Jagger, J., Sajaev, V., and Vasserman, I. High-Gain Harmonic-Generation Free-Electron Laser. *Science*, 289(5481):932–934, 2000. Cited on p.

[205] Stupakov, G. Using the beam-echo effect for generation of short-wavelength radiation. *Physical Review Letters*, 102(7):074801, 2009. Cited on p.

[206] Schoenlein, R. W., Chattopadhyay, S., Chong, H. H. W., Glover, T. E., Heimann, P. A., Shank, C. V., Zholents, A. A., and Zolotorev, M. S. Generation of Femtosecond Pulses of Synchrotron Radiation. *Science*, 287(5461):2237–2240, 2000. Cited on p.

[207] Baum, P. On the physics of ultrashort single-electron pulses for time-resolved microscopy and diffraction. *Chemical Physics*, 423:55–61, 2013. Cited on p.

[208] Querlioz, D., Saint-Martin, J., Bournel, A., and Dollfus, P. Wigner Monte Carlo simulation of phonon-induced electron decoherence in semiconductor nanodevices. *Physical Review B*, 78(16):165306, 2008. Cited on p.

[209] Dorfman, K. E., Schlawin, F., and Mukamel, S. Nonlinear optical signals and spectroscopy with quantum light. *Reviews of Modern Physics*, 88(4):1018, 2016. Cited on p.

[210] Kiesel, H., Renz, A., and Hasselbach, F. Observation of Hanbury Brown–Twiss anticorrelations for free electrons. *Nature*, 418(6896):392–394, 2002. Cited on p.

[211] Dowling, J. P. and Milburn, G. J. Quantum technology: The second quantum revolution. *Philosophical Transactions. Series A, Mathematical, Physical, and Engineering Sciences*, 361(1809):1655–1674, 2003. Cited on p.

[212] Ladd, T. D., Jelezko, F., Laflamme, R., Nakamura, Y., Monroe, C., and O'Brien, J. L. Quantum computers. *Nature*, 464(7285):45–53, 2010. Cited on p.

[213] Perets, H. B., Lahini, Y., Pozzi, F., Sorel, M., Morandotti, R., and Silberberg, Y. Realization of Quantum Walks with Negligible Decoherence in Waveguide Lattices. *Physical Review Letters*, 100(17):170506, 2008. Cited on p.

[214] Kempe, J. Quantum random walks: An introductory overview. *Contemporary Physics*, 44(4):307–327, 2003. Cited on p.

[215] Shenvi, N., Kempe, J., and Whaley, K. B. Quantum random-walk search algorithm. *Physical Review A*, 67(5):1687, 2003. Cited on p.

[216] Kendon, V. Decoherence in quantum walks – a review. *Mathematical Structures in Computer Science*, 17(06):11, 2007. Cited on p.

[217] Peruzzo, A., Lobino, M., Matthews, Jonathan C F, Matsuda, N., Politi, A., Poulios, K., Zhou, X.-Q., Lahini, Y., Ismail, N., Wörhoff, K., Bromberg, Y., Silberberg, Y., Thompson, M. G., and OBrien, J. L. Quantum walks of correlated photons. *Science*, 329(5998):1500–1503, 2010. Cited on p.

[218] Block, A., Etrich, C., Limboeck, T., Bleckmann, F., Soergel, E., Rockstuhl, C., and Linden, S. Bloch oscillations in plasmonic waveguide arrays. *Nature Communications*, 5:3843, 2014. Cited on p.

[219] Meany, T., Gräfe, M., Heilmann, R., Perez-Leija, A., Gross, S., Steel, M. J., Withford, M. J., and Szameit, A. Laser written circuits for quantum photonics. *Laser & Photonics Reviews*, 9(4):363–384, 2015. Cited on p.

[220] Omar, Y., Paunković, N., Sheridan, L., and Bose, S. Quantum walk on a line with two entangled particles. *Physical Review A*, 74(4), 2006. Cited on p.

[221] Friis, N. Reasonable fermionic quantum information theories require relativity. *New Journal of Physics*, 18(3):033014, 2016. Cited on p.

[222] DiVincenzo, D. P. The Physical Implementation of Quantum Computation. *Fortschritte der Physik*, 48(9-11):771–783, 2000. Cited on p.

[223] Luo, M. and Wang, X. Universal quantum computation with qudits. *Science China Physics, Mechanics & Astronomy*, 57(9):1712–1717, 2014. Cited on p.

[224] Abramowitz, M. and Stegun, I. A. *Handbook of mathematical functions: With formulas, graphs, and mathematical tables*. Dover books on mathematics. Dover Publications, 9th edition, 1965. ISBN 978-0486612720. Cited on p.

[225] Orfanidis, S. J. *Electromagnetic Waves*. Online book, http://www.ece.rutgers.edu/~orfanidi/ewa/ewa-1up.pdf, 2016. Cited on p.

[226] Goulielmakis, E., Uiberacker, M., Kienberger, R., Baltuska, A., Yakovlev, V., Scrinzi, A., Westerwalbesloh, T., Kleineberg, U., Heinzmann, U., Drescher, M., and Krausz, F. Direct measurement of light waves. *Science*, 305(5688):1267–1269, 2004. Cited on p.

Author Contributions, Publications and Conference Talks

This Chapter describes the specific contributions of the author in the publications that constitute Chpts. 2 and 3. The cumulative thesis comprises the following articles, that fulfill the requirements of a cumulative thesis according to the doctoral degree regulations of the PhD program ProPhys at the Georg-August University School of Science (GAUSS) Göttingen:

(1) Katharina E. Echternkamp, Armin Feist, Sascha Schäfer, and Claus Ropers, *Ramsey-type phase control of free-electron beams*, Nat. Phys. **12**, 1000-1004 (2016).

(2) Katharina E. Priebe, Christopher Rathje, Sergey V. Yalunin, Thorsten Hohage, Armin Feist, Sascha Schäfer, and Claus Ropers, *Attosecond Electron Pulse Trains and Quantum State Reconstruction in Ultrafast Transmission Electron Microscopy*, Nat. Photon. **11**, 793-797 (2017).

These publications present original work by the author (K.E.P.) concerning the design, setup and conduction of all experiments in (1) and (2), the preparation of the nanostructure used in (1) as well as the analysis of the collected data in (1) and (2). An exception are the measurements showing temporal reshaping in (2), which were performed by Christopher Rathje as part of his Master thesis in collaboration with the author. The SQUIRRELS reconstruction algorithm in (2) was devised by Cl.R. and S.V.Y. and the regularisation scheme was implemented by T.H., both with contributions from K.E.P., who also tested the algorithm and analysed its performance. All results were discussed and interpreted by all authors of the respective publications. The manuscripts of both publications were written by K.E.P. and Cl.R., in (2) with contributions from S.V.Y. and T.H.

Publications

The following articles originated over the course of this work, and are not a direct part of the cumulative thesis.

- Feist, A., Bach, N., Rubiano da Silva, N., Danz, T., Möller, M., Priebe, K. E., Domröse, T., Gatzmann, J. G., Rost, S., Schauss, J., Strauch, S., Bormann, R., Sivis, M., Schäfer, S., and Ropers, C., "Ultrafast transmission electron microscopy using a laser-driven field emitter: femtosecond resolution with a high coherence electron beam", Ultramicroscopy, **176**, 63-73 (2017).

- Wimmer, L., Sivis, M., Herink, G., Yalunin, S. V., Echternkamp, K. E., and Ropers, C., "Highly Nonlinear and Ultrafast Optical Phenomena in Metallic Nanostructures", in Kitzler, M., and Gräfe, S. (Eds.), Ultrafast Dynamics Driven by Intense Light Pulses, Springer International Publishing, Switzerland, (2016).

- Echternkamp, K. E., Herink, G., Yalunin, S. V., Rademann, K., Schäfer, S., and Ropers, C., "Strong-field photoemission in nanotip near-fields: from quiver to subcycle electron dynamics", Appl. Phys. B., **122** (4), 10-10 (2016).

- Kusa, F., Echternkamp, K. E., Herink, G., Ropers, C., and Ashihara, S., "Optical field emission from resonant gold nanorods driven by femtosecond mid-infrared pulses", AIP Advances, **7**, 077138 (2015).

- Feist, A., Echternkamp, K. E., Schauss, J., Yalunin, S. V., Schäfer, S., and Ropers, C., "Quantum coherent optical phase modulation in an ultrafast transmission electron microscope", Nature, **521**, 200-203 (2015).

Conference Talks

- *Free-Electron Quantum State Tomography for the Characterization of Attosecond Electron Pulse Trains*, ONS'17, 2017, Capri, Italien, **Invited**

- *Quantum State Reconstruction and Coherent Control of Free-Electron Quantum States*, GRC Quantum Control of Light and Matter, 2017, South Hadley, Massachusetts, USA, **Invited**

- *Controlling the Quantum State of Free Electrons by Inelastic Optical Near-Field Scattering*, CLEO/Europe-EQEC 2017, München
- *Free-Electron Quantum Optics*, DPG Frühjahrstagung 2017, Dresden
- *Free-Electron Quantum Optics*, Annual QUTIF Meeting (Quantum Dynamics in Tailored Intense Fields) 2017, Dresden
- *Coherent Control of Free-Electron Momentum Superposition States*, PQE (Physics of Quantum Electronics) 2017, Snowbird, Utah, USA, **Invited**
- *Quantum Coherent Manipulation of Free-Electron Wavefunctions*, NFO-14 (Near-field Optics) 2016, Hamamatsu, Japan
- *Quantum Coherent Manipulation of Free-Electron Wavefunctions*, Annual QUTIF Meeting (Quantum Dynamics in Tailored Intense Fields) 2016, Jena
- *Quantum Coherent Ramsey-type Interaction of Free Electrons with Spatially Separated Near-fields*, DPG Frühjahrstagung 2016, Hannover
- *Coherent Electron-Light Interaction in an Ultrafast Electron Microscope*, UNO-4 (Ultrafast Nano-Optics) 2015, Bad Dürkheim
- *Quantum Coherent Interaction of Electrons with Optical Near-fields in an Ultrafast Electron Microscope*, CLEO/Europe-EQEC (Conference on Lasers and Electro-Optics) 2015, München
- *Quantum Coherent Interaction of Electrons with Optical Near-fields in an Ultrafast Electron Microscope*, Photonics North 2015, Ottawa, Kanada
- *Electron Tunneling and Acceleration at Gold Nanostructures Driven by Ultrashort Mid-Infrared Pulses*, CLEO:2014 (Conference on Lasers and Electro-Optics) 2014, San José, USA

Danksagung

An dieser Stelle möchte ich mich bei all denjenigen bedanken, die mich während meiner Promotion unterstützt und zum Gelingen dieser Arbeit beigetragen haben.

Zu allererst gilt mein Dank Prof. Dr. Claus Ropers, meinem Doktorvater, der mir diese Arbeit überhaupt erst ermöglicht hat. Ich danke ihm ganz herzlich für die gute Betreuung, für die Möglichkeit, an einer Vielzahl Konferenzen teilzunehmen, für das entgegengebrachte Vertrauen und für viele inspirierende Diskussionen!

Prof. Dr. Dirk Schwarzer danke ich für die freundliche Übernahme der Zweitbetreuung und sein Interesse an meiner Arbeit.

Ich danke Prof. Dr. Stefan Mathias und Prof. Dr. Thomas Baumert für die freundliche Übernahme des Korreferats.

Ganz besonders bedanken möchte ich mich bei Armin Feist für die Einarbeitung am UTEM und seine Unterstützung im Labor, für seine unerschöpfliche Hilfsbereitschaft, die harmonische Zusammenarbeit und insbesondere für seine Freundschaft! Ich danke ihm außerdem für die guten Ratschläge in fachlichen und persönlichen Fragen.

I'd like to thank Prof. Dr. Sergey Yalunin for the fruitful collaboration on the SQUIRRELS project and for answering all my questions concerning theory!

Prof. Dr. Thorsten Hohage danke ich für die unkomplizierte Zusammenarbeit und für seinen Einsatz für den Rekonstruktionsalgorithmus. Vielen Dank für die geduldige Beantwortung all meiner Fragen zu Regularisierung!

Ich möchte mich bei allen aktuellen und ehemaligen Mitgliedern der Arbeitsgruppe für das außergewöhnlich gute Arbeitsklima, die große Hilfsbereitschaft und für viele lustige und erlebnisreiche Ausflüge bedanken. Besonders hervorheben möchte ich Dr. Max Gulde und Prof. Dr. Georg Herink für die großartige Betreuung während meiner Bachelor- bzw. Masterarbeit und ihre motivierende Art und Dr. Murat Sivis für die unterhaltsamen FIB-Sessions, für seine Begeisterung und gute Laune. Ein besonderer Dank geht an Lara Wimmer für ihr offenes Ohr bei fachlichen und persönlichen Fragen und die traditionellen Frischluftpausen! Des Weiteren Danke ich Christopher Rathje für die gute Zusammenar-

beit. Für die tollen Bürogemeinschaften möchte ich u.a. Georg und Lara und zuletzt Sergey und Christopher danken.

Für's fleißige Korrekturlesen danke ich Murat, Armin, Lara, und Marcus Horwood.

Meinen Freunden und Studienkollegen – dem "Obstsalat" – Daja, Aike, Ann-Kathrin, Jelena, Jan, Johannes und Kolja, die mich durch das Physikstudium begleitet haben, sowie meinen FSR-Kollegen danke ich für die schöne gemeinsame Zeit in Göttingen.

Ein besonders großer Dank gilt meinen Eltern, die immer für mich da waren und sind und die mich mein ganzes Leben lang unterstützt haben.

Meinem Mann Dr. Marius Priebe danke ich dafür, dass er mich immer wieder ermutigt und mir während meiner Zusammenschreibphase den Rücken freigehalten hat. Ich danke ihm von ganzem Herzen für seine unermüdliche Unterstützung und vor Allem für seine Liebe.